DISSERTATION

RADIATIVE FEEDBACKS IN TROPICAL ORGANIZED CONVECTION AND THE MADDEN-JULIAN OSCILLATION

Submitted by

Wei-Ting Hsiao

Department of Atmospheric Science

In partial fulfillment of the requirements

For the Degree of Doctor of Philosophy

Colorado State University

Fort Collins, Colorado

Fall 2024

Doctoral Committee:

Advisor: Eric D. Maloney

Maria A. A. Rugenstein
Christian D. Kummerow
David A. Randall
Nathaniel D. Mueller

ABSTRACT

RADIATIVE FEEDBACKS IN TROPICAL ORGANIZED CONVECTION AND THE MADDEN-JULIAN OSCILLATION

The organization of tropical deep convection is supported by radiative feedbacks, in which high clouds and moisture anomalies associated with convection imposes anomalous longwave (LW) radiative heating in the atmosphere, further supporting convection. Despite an abundance of studies using numerical simulations, the interactions between tropical convective organization, radiative feedbacks, and the large-scale atmospheric environment have not been comprehensively examined in real-world observations. The present dissertation examines such interactions among tropical mesoscale organized convection, radiative feedbacks, and the Madden-Julian oscillation (MJO) using a set of observation-derived data products, including retrievals using spaceborne satellites and ground-based precipitation radar, along with combined products and reanalyses. The main findings in each chapter are summarized as follows: (1) higher sea surface temperature and stronger low-level wind shear strength enhance tropical mesoscale convective activity, increasing cirrus cloud cover and LW heating generated per unit precipitation. (2) the estimation of LW cloud-radiative feedback (LW CRF), defined as the LW cloud-radiative heating produced per unit precipitation, is sensitive to the precipitation data set used. (3) radiatively driven circulation and the associated moistening effects in the MJO can be derived in a weak-temperature-gradient framework and a linear baroclinic model. The result suggests that LW heating moistens the MJO more efficiently than the total apparent heat source, while shortwave (SW) radiative effects dry the MJO. (4) The LW CRF of the MJO is spatially inhomogeneous, with stronger feedbacks over the tropical Indian ocean and to the northwest of Australia, but weaker feedbacks over the tropical western and central Pacific. The spatial pattern may be determined by the spatial distribution of preferred convective types and precipitation efficiency.

ACKNOWLEDGEMENTS

I first would like to thank my advisor, Eric, on helping me a lot on completing my Ph.D. research. Despite his busy schedule of being a department head, we still have meetings every week to catch up on life and research. With many random research ideas popping up in my head, most of them being not rigorous enough, Eric offered much freedom to try out these ideas and provided very solid feedbacks to help me refine the missing logical connections. I also have learned a lot about scientific writing and doing a big research project, and I really enjoyed the time working with him. Big thanks to my committee, Chris, Maria, Dave, and Nathan, for their feedbacks and discussions during all the meetings. The frequent discussions with our research collaborators, Nick and Chris, were very motivating, and I learned a lot about satellites working with them. I enjoyed the time working with past and current Maloney's group members and officemates: Justin Hudson, Michael, Justin Whitaker, Bohar, Hien, Charlotte, Emily, Kyle, Amanda, Zane, Daniel, Jack, Zaibeth, Jack, Jingxuan, Chris, Yu-Cian, and Yihao (this is a long list…and sorry if I missed your name!). Thanks for those who have attended the ATS West Study Club – the group really motivated me when I was stuck on my progress, and got me chances to learn things outside of my narrow field of expertise. I cannot finish this dissertation without any of them mentioned above.

Thanks for all the staff at the department who were very helpful and supportive, such that I would not be able to smoothly complete my degree here without any of them. I especially want to thank Sarah for helping me navigating through the graduate school. My time serving at ATSISSA was truly valuable, that I got to think about my identity as an international student and how I could contribute to the environment. I felt lucky and happy to be a part of the department.

Deep appreciation to Jingxuan who has generously supported me all along the way. I could not imagine the difficult time when I was very stressed and confused about life and career without her. The greatest change of myself studying abroad is probably not about the academic achievements gained, but the profound change about values and how to live a life that I learned largely from her, especially on how to be healthy and a better person.

Thank all the colleagues and friends I met here. The hiking group helped me a lot maintaining my sanity during the pandemic, and I enjoyed hanging out with them. I cannot end this section without thanking my family, friends, and collogues in Taiwan. Thanks to my family - although having an academic career and studying abroad always sound intimidating to them, they still support me and always hope that I can be happy pursuing what I love. The professors and colleagues at National Taiwan University opened my eyes to the world of scientific research. I especially would like to express sincere appreciation to Yen-Ting who has greatly supported me no just for my career but as a life mentor. My interest in atmospheric science dates back to my high school years at HSNU, where I attended the Earth Science training offered by Teacher Hung and Teacher Wang. Thank them for all those great times which really impacted my life path.

I would like to thank NASA, NOAA and NSF for the research funds to make my attendance of the Ph.D. program in the US possible. Thank Colleen Mikovitz for calculating the radiative heating rates used throughout this dissertation, and the discussions with the NASA NEWS team were fruitful and helped a lot for the completion of this dissertation.

TABLE OF CONTENTS

ABSTRACT ii
ACKNOWLEDGEMENTS iv

CHAPTER 1. Introduction 1

CHAPTER 2. Observed Relationships between Sea Surface Temperature, Vertical Wind Shear, Tropical Organized Deep Convection, and Radiative Effects 5
  2.1 Introduction 5
  2.2 Methodology 7
    2.2.1 Tropical convective rain states (CRS) and CRS rain contributions 7
    2.2.2 Large-scale meteorological variables 11
    2.2.3 El Niño-Southern oscillation (ENSO) indices 12
  2.3 Tropical SST control on convection and radiative feedbacks 13
    2.3.1 Tropical SST and CRS rain contributions 13
    2.3.2 Tropical SST and radiative feedbacks 16
    2.3.3 Possibly stronger control on $f_{DeepOrg}$ by SST than by SST* 18
  2.4 Effects of vertical wind shear on the transition SST of $f_{DeepOrg}$ and radiative feedbacks ... 23
    2.4.1 The transition SST of $f_{DeepOrg}$ versus low-level wind shear 23
    2.4.2 The transition SST of $f_{DeepOrg}$ versus mid-level wind shear 26
    2.4.3 Cloud radiative feedback following $f_{DeepOrg}$ and vertical wind shears 29
  2.5 Discussion 34
  2.6 Summary 36

CHAPTER 3. Tropical Longwave Cloud-radiative Feedback Derived by Different Precipitation Datasets 40
  3.1 Introduction 40
  3.2 Methodology 42
    3.2.1 Data 42
    3.2.2 Signal filtering 44
  3.3 Results 45
    3.3.1 Differences in precipitation and the climatological radiative feedback 45
    3.3.2 Precipitation and radiative feedback in the MJO 47
    3.3.3 Precipitation and radiative feedback in other tropical waves 49

3.4 Summary 53

CHAPTER 4. Three-dimensional Structure of Radiative Effect in the Observed Madden-Julian Oscillation 56

4.1 Introduction 56

4.2 MJO composites using OMI 58

4.2.1 Data 58

4.2.2 Compositing method 60

4.2.3 Basic fields 62

4.3 Diagnosis of moistening induced by radiative effects 64

4.3.1 Vertical-advective moistening 64

4.3.2 Horizontal winds 68

4.4 Radiative moistening in the MJO composite 69

4.4.1 Vertical-advective moistening at the center of the MJO 69

4.4.2 The three-dimensional spatial structure of MJO radiation 74

4.5 Implication for MJO dynamics 81

4.5.1 MJO growth/propagation contributions 81

4.5.2 Radiative contribution to MJO propagation 84

4.5.3 Importance of radiation on the MJO enhancement events 89

4.6 Summary 92

CHAPTER 5. Spatially Inhomogeneous Longwave Cloud-radiative-convective Feedback in Tropical Intraseasonal Variability 95

5.1 Introduction 95

5.2 Methodology 96

5.2.1 Data and filtering method 96

5.2.2 Defining LW CRF 98

5.3 The spatially non-uniform LW CRF 100

5.3.1 Intraseasonal OLR does not entirely match intraseasonal precipitation 100

5.3.2 The spatial structure of LW CRF 102

5.4 The cause of the different values of LW cloud-radiative feedback 104

5.4.1 Overview 104

5.4.2 Vertical structure of convection and clouds 106

5.4.3 Mesoscale organization of convection 108

5.4.4 Different heights of ITCZ and SPCZ 111

5.4.5 Precipitation efficiency 112
5.4.6 Synopsis 113
5.5 Possible effects on the MJO 114
5.6 Summary 115

CHAPTER 6. Summary 118
6.1 Main findings of this dissertation 118
6.2 Future outlook 122

REFERENCES 124
APPENDIX A 139
APPENDIX B 156
B1. Details of the spectral analyses 156
B2. Details of the statistical methods 157

CHAPTER 1

Introduction

Tropical deep convection is commonly organized. For example, mesoscale convective systems and tropical cyclones consist of multiple deep convective cores, and these clustered systems are somewhat self-sustained (see reviews by K. Emanuel, 2018; Houze, 2004). These systems produce intense rainfall and winds, which cause severe impact on property and human livelihood. Convectively-coupled equatorial waves (CCEWs; Kiladis et al., 2009) and the Madden-Julian oscillation (T. Li et al., 2018; MJO; Madden & Julian, 1971, 1972) are also a manifestation of organization of tropical deep convection, where individual thunderstorms interact with large-scale dynamics, and the whole envelope of deep convection propagates and develops. These large-scale convective phenomena remotely impact weather globally through teleconnections produced by, for example, atmospheric Rossby wave propagation (Kai-Chih Tseng et al., 2019). Understanding the organization of convection is thus important in understanding the Earth's weather and climate systems, for prediction, and for its impact on human society.

Convective organization in numerical model simulations, commonly referred to as convective aggregation, has been extensively studied (Wing et al., 2017). However, the drivers of convective organization and its impact on the weather and climate systems have not been as extensively explored and understood using observations. Some attempts have been made to transfer knowledge from modeling results to help explain the drivers of real world organization, but there seems to be a lack of agreements, such as whether the presence of vertical wind shear helps convective organization (e.g., Bretherton et al., 2005; Hsiao et al., 2024). While simulations with limited domains and simple boundary conditions under radiative-convective equilibrium have shown the impact of convective organization on the climate system through modulation of radiative budget, how this can be used to understand the impact of real-world convective organization on climate is also unclear (Mauritsen & Stevens, 2015). Thus, more study is needed to understand the real-world nature of tropical convective organization.

Radiative effects are found to be important in the organization of convection in numerical simulations (Muller & Bony, 2015). When deep convection occurs, it generates high-altitude clouds by detrainment. These clouds consist of ice, which are often optically thin but opaque in the infrared band of electromagnetic waves (or longwave radiation). The presence of these ice clouds effectively trap outgoing longwave radiation emitted by the Earth’s surface and lower troposphere, anomalously heating the atmosphere and the surface (Webster & Stephens, 1980). This mechanism produces a positive longwave cloud-radiative feedback such that when deep convection produces ice clouds, more anomalous atmospheric longwave heating is generated near the convective region, which supports further convection.

How this radiative feedback plays a role in modulating the organization of tropical convection in the real world is not well understood. Tropical cyclone development is much enhanced by the longwave cloud-radiative effect (Ruppert et al., 2020). But what about tropical organized convective systems on other scales, and how are these interactions mediated by large-scale atmospheric conditions? This dissertation aims to investigate how real-world organization of convection interacts with the atmospheric radiative feedback, and how large-scale meteorological conditions modulate this interaction. The dissertation focuses on examining the radiative feedbacks in two types of organized tropical convective systems: mesoscale convective systems and the MJO, in observation-derived data sets.

In **Chapter 2**, the large-scale conditions controlling tropical mesoscale convective activity are examined using monthly mean reanalyses and satellite observations. Higher sea-surface temperatures and higher low-level wind shear magnitudes are found to be associated with higher tropical mesoscale convective activity. Cirrus cloud cover and LW cloud-radiative heating produced per unit surface precipitation are further found to covary with tropical mesoscale convective activity, and both increase with sea-surface temperature and low-level wind shear magnitudes. This work is published in *Journal of Climate* as:

- Hsiao, W.-T., Maloney, E. D., Leitmann-Niimi, N. M., & Kummerow, C. D. (2024). Observed Relationships between Sea Surface Temperature, Vertical Wind Shear, Tropical Organized Deep Convection, and Radiative Effects. *Journal of Climate*, *37*(4), 1277–1293.

Since radiative feedbacks are generally defined as the anomalous atmospheric radiative heating generated with per unit anomalous surface precipitation, the magnitudes of the feedbacks are sensitive to the observational data set used for estimating the radiative heating and precipitation. **Chapter 3** examines such sensitivity for longwave radiative feedbacks in the MJO and other CCEWs, and suggests better accuracy using a newer daily precipitation data set, although caveats are provided. This work is published in *Geophysical Research Letters* as:

- Hsiao, W.-T., & Maloney, E. D. (2024). The Longwave Cloud-Radiative Feedback in Tropical Waves Derived by Different Precipitation Data Sets. *Geophysical Research Letters*, *51*(11), e2024GL109143.

The rest of the dissertation focuses on radiative feedbacks in the MJO. In **Chapter 4**, the three-dimensional (3-D) structure of radiative effect in the MJO is examined. A weak-temperature-gradient framework and a linear baroclinic model are used to infer the circulation driven by the 3-D field of radiative heating, and how the radiatively-driven circulation contributes to the moistening of the MJO is investigated. This work will be submitted to *Journal of Atmospheric Science* as:

- Hsiao, W.-T. & Maloney, E. D. Three-dimensional Structure of Radiative Effects in the Observed Madden-Julian Oscillation.

In **Chapter 5**, the longwave cloud-radiative feedback of the MJO is found to have a rich horizontal spatial structure. Possible causes and implications for MJO dynamics are examined. This work will be submitted to *Journal of Climate* as:

- Hsiao, W.-T. & Maloney, E. D. Spatially Inhomogeneous Longwave Cloud-radiative-convective Feedback in Tropical Intraseasonal Variability.

Finally, a summary of this dissertation and a future outlook are provided in **Chapter 6**.

CHAPTER 2

Observed Relationships between Sea Surface Temperature, Vertical Wind Shear, Tropical Organized Deep Convection, and Radiative Effects[1]

2.1 Introduction

Tropical precipitation is largely produced by convection that can be classified into certain types, each of them imposing distinct moistening and heating effects on the atmospheric vertical profile (e.g., Chen et al., 2021; Elsaesser et al., 2010; Houze et al., 2015; R. H. Johnson et al., 1999). Long-lived, horizontally wide-spread *organized* deep convection largely determines the spatiotemporal distribution of the precipitation means and extremes in the current climate, and will regulate how these change with climate warming (Roca & Fiolleau, 2020; Rossow et al., 2013; Semie & Bony, 2020; Tan et al., 2015). Instead of being a passive factor in how tropical precipitation is statistically realized, organized deep convection drives radiative effects that not only locally help maintain its own development, but also regulate the Earth's energy budget through modification of moisture, cloudiness, and large-scale circulation (Bony et al., 2016, 2020; Houze, 1989; Schumacher et al., 2004). Differences in simulating organized deep convection and related processes in tropical ascending regions have been suggested to contribute to a spread in future climate projections (Bony et al., 2015; S. Lee et al., 2022; Mauritsen & Stevens, 2015; B. Wolding et al., 2020). Thus, it is vital to understand what controls the activity of organized deep convection in the tropics.

---

[1] This chapter contains material that is published in *Journal of Climate* as: Hsiao, W.-T., Maloney, E. D., Leitmann-Niimi, N. M., & Kummerow, C. D. (2024). Observed Relationships between Sea Surface Temperature, Vertical Wind Shear, Tropical Organized Deep Convection, and Radiative Effects. *Journal of Climate*, *37*(4), 1277–1293.

Sea surface temperature (SST) has been previously shown to strongly regulate tropical deep convection and precipitation. Early pioneering studies showed positive correlations between tropical SST and deep convective activity as measured by outgoing longwave radiative flux, with a "pick-up" of convective activity above SSTs of 26-27°C observed (Gadgil et al., 1984; Graham & Barnett, 1987; Lau et al., 1997; Waliser & Graham, 1993; Chidong Zhang, 1993). Studies utilizing cloud-resolving models have shown some SST dependence for the onset of aggregated convection, a numerical phenomenon possibly relevant to real-world organized deep convection, but this dependence is sensitive to the model and simulation setup (Wing, 2019; Wing et al., 2017, 2020). In addition, observations suggest that higher precipitation rate is collocated with higher SST relative to the tropical mean (SST*) (A. H. Sobel et al., 2002), associated with higher convective instability (Vecchi & Soden, 2007) and column saturation fraction (CSF) (Bretherton et al., 2004), both of which imply higher effective buoyancy to support convective systems. While modern observation has started to support global surveys of convective systems (e.g., Houze et al., 2015; Zipser et al., 2006), studies that explicitly examine the observed relationship between tropical SST or SST* and organized deep convection are sparse.

In addition to SST and its correlated thermodynamical factors, organized deep convection can be impacted by nonthermodynamical factors. It has long been recognized by the mesoscale meteorology community that the presence of low-level wind shear assists in the development of mesoscale convective systems (Houze, 2004 and reference therein). For instance, low-level wind shear balances the horizontal vorticity created by convective cold pools, which helps support the growth of new convective cells in a convection system (Rotunno et al., 1988). In numerical experiments, the relationship between convective aggregation and vertical wind shear is complicated, probably due to different simulation setups among studies (Abbot, 2014; Bretherton et al., 2005; Tsai & Wu, 2017; Wing et al., 2017). In observations, low-level vertical wind shear in the pre-initiation stage of convection has been shown to favor organized deep convection in regional survey studies, consistent with mesoscale theory (e.g., Laing & Fritsch, 2000). These different results imply a need for validation from an observational-based, global-coverage investigation of the relationship between vertical wind shear and tropical organized convection, and how thermodynamic factors jointly affect this relationship.

This study aims to improve the understanding of not only how thermodynamics, but also how large-scale dynamical conditions, impact the statistical properties of tropical convective organization and associated radiative effects. The quantitative assessment of the observed connections between organized deep convection, radiative effects, precipitation, SST, and low-level wind shear in the tropics can be used to evaluate biases in numerical simulations, and also provide basic insight into the dynamics of large-scale convective modes of variability in the tropical atmosphere that are mediated by convective organization and radiative feedbacks.

2.2 Methodology

2.2.1 Tropical convective rain states (CRS) and CRS rain contributions

Self-similar tropical *convective rain states* (CRS) of organized deep convection (DeepOrg), isolated deep convection (DeepIso), and shallow convection (Shallow) are identified using spaceborne precipitation radar observations following a similar procedure that Elsaesser et al. (2010) used to define tropical precipitation types. A k-means clustering model is trained and applied on the statistical distribution of rain rates and echo-top heights with echo intensities > 20 dBZ in each oceanic 1° × 1° latitude-by-longitude scene observed by precipitation radars from the Tropical Rainfall Measuring Mission (TRMM; Level 2A TRMMPR V8; Kummerow et al., 1998) exactly as in Elsaesser et al. (2010) from January 1998 to August 2014. A separate k-means clustering model is trained and applied on Global Precipitation Measurement (GPM; GPM KuPR V8; Hou et al., 2014) from March 2014 to December 2021 by first rescaling the clustering parameters so that their means of the 5-month overlapping period match with those in TRMM. Aside from these *convective* scenes, the residual scenes have negligible precipitation and will not be discussed in this study. Since TRMM and GPM precipitation radars cannot track convective systems over time (e.g., Feng et al., 2021), how a convective system evolves is not considered when performing classification. Note that DeepOrg, DeepIso, and Shallow CRS are same as the organized deep convection, unorganized deep convection, and shallow convection clusters in Elsaesser and Kummerow (2013), and DEEP, MID-LEV, and SHAL in Elsaesser et al. (2010), respectively. These prior studies have shown that DeepOrg features mesoscale convective systems and its apparent heating is dominated by stratiform systems with larger cold pool kinetic energy that implies stronger mesoscale downdrafts (Elsaesser et al., 2010; Elsaesser & Kummerow, 2013).

Example snapshots of echo-top heights from each CRS are shown in **Figures 2.1a-c**. In general, DeepOrg scenes have the highest echo-top heights and a larger horizontal extent of higher echo-top heights. DeepIso scenes on average include fewer pixels with the highest echo-top heights and are generally more fragmented horizontally with more isolated cores than DeepOrg. Shallow scenes, on the other hand, have generally low echo-top heights compared to DeepOrg and DeepIso scenes. In addition to echo-top heights, the algorithm also considers the ratio of convective to total rain rates. The classification method captures stronger stratiform rainfall likely from the later stage and the edge of mesoscale convective systems, as shown in some scenes in **Figure 2.1a** with stratiform precipitation areas. Since the algorithm only considers the observed features in the precipitating pixels, some scenes with fragmented convective features are shown in all **Figures 2.1a-c** when the classification parameters are noisy due to insufficient samples. These scenes with small areas of precipitation do not affect the statistical features of CRS and are suggested to not affect their associated rainfall contribution (Elsaesser et al., 2010).

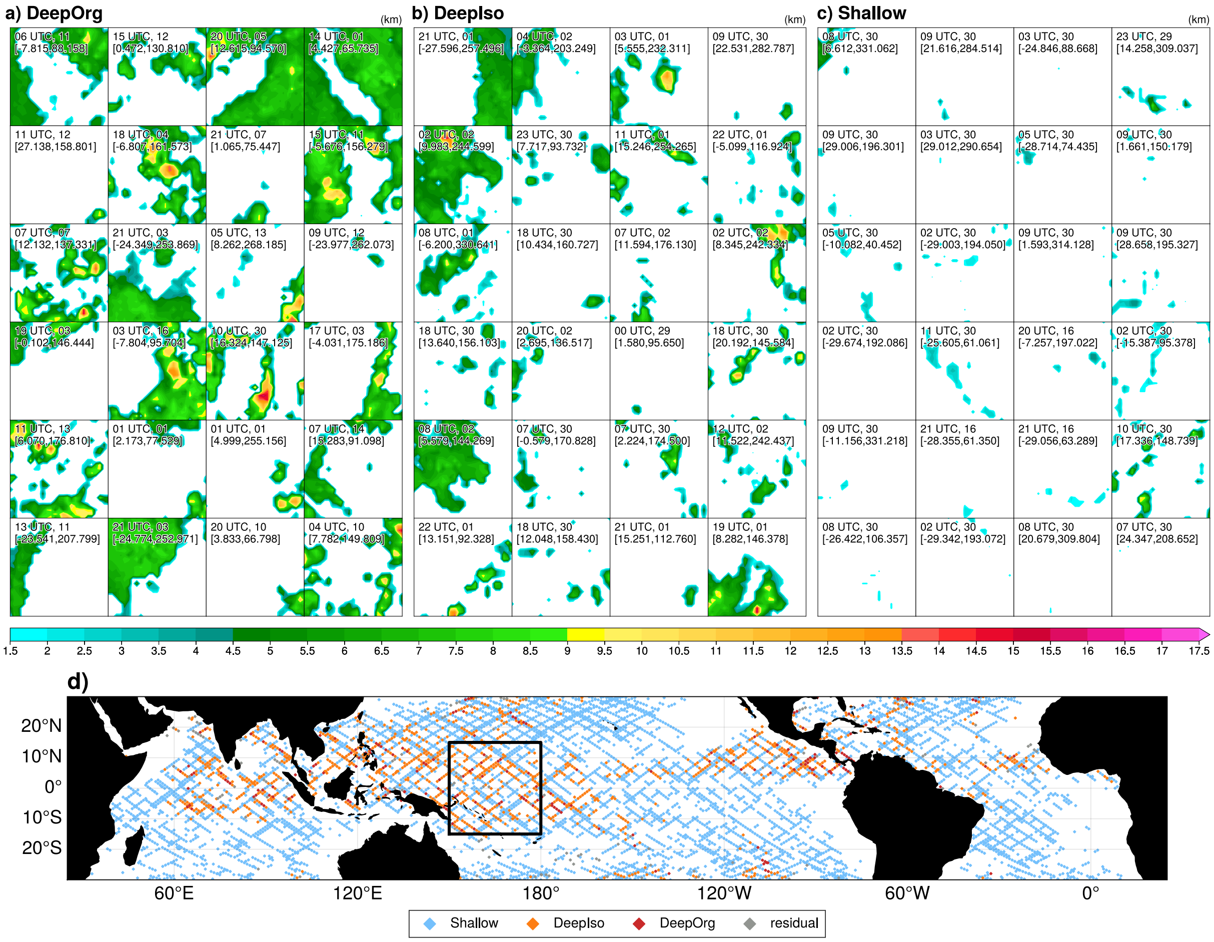

Figure 2.1. Example 1° × 1° CRS scenes of echo top heights (km) measured by TRMM during July 2012 classified as (a) DeepOrg, (b) DeepIso, and (c) Shallow. The time and day of the month (top line) and the center latitude-longitude coordinate (bottom line) of each scene is annotated at the upper left corner. (d) Example of CRS classification over 1 July 2012 to 5 July 2012, with each diamond marker roughly representing the size of a CRS scene, and the black box showing an example of the 30° × 30° domain used for averaging as described in text.

Given a spatiotemporal range, the fractional precipitation contribution of each CRS can be calculated by dividing the precipitation contributed by the scenes of each CRS by the total precipitation contributed by all CRS over that time period and region. The fractional precipitation contributed by each CRS and are referred to as *CRS rain contribution*, and is denoted as f_{DeepOrg}, f_{DeepIso}, f_{Shallow}, respectively for DeepOrg, DeepIso, and Shallow. A time length of a calendar month, and 30° × 30° latitude-by-longitude spatial domains centered at the equator that are progressively shifted by 1° longitude, are used to calculate the CRS rain contributions using all the 1° × 1° scenes included in each domain, as schematically shown in **Figure 2.1d**. Each spatial domain includes more than 5000 CRS scenes per month covered by the swaths of TRMM or GPM precipitation radar. These CRS rain contributions are available during 1998-2021, in which the values from GPM are offset by the difference between TRMM and GPM during their overlapping period such that their means match. TRMM and GPM yield consistent results such that the CRS rain contributions vary similarly over the overlapping period (not shown). Since f_{DeepOrg}, f_{DeepIso}, and f_{Shallow} are fractional precipitation contributions, they can indicate variability in both relative frequency and intensity of convective activity associated with each CRS compared to the others. Note that the large spatial domain (30° × 30°) is chosen to yield statistically stable results. A smaller spatial domain also yields qualitatively consistent conclusions, but provides noisier results (see **Figures A2.1-A2.4** in **Appendix A** for results produced for 10° × 10° domains).

Despite the gradual increase in median and mean f_{DeepOrg} with respect to SST and SST* as shown later in **Chapter 2.3**, the *transition SST* of tropical organized deep convection is defined to quantitatively examine the “pick-up” behavior of f_{DeepOrg}. The transition SST is defined as when the median or the mean of f_{DeepOrg} within a given bin exceeds 0.3 with increasing SST above 26.5°C or increasing SST* above -1°C. The reason for selecting these SST and SST* thresholds is elaborated in **Chapter 2.3**. The criterion of 0.3 is arbitrary, and using various criteria over 0.25-0.35 do not yield different conclusions (**Figure A2.5**). Note that the median of f_{DeepOrg} is used in

SST and SST* spaces in **Chapter 2.3** to be compared to interquartile ranges, and the mean is used to define thresholds in SST-shear and SST*-shear spaces later in **Chapter 2.4**, while using either statistic yields very similar results (not shown).

2.2.2 Large-scale meteorological variables

Monthly-mean large-scale meteorological variables from various data products are compared with the CRS rain contributions in this study. The SST used is from Optimum Interpolation Sea Surface Temperature Version 2 (OISSTv2; Reynolds et al., 2002). SST* is calculated relative to the tropical mean defined as the mean SST between the latitudes of 15°S and 15°N. Surface precipitation is represented by the Global Precipitation Climatology Project version 2.3 product (GPCPv2.3; Adler et al., 2018). Horizontal winds on pressure levels from European Centre for Medium-Range Weather Forecasts Reanalysis v5 (ERA5; Hersbach et al., 2020) are used. The Level-3 products of the Clouds and the Earth's Radiant Energy System synoptic Top of Atmosphere and surface fluxes and clouds (CERES SYN1deg; Doelling et al., 2013, 2016) provide radiative heating rates on pressure levels. CERES CldTypHist provides high ice cloud properties (50-440 mb pressure) binned by their optical depth (τ) including areal coverage, effective temperatures, and effective height for cirrus (Ci; $\tau < 3.6$), cirrostratus (Cs; $23 > \tau > 3.6$), and the upper part of cumulonimbus (Cb; $\tau > 23$).

Data is first averaged horizontally to a 1° × 1° grid. Monthly low-level wind shear magnitudes in ERA5 are calculated as the magnitude of the horizontal wind vector difference between 700 hPa and 925 hPa ($\Delta U_{700\text{-}925}$), with the difference between 500 hPa and 750 hPa used to define mid-level wind shear ($\Delta U_{500\text{-}750}$). Radiative heating rates are calculated using the flux divergence from the CERES SYN1deg product over oceanic regions, and are then linearly regridded vertically to the same pressure levels as ERA5. Cloud radiative heating rates are defined as the total heating rates minus the clear-sky heating rates. Data from OISSTv2, GPCPv2.3, and ERA5 are used during 1998-2021 to match the timespan of the CRS. Data from CERES SYN1deg and CldTypHist is only available during 2003-2021, and is compared to other datasets only during the same range of time.

Monthly-mean oceanic area averages over the 30° × 30° horizontal boxes of the variables described above are then calculated to compare to the CRS rain contributions. Oceanic regions are defined by neglecting grid points of more than 50% land area, as provided by the auxiliary data for CERES SYN1deg. Altering this threshold for land area does not substantially affect the results (not shown). The effective sample size of these averages over all oceanic regions needs to consider the overlap in space between the boxes, the different fractional area represented by each box due to land cover, and different number of days in a calendar month. Based on the above, the effective count is estimated as the actual count divided by 30 (the overlapping counts for each grid cell is 30 with the 1°-longitude shift of spatial boxes), multiplied by the areal fraction of oceanic region within a box (the maximum is 1), and multiplied by the ratio of the days in a calendar month to 31 (the maximum days in a calendar month is 31). This yields effective counts of 2622 over 1998-2021 and 2074 over 2003-2021, respectively. The effective counts are used as weights when calculating all the quartiles, means, and correlations between variables.

2.2.3 El Niño-Southern oscillation (ENSO) indices

In **Chapter 2.3.3**, the dependence of results on ENSO state is discussed. The multivariate ENSO Index Version 2 (MEIv2; T. Zhang et al., 2019) is used to define ENSO events. The bimonthly MEIv2 is linearly interpolated to each month to match the time resolution of the other data. The warm El Niño-like months and the cold La Niña-like months are defined as when the monthly MEIv2 is greater than or equal to 0.5 (n = 35) and smaller than or equal to -0.5 (n = 89), respectively. Note that the magnitude threshold of 0.5 is used instead 1 conventionally to ensure there are sufficient samples in both categories.

2.3 Tropical SST control on convection and radiative feedbacks

2.3.1 Tropical SST and CRS rain contributions

The relationship between CRS rain contributions and SST is explored. **Figure 2.2a** shows the statistical distribution of the fractional precipitation contributions in tropical oceanic regions binned by SST. Overall, f_{DeepIso} is greater than f_{DeepOrg} and f_{Shallow}, indicating that isolated deep convection generally makes up the greatest contribution to total precipitation at all SSTs. However, its contribution is relatively invariant across SST bins. Focusing on the medians (solid lines), f_{DeepIso} is nearly constant over all SST bins at 0.4, with a slight increase with SST over 26-28.5°C to 0.45, and a slight decrease with SST above 28.5°C. The relative contribution to tropical precipitation from organized deep convection and from shallow convection varies more with SST. The median f_{DeepOrg} shows an increase with SST above 27°C from 0.24 to 0.39. Below this 27°C threshold, results are more complex with an increase below 24°C to 0.34, and a decrease with SST over 24.5°C to 27°C from 0.35 to 0.24. The median f_{Shallow} are nearly the mirror image of median f_{DeepOrg}, which is not surprising given that all the fractional precipitation contributions add to unity. **Figure 2.2b** shows the same statistics but for the precipitation contribution by adding both deep convection types ($f_{\mathrm{DeepOrg}}+f_{\mathrm{DeepIso}}$) and for shallow convection (f_{Shallow}). The plot shows that deep convective activity as a whole ($f_{\mathrm{DeepOrg}}+f_{\mathrm{DeepIso}}$) increases with SST above 26.5°C, consistent with previous results as discussed in Introduction.

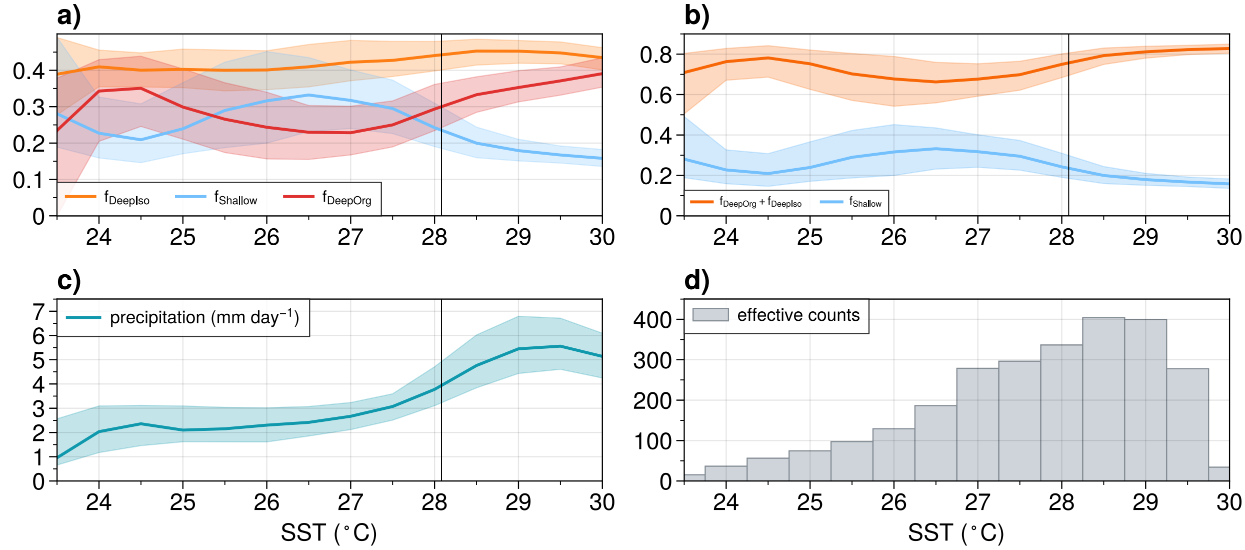

Figure 2.2. The statistical distribution of (a-b) $f_{DeepOrg}$ (red), $f_{DeepIso}$ (orange), $f_{Shallow}$ (blue), and (c) precipitation in mm day^{-1}, binned by SST every 0.5°C, where solid lines denote the medians and shading denotes the range between the first and third quartiles, with color codes of precipitation types annotated. (d) shows the effective count in each SST bin. The transition SST of organized deep convection, defined at where the median $f_{DeepOrg}$ exceeds 0.30 above 26.5°C, is at 28.1°C, showing as the vertical lines in (a-c).

Figure 2.2c shows the statistical distribution of monthly-mean area-averaged tropical oceanic precipitation binned by SST. From 27°C to 29.5°C, the median precipitation sharply increases with SST from 2.7 to 5.6 mm day^{-1}, associated with increase in median $f_{DeepOrg}$ and slight increase in median $f_{DeepIso}$. The median precipitation increases with SST below 24.5°C to 2.4 mm day^{-1}, covarying with increasing median $f_{DeepOrg}$. Between 24.5°C and 27°C, the median precipitation remains nearly constant at 2 mm day^{-1}, despite decreasing median $f_{DeepOrg}$ and increasing median $f_{Shallow}$. The spreads of all the fractional precipitation contributions, if measured by the range between their first and third quartiles (shading), decrease with SST in the range of 27-29.5°C. These statistical features suggest that higher precipitation tends to be produced by increasingly organized deep convection with lower variability in this relationship at higher SSTs. However, as an exception, at the highest SSTs above 29.5°C the median precipitation decreases with SST, but the large interquartile precipitation spread makes the trend uncertain, which may originate from large-scale atmospheric disturbances that controls the onset of precipitation, such as the Madden-Julian oscillation (MJO).

The increase in median $f_{DeepOrg}$ with SST above 27°C is of interest due to its association with active tropical convection and significant precipitation as suggested by the early literature that used outgoing longwave radiative flux as a proxy for convective activity (Gadgil et al., 1984; Graham & Barnett, 1987; Lau et al., 1997; Waliser & Graham, 1993; Chidong Zhang, 1993). Meanwhile, a nearly constant median $f_{DeepIso}$ over all SSTs imply that most of the variation of convective activity with respect to SST observed by previous studies is from the variation in organized deep convective activity, instead of isolated deep convective activity. The definition of the transition SST of tropical organized deep convection where the median or the mean of $f_{DeepOrg}$ exceeds 0.3 is therefore defined only when SST values are above 26.5°C, as mentioned in **Chapter 2.2**. Our calculated transition SST for organized deep convection when conditioned on no other variables is 28.1°C (vertical lines in **Figures 2.2a-c**). The change in transition SST with additional conditioning on vertical wind shear will be examined in **Chapter 2.4**.

A decrease in median $f_{DeepOrg}$ with increasing SST is observed at SST below 27°C (**Figure 2.2a**). A possible explanation for this behavior was suggested in a numerical simulation study, in which stratiform cloud decks favored by low SST and stable atmospheres can produce radiatively driven cold pools that assist in the development of aggregated convection (Coppin & Bony, 2015). However, it is not certain whether this mechanism is present in observations. This phenomenon will not be discussed further in this study, and is left for future research.

2.3.2 Tropical SST and radiative feedbacks

Mesoscale organized deep convection produces larger anvils and more extensive cirrus shields compared to isolated deep convection, which impose a warming effect on the atmosphere by reducing the longwave radiative emission temperature at the top of the atmosphere. This subchapter aims to study the connection between longwave radiative heating and organized deep convective activity in SST space. The radiative heating rates are first integrated over the troposphere (100-1000 mb), and then normalized by total precipitation in units of W m^{-2} to represent the contribution of longwave radiation to atmospheric heating per unit precipitation. This yields the dimensionless tropospheric radiative feedback to precipitation by longwave radiative heating under clear-sky condition ($\hat{Q}_{R,LW,clear}$) and by the cloud radiative effect ($\hat{Q}_{R,LW,cloud}$) defined as all-sky minus clear-sky radiative heating. For consistency, cirrus ice cloud cover is also normalized by total precipitation. The definitions of these radiative feedbacks capture how much heating is associated with a fixed amount of precipitation. Under tropical weak temperature gradient (WTG) theory, this feedback defined by radiative heating per unit surface precipitation is able to support the moistening of the atmosphere and convection through vertical advection, as widely used in studies examining convectively-coupled tropical disturbances (e.g., Adames & Kim, 2016; Kim et al., 2015).

Median normalized cirrus cover generally increases with SST, with a faster increase from 2.6% (mm $day^{-1})^{-1}$ at 27.5°C to 4.4% (mm $day^{-1})^{-1}$ at 30°C compared to lower SST (**Figure 2.3b**). Median $\hat{Q}_{R,LW,cloud}$ also increases with SST, which exceeds zero at around 27.5°C and exceeds 0.1 at 28.5°C (**Figure 2.3a**). These increased feedbacks are consistent with the increase in median $f_{DeepOrg}$ with SST (**Figure 2.2a**), suggesting that more extensive cirrus clouds generated by more organized deep convection led to stronger column longwave radiative heating per unit precipitation of the troposphere. This observed positive radiative feedback of organized deep convection can help maintain upward motion, as suggested by tropical WTG theory that heating must be compensated by adiabatic cooling induced by vertical motion (e.g., A. Sobel & Maloney, 2012). Median $\hat{Q}_{R,LW,clear}$ also rises with SST (**Figure 2.3c**), which is expected given the increase in CSF with SST (**Figure 2.3d**) and its associated clear-sky effect of enhanced water vapor trapping longwave radiative flux in the troposphere.

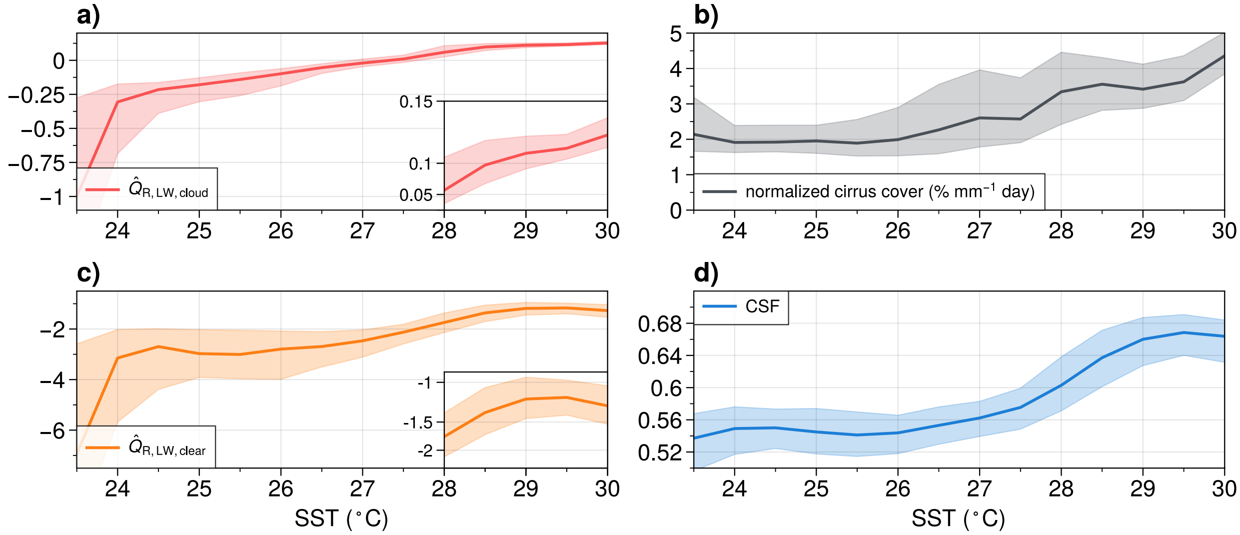

Figure 2.3. The statistical distribution of (a-b) $f_{DeepOrg}$ (red), $f_{DeepIso}$ (orange), $f_{Shallow}$ (blue), and (c) precipitation in mm day^{-1}, binned by SST every 0.5°C, where solid lines denote the medians and shading denotes the range between the first and third quartiles, with color codes of precipitation types annotated. (d) shows the effective count in each SST bin. The transition SST of organized deep convection, defined at where the median $f_{DeepOrg}$ exceeds 0.30 above 26.5°C, is at 28.1°C, showing as the vertical lines in (a-c).

There are also notable heating effects from clouds and the atmosphere absorbing shortwave radiation. Positive shortwave cloud- and clear-sky radiative feedbacks are present with smaller magnitudes than in longwave radiative feedbacks (**Figures S2.6a, c**). Thus, the total radiative feedbacks retain the same patterns as in longwave radiative feedbacks (comparing **Figures S2.3a,**

c with **Figures S2.6a, c**), but are slightly stronger. However, since shortwave cloud radiative heating is commonly top-heavy and associated with a cooling near the surface where the vertical moisture gradient is large (Ruppert & Hohenegger, 2018), it can impose a downward motion under the WTG balance with a drying effect. The complicated interaction between the vertical structure of radiative heating and the moistening feedbacks in tropical deep convection is beyond the scope of this study.

*2.3.3 Possibly stronger control on $f_{DeepOrg}$ by SST than by SST**

To compare to previous studies suggesting SST deviation from its tropical mean (SST*) be a better indicator of tropical precipitation than SST under both global warming trend and interannual variability (e.g., N. C. Johnson & Xie, 2010; A. H. Sobel et al., 2002), similar analysis is performed by binning tropical CRS rain contributions and precipitation by SST* (**Figure 2.4**).In SST* space, the median precipitation increases monotonically above -2.5°C (**Figure 2.4c**), which verifies the conclusion of the previous studies. The CRS rain contributions have qualitatively similar behavior in the SST* space compared to that in the SST space (comparing **Figures 2.4a-b** and **Figures 2.4a-b**): median $f_{DeepIso}$ remains nearly constant; median $f_{DeepOrg}$ increases with SST* above -1°C and behaves oppositely below it; median $f_{Shallow}$ is a mirror image of median $f_{DeepOrg}$. However, the increase in median $f_{DeepOrg}$ with SST* is flatter than for SST at some high temperatures. For example, median $f_{DeepOrg}$ increases with SST* by 0.02 from 0.34 at 1°C to 0.36 at 2°C. In comparison, median $f_{DeepOrg}$ increases with SST by 0.04 from 0.33 at 28.5°C to 0.37 at 29.5°C, having twice as large increase over the same 1°C range, although this 0.02 excess is not very robust comparing to the magnitude of interquartile range (~0.09). The comparison suggests that while SST* is a better predictor of precipitation than SST, SST is more strongly related to organized deep convective activity than SST*. We will show in the next paragraph that this subtle difference may lead to different strengths in radiative feedback that are important for supporting convection.

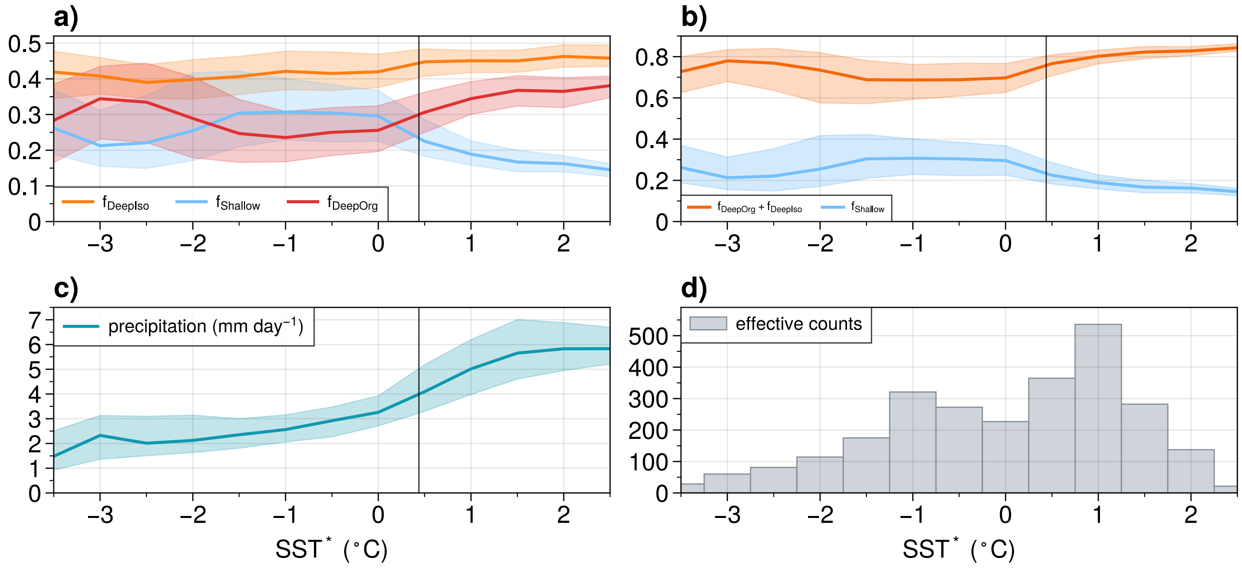

Figure 2.4. As in **Figure 2.2**, but binned by the deviation of SST from its tropical mean (SST*) every 0.5°C. The transition SST* of organized deep convection is at 0.4°C, showing as the vertical lines in (a-c), defined at where the median of $f_{DeepOrg}$ exceeds 0.30 above -1°C.].

Notable differences are shown in SST* space for variables related to longwave radiative feedback compared to those in SST space. Tropical precipitation increases with SST* more monotonically than with SST (**Figure 2.4c**). Consistent with the strong coupling between tropical precipitation and column saturation fraction (CSF) (Bretherton et al., 2004), median CSF and $\hat{Q}_{R,LW,clear}$ also increase with SST* more monotonically (**Figures 2.5c-d**). Median normalized cirrus ice cloud cover generally increases with SST* (**Figure 2.5b**), with a relatively sudden jump from 2.7% (mm day^{-1})$^{-1}$ at 0°C to 3.9% (mm day^{-1})$^{-1}$ at 1°C, and becomes irregular above 1°C compared to that in SST space above 28.5°C. This is reflected in median $\hat{Q}_{R,LW,cloud}$, which increases with SST* below 1°C and remains relatively flatter between 1-2°C compared with that in SST space between 28.5-29.5°C (compare the insets of **Figure 2.3a** and **Figure 2.5a**). This less monotonic behavior of normalized cirrus cover and longwave cloud radiative feedback in SST* space is perhaps because of the weaker increase in organized deep convective activity (measured by median $f_{DeepOrg}$) and associated anvil cloud decks at very high values of SST* versus SST, as discussed in the previous paragraph.

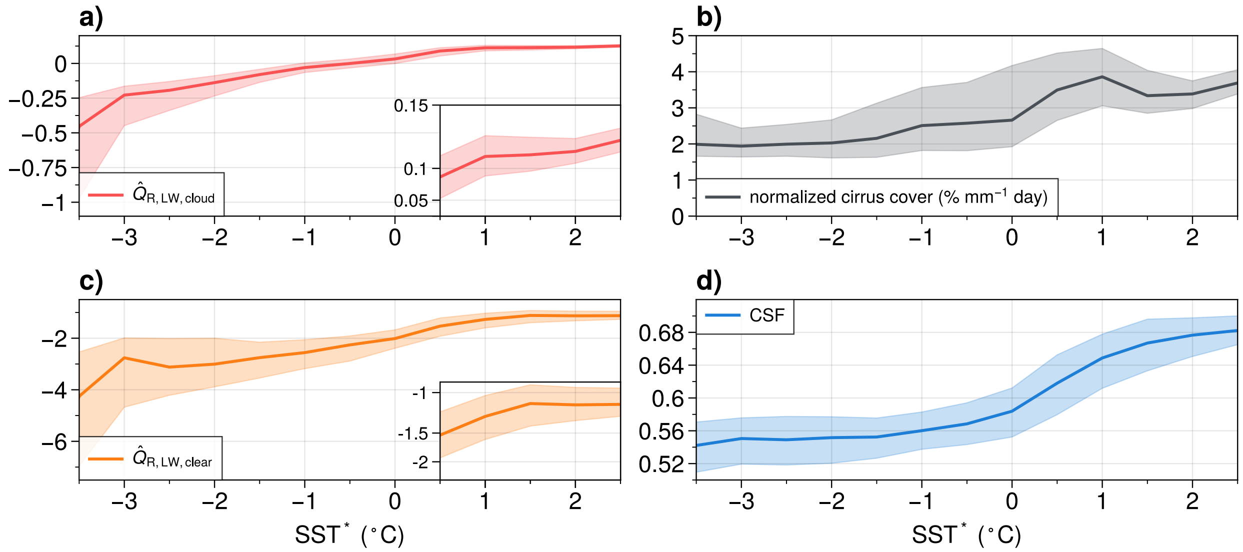

Figure 2.5. As in **Figure 2.3**, but binned by SST* every 0.5°C.

To summarize, it appears that while SST* is a stronger predictor of tropical precipitation, CSF, and clear-sky longwave radiative feedback, SST is a stronger predictor of tropical organized deep convective activity, normalized cirrus ice cloud cover, and longwave radiative feedback due to clouds. To support this argument, individual samples (instead of medians) are used to calculate the Pearson correlation coefficient between $\hat{Q}_{R,LW,cloud}$ and either SST above 26.5°C or SST* above -1°C, which yield 0.75 and 0.72, respectively, which are significantly different utilizing bootstrapping ($p < 0.01$). If focusing on the high-temperature conditions, the correlation coefficients obtained by SST above 28°C and SST* above 0.5°C are 0.37 and 0.22, respectively, which are also statistically different utilizing bootstrapping ($p < 0.01$). These results suggest that SST correlates better with longwave cloud radiative feedback than SST*, especially at higher surface temperatures.

We present a hypothesis for why SST more strongly controls organized deep convective activity and associated cloud radiative feedbacks than SST*. SST* has a strong control on CAPE such that it shapes the large-scale tropical circulation and free-tropospheric relative humidity patterns (e.g., Vecchi & Soden, 2007). However, SST more directly controls low-level moisture content as well as its longwave radiative opacity through Clausius-Clapeyron relationship when assuming invariant relative humidity. Since the occurrence of bifurcation in convective states depends largely on the low-level longwave radiative opacity (Kerry Emanuel et al., 2014), the organization of convection may thus vary more consistently with SST instead of SST*. A caveat of the presented hypothesis is that the radiative-convective instability discussed above requires radiative-convective equilibrium (RCE), but this is only reached nearly 65% of time on monthly, 30° × 30° spatiotemporal scale (Jakob et al., 2019). Nevertheless, the instability may still partly contribute to convective organization, given the presence of cloud-radiative heating in ascending regions that may increase the possibility of bifurcation.

The stronger control of SST on organized deep convective activity and associated cloud radiative feedbacks can only be manifest when the SST does not covary well with SST*, which we now demonstrate to be true at higher temperatures. **Figure 2.6a** shows a bimodal structure in SST*-SST occurrence when both temperatures are high. During La Niña-like months (**Figure 2.6c**), SST is not necessarily the highest when some of the highest values of SST* occur (blue boxes). Similarly, extremely high SST occurs while SST* is relatively low (red boxes) during El Niño-like months. It is also notable that in the green boxes, high occurrences of SST* (e.g., 0.8°C) are accompanied by a large range of SST (28-29.5°C) during El Niño-like months (**Figure 2.6b**), which likely contributes to the flatter $f_{DeepOrg}$ in SST* space than in SST space as discussed above. Additional analysis shows that the Laplacian of SST, which contributes to boundary layer convergence and divergence (Lindzen & Nigam, 1987), is dependent on ENSO along the SST* axis at high SSTs above 28°C and may impose additional control on organized deep convection shown by the somewhat similar patterns in **Figures A2.7d and A2.8d**. However, SST as a stronger predictor is still shown when a fixed range of the magnitudes of the Laplacian of SST is selected (**Figures A2.9-A2.10**), reinforcing the robustness of SST having more control on $f_{DeepOrg}$ than SST*.

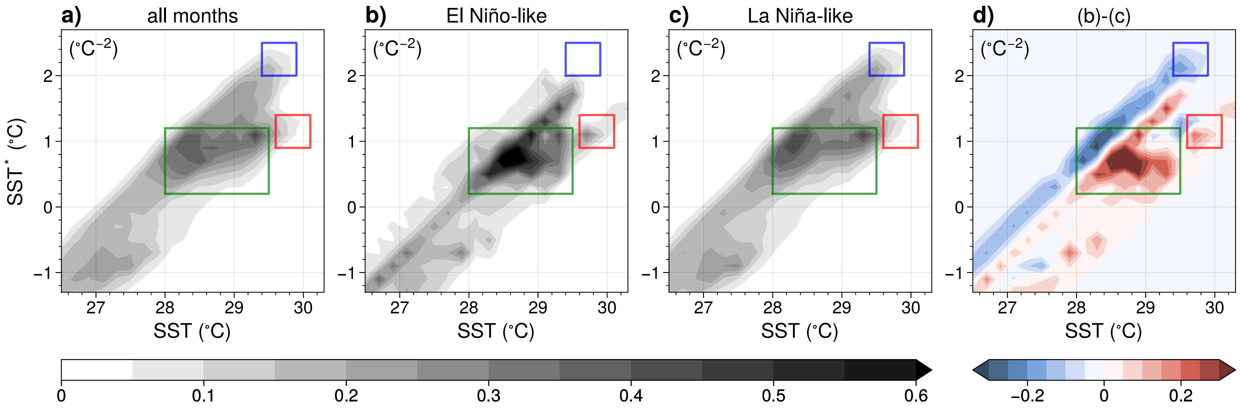

Figure 2.6. The joint probability density function (°C^{-2}) of SST (x-axis) and SST* (y-axis) over 2003-2021 in (a) all months, when (b) MEIv2 ≥ 0.5 (El Niño-like), and (c) MEIv2 ≤ 0.5 (La Niña-like). (d) shows the difference between the probability density function of El Niño-like and La Niña-like conditions, namely the shading of (b) minus that of (c). The reference boxes in (a)-(c) highlight the structures possibly associated with ENSO, as discussed in text.

It should be emphasized that the transition SST and SST* of deep organized convective activity is obtained from the current-state climate, and how the conclusions would hold under a different climate state is unclear. Studies have suggested that the SST that triggers tropical deep convection could vary with tropical mean SST (Hoyos & Webster, 2012; N. C. Johnson & Xie, 2010), which motivates our examination of SST*. However, how the tropical circulation responds to a warming climate is still an area of active investigation (e.g., Held & Soden, 2006; Hoyos & Webster, 2012; Knutson & Manabe, 1995), and how the response of organized deep convection and associated radiative feedbacks play a role in a stronger or weaker circulation response is a topic for a future study.

2.4 Effects of vertical wind shear on the transition SST of $f_{DeepOrg}$ and radiative feedbacks

2.4.1 The transition SST of $f_{DeepOrg}$ versus low-level wind shear

Now the focus is shifted to how nonthermodynamic factors such as low-level wind shear affect tropical $f_{DeepOrg}$ in addition to SST. **Figure 2.7a** shows the means of $f_{DeepOrg}$ jointly binned by SST and the low-level wind shear magnitude, defined between 700 and 925 hPa ($\Delta U_{700\text{-}925}$). This plot demonstrates a decrease in the transition SST for organized deep convection from 28.5°C to 27°C as $\Delta U_{700\text{-}925}$ increases from 2 m s^{-1} to 9 m s^{-1}. The statistical distribution of the SST near the criterion of $f_{DeepOrg} = 0.3$, obtained from data points with $f_{DeepOrg}$ lying in the range of 0.3 ± 0.01 at given shear bins, is further depicted in **Figure 2.7b**. The interquartile range of SST follows the decrease in its median with increasing $\Delta U_{700\text{-}925}$ up to 6 m s^{-1}, where above this the median SST stays nearly constant. This result supports the conclusion that low-level wind shear favors the development of tropical organized deep convection at constant SST, or equivalently, a higher SST is required to produce the same mean $f_{DeepOrg}$ at weaker low-level wind shear. As noted in **Chapter 2.2.1**, the actual value of the criterion (currently 0.3) does not impact the conclusions (**Figure A2.5**). The transition SST* of $f_{DeepOrg}$ has similar behavior as the transition SST in SST*-$\Delta U_{700\text{-}925}$

space, but it decreases less consistently with $\Delta U_{700\text{-}925}$, supporting the conclusion that SST has stronger control on $f_{DeepOrg}$ than SST* (**Figure A2.11**).

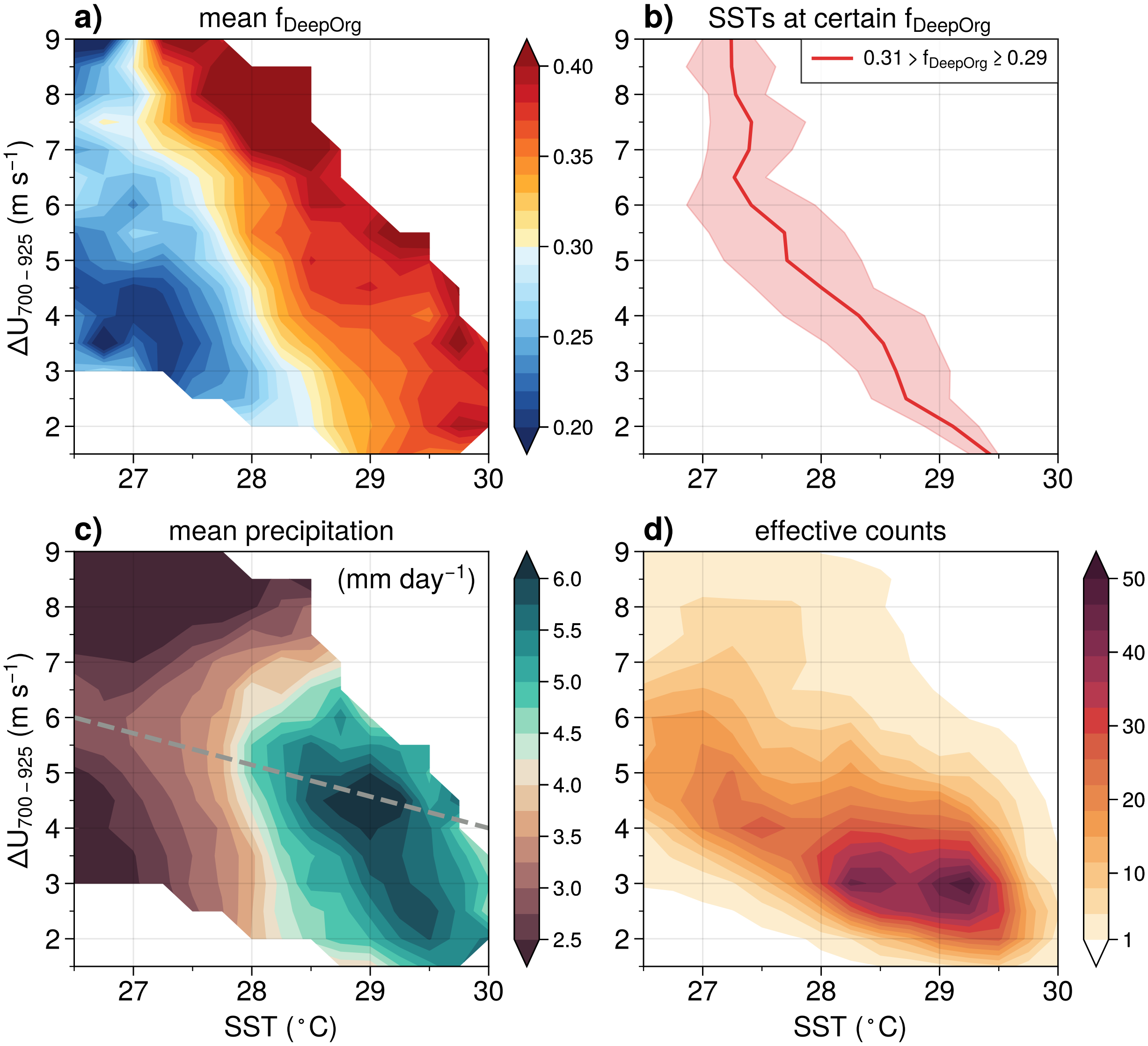

Figure 2.7. (a) The means of $f_{DeepOrg}$ jointly binned by SST every 0.25°C and by $\Delta U_{700\text{-}925}$ every 0.4 m s^{-1}, where bins with effective counts less than one are omitted. The colormap in (a) is centered at 0.3, which is the criterion of the transition SST of $f_{DeepOrg}$. (b) shows the medians (solid line) and the range between the first and third quartiles (shading) of SST binned by $\Delta U_{700\text{-}925}$ every 0.4 m s^{-1} when $f_{DeepOrg}$ lies in 0.3 ± 0.01. (c) as in (a) but showing the mean precipitation rate in mm day^{-1}, and a reference dashed gray line as discussed further in the text. (d) as in (a) but showing the effective count in each bin.

Figure 2.7c shows the means of precipitation jointly binned by SST and $\Delta U_{700\text{-}925}$. The behavior of precipitation with respect to $\Delta U_{700\text{-}925}$ varies as a function of shear values. The mean precipitation increases with $\Delta U_{700\text{-}925}$ below the reference dividing line (dashed gray line), but with opposite behavior above it. Below the dividing line, mean precipitation covaries with mean f_{DeepOrg}, supporting the contention that more precipitation is associated with more organized deep convective activity. The increasing mean precipitation with larger $\Delta U_{700\text{-}925}$ is also consistent with the mesoscale theory that fractionally more low-level inflow into a convection system with convectively unstable air supports more intense precipitation (Alfaro, 2017).

Above the dividing line, comparing **Figures 2.7a and 2.7c** suggests that stronger low-level wind shear supports an increasing relative contribution of organized deep convection to precipitation, but diminishes total precipitation. Possible mechanisms for how higher $\Delta U_{700\text{-}925}$ values support f_{DeepOrg} but inhibit precipitation are suggested in the following. Strong low-level wind shear could deepen and dilute the boundary layer, leading to drying which is unfavorable for convection plumes to maintain their buoyancy (Robe & Emanuel, 2001), and weaken the intensity of organized convection. Figure 6 in Robe and Emanuel (2001) shows a decrease in low-level relative humidity with increasing low-level wind shear observed in cloud-resolving numerical simulations above a critical value of shear equivalent to $\Delta U_{700\text{-}925}$ value of 5 m s^{-1}, strikingly consistent with the dividing line in **Figure 2.6c**. Rotunno et al. (1988) proposed that the shear that exceeds the "optimal state" of squall lines balancing convective cold pools causes convective cells to tilt, in a way such that the low-level air under developing cells experienced rain-induced cooling and reduced CAPE, which reduces the potential intensity of organized convection. The stronger shear that exceeds the optimal state makes convection weaker while still maintaining its persistence (Rotunno et al., 1988), consistent with the finding that mean precipitation but not $f_{DeepOrg}$ decreases at strong low-level wind shear.

2.4.2 The transition SST of $f_{DeepOrg}$ versus mid-level wind shear

How mid-level wind shear affects $f_{DeepOrg}$ over the tropics is also examined. First, it is shown in **Figure 2.8b** that mean $\Delta U_{700-925}$ is largely independent of mid-level wind shear magnitudes defined between 500 and 750 hPa ($\Delta U_{500-750}$) in SST-$\Delta U_{500-750}$ space. The Pearson correlation between $\Delta U_{700-925}$ and $\Delta U_{500-750}$ is low, with a value of 0.14. This supports our motivation to examine mid-level wind shear in addition to low-level wind shear. As shown in **Figures 2.8a and 2.8c**, mid-level wind shear magnitudes ($\Delta U_{500-750}$) do not have a clear effect on mean $f_{DeepOrg}$ and precipitation in SST-$\Delta U_{500-750}$ space, demonstrated by the roughly vertical contours in those mean quantities.

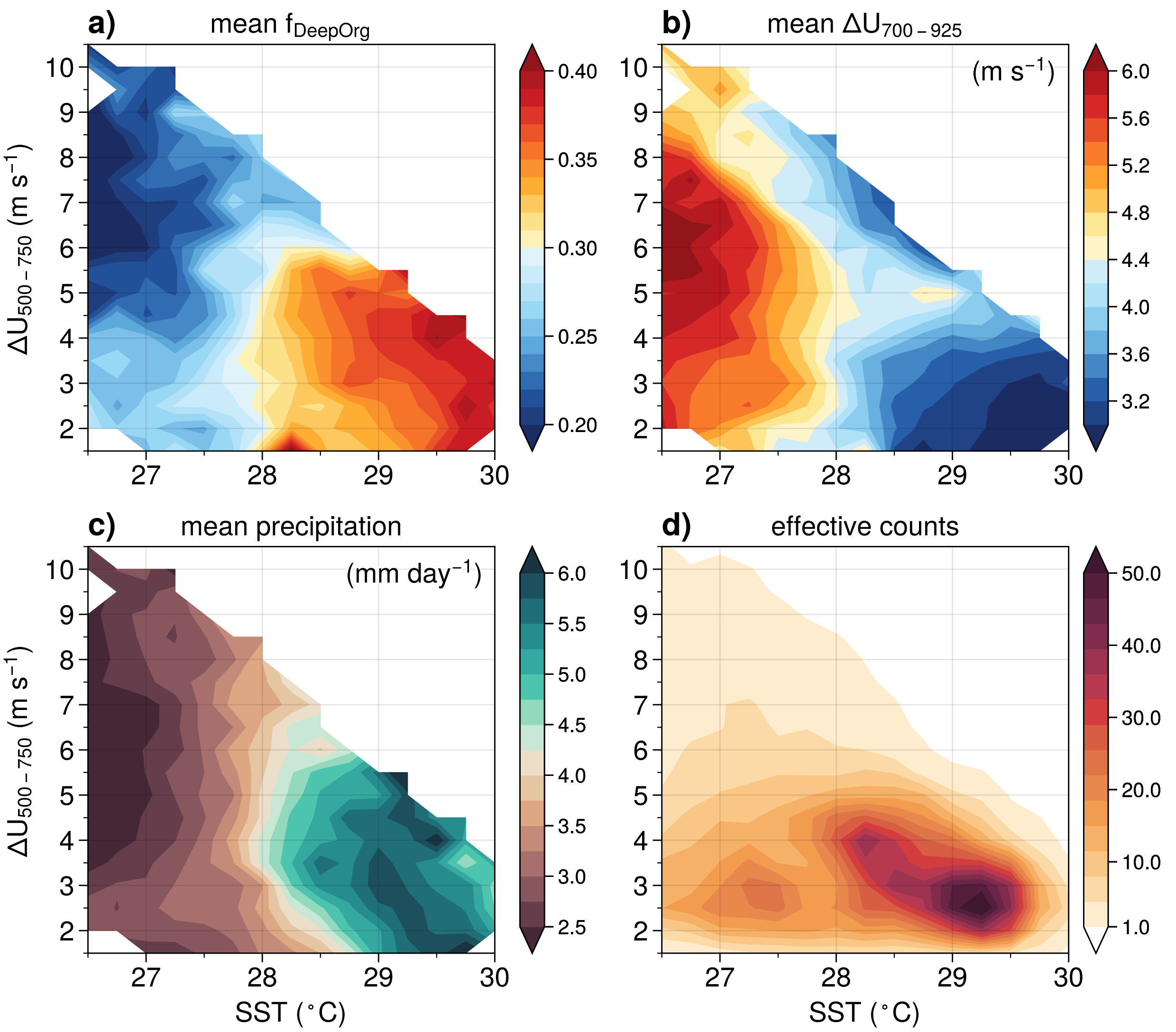

Figure 2.8. As in **Figure 2.7**, but binned by $\Delta U_{500\text{-}750}$ every 0.5 m s^{-1} instead of $\Delta U_{700\text{-}925}$ on the y-axis, and (b) shows the mean $\Delta U_{750\text{-}925}$.

As SST plays the primary role controlling tropical convective organization and precipitation in **Figure 2.8**, a question is whether the effect of mid-level wind shear is truly absent or is hidden in SST-$\Delta U_{500\text{-}750}$ space. When plotting the variables of interest in $\Delta U_{700\text{-}925}$-$\Delta U_{500\text{-}750}$ space, mid-level wind shear larger than 6 m s^{-1} sharply reduces the mean $f_{DeepOrg}$ to below 0.3 and mean precipitation to below 4 mm day^{-1} (**Figures 2.9a, c**). Below $\Delta U_{500\text{-}750}$ values of 6 m s^{-1}, a complicated pattern of mean $f_{DeepOrg}$ appears in **Figure 2.9a** likely due to competing effects originating from the anticorrelation between mean SST and $\Delta U_{700\text{-}925}$ (**Figure 2.9b**). With increasing $\Delta U_{700\text{-}925}$ in $\Delta U_{700\text{-}925}$-$\Delta U_{500\text{-}750}$ space, stronger low-level wind shear favors organized deep convection, but decreasing mean SST accompanied with increasing $\Delta U_{700\text{-}925}$ imposes a parallel inhibition effect.

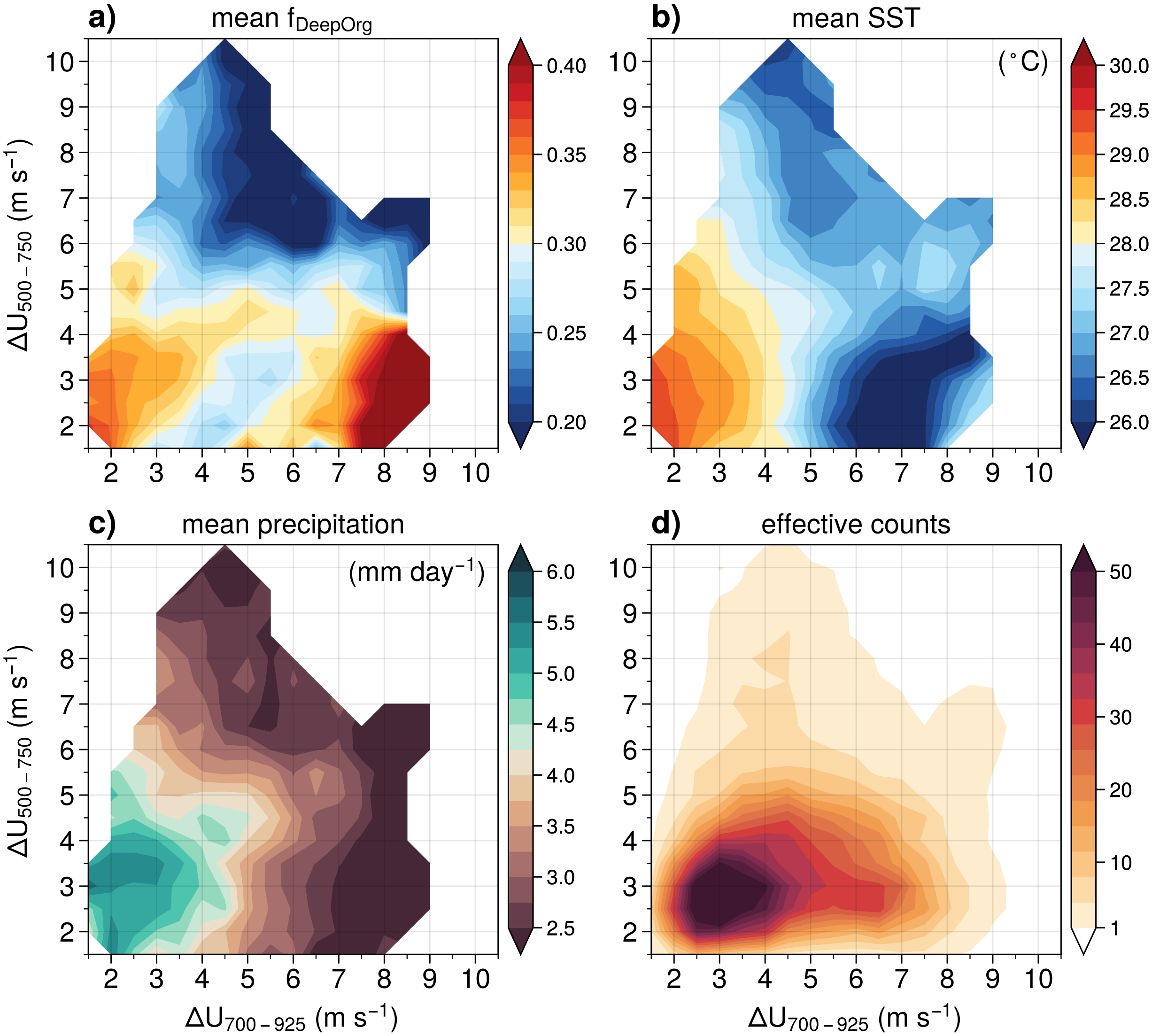

Figure 2.9. As in **Figure 2.7**, but binned by $\Delta U_{700\text{-}925}$ on the x-axis and by $\Delta U_{500\text{-}750}$ on the y-axis every 0.5 m s^{-1} in both axes, and (b) showing the mean SST.

Given the distribution of mean SST, one might conclude that high $\Delta U_{500-750}$ cuts down $f_{DeepOrg}$ and precipitation because lower SST coexists with $\Delta U_{500-750}$ above 6 m s^{-1} (**Figure 2.9b**). However, conditions with both low $\Delta U_{500-750}$ (< 6 m s^{-1}) and high $\Delta U_{700-925}$ (> 5 m s^{-1}) also demonstrate much lower SST but high mean $f_{DeepOrg}$, suggesting a notable independent impact of mid-level wind shear on mean $f_{DeepOrg}$. For mean precipitation (**Figure 2.9c**), since it mainly follows the pattern of mean SST (**Figure 2.9b**), it cannot be concluded whether mid-level wind shear has an impact on it. This analysis implies a secondary but significant effect by strong mid-level wind shear inhibiting tropical organized deep convection compared to low-level shear and SST.

A possible physical explanation for why strong mid-level shear inhibits tropical organized deep convection is introduced here. An observational study hypothesized that very-strong mid-level wind shear decouples the moisture supply of the stratiform region of a mesoscale convective system from its convective updraft, inhibiting mesoscale organization (Barnes & Houze, 2013). While the study only examined this mechanism in the context of the MJO, our analysis suggests that similar physical mechanisms might be relevant on monthly timescales over global tropical oceanic regions.

2.4.3 Cloud radiative feedback following $f_{DeepOrg}$ and vertical wind shears

A robust control of vertical wind shear on tropical organized convection and precipitation is suggested in **Chapters 2.4.2-2.4.3**. Here, we examine a possible connection between vertical wind shears and strength of the longwave radiative feedback (as defined in **Chapter 2.3.2**) associated with the precipitating convective systems.

Variables related to longwave radiative heating are plotted in SST-$\Delta U_{700\text{-}925}$ space. Shading in **Figure 2.10a** shows the tropospheric longwave cloud radiative feedback ($\hat{Q}_{R,LW,cloud}$), which increases with both SST and $\Delta U_{700\text{-}925}$ and generally follows the pattern of mean f_{DeepOrg} (contours; or see **Figure 2.7a**). Comparing **Figure 2.10b** to **2.10a** shows that the mean normalized cirrus cover qualitatively follows the mean $\hat{Q}_{R,LW,cloud}$ as both SST and $\Delta U_{700\text{-}925}$ increase. The results suggest that more extensive anvil clouds generated by more organized deep convection produce stronger column longwave radiative heating per unit precipitation, aided by higher SST and stronger low-level wind shear in fostering convective organization. The magnitudes of mean $\hat{Q}_{R,LW,cloud}$ fluctuates by ~0.1 with varying $\Delta U_{700\text{-}925}$, which may be relevant to a previous study suggesting that outgoing longwave radiation changes with vertical wind shear by the order of 10% amount of latent heat in tropical western Pacific (J.-L. Lin & Mapes, 2004a).

However, upon closer inspection the relationship between normalized cirrus cloud cover and $\hat{Q}_{R,LW,cloud}$ variations in the region of positive $\hat{Q}_{R,LW,cloud}$ is not perfect, which may be attributed to changes in other high cloud types and cloud properties. **Figure 2.11d** suggests that normalized cirrostratus ice cloud cover maximizes at an SST of 28°C and $\Delta U_{700\text{-}925}$ of 7 m s^{-1}, and decreases with higher $\Delta U_{700\text{-}925}$. The mean effective temperature of cirrostratus also increases from 238.4 to 240.3 K from $\Delta U_{700\text{-}925}$ values of 7 to 8 m s^{-1} at 28°C SST (**Figure 2.11e**), along with a decrease in mean effective cloud height (**Figure 2.11f**), which would impose a weakening effect of cloud longwave heating with increasing low-level wind shear when cloud cover is fixed. These combined effects likely cause the $\hat{Q}_{R,LW,cloud}$ to weaken at larger $\Delta U_{700\text{-}925}$, which cannot be explained by the mean normalized cirrus cover alone.

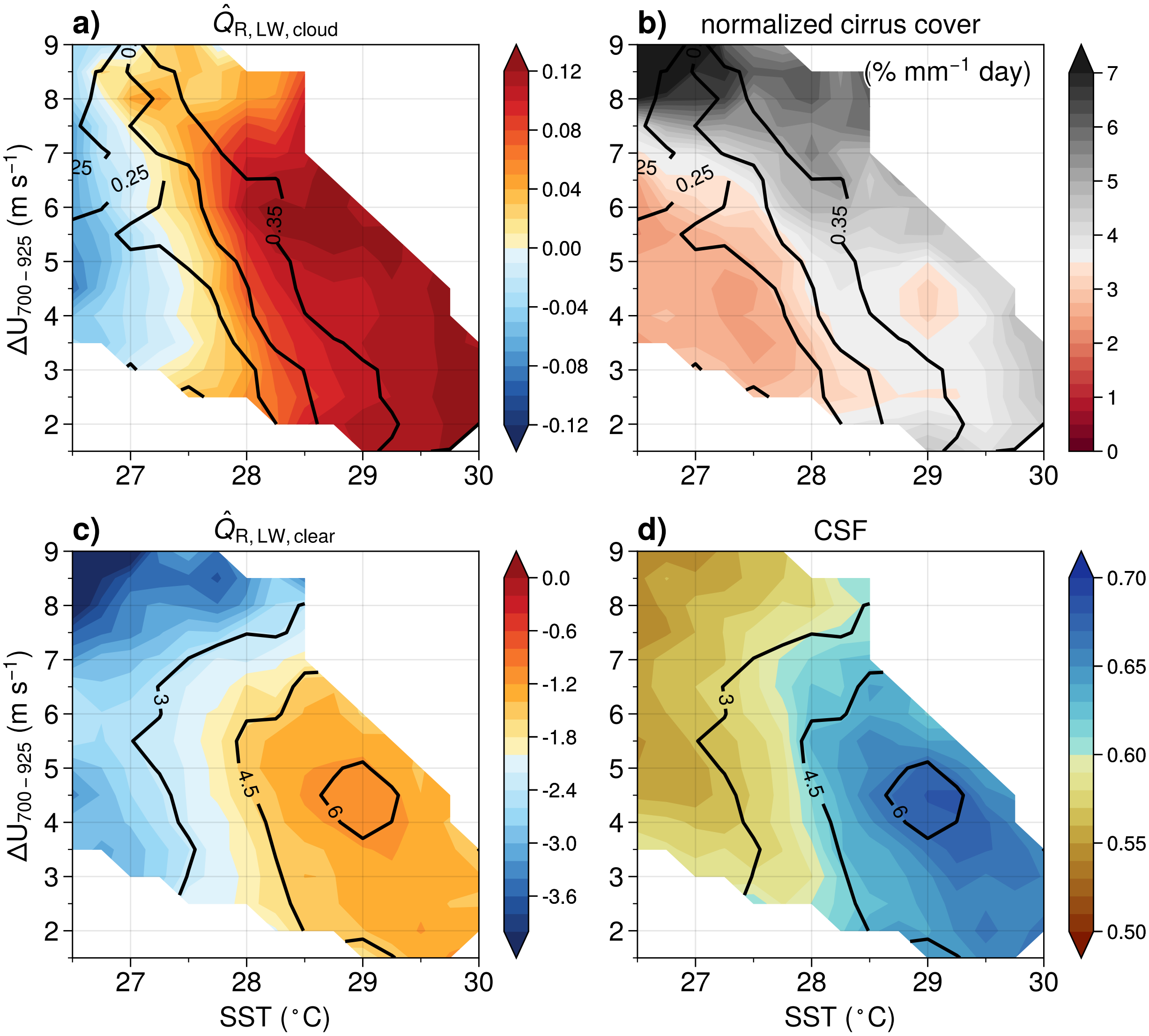

Figure 2.10. As in **Figure 2.7a**, but shading showing the means of (a) $\hat{Q}_{R,LW,cloud}$ (dimensionless), (b) normalized cirrus ice cloud area (% mm^{-1} day), (c) $\hat{Q}_{R,LW,clear}$ (dimensionless), and (d) CSF (dimensionless). Contours in (a-b) indicate the isolines of 0.25, 0.3, and 0.35 (as labeled) in the means of $f_{DeepOrg}$. Contours in (c-d) indicate the isolines of 3, 4.5, and 6 mm day^{-1} (as labeled) in the means of precipitation.

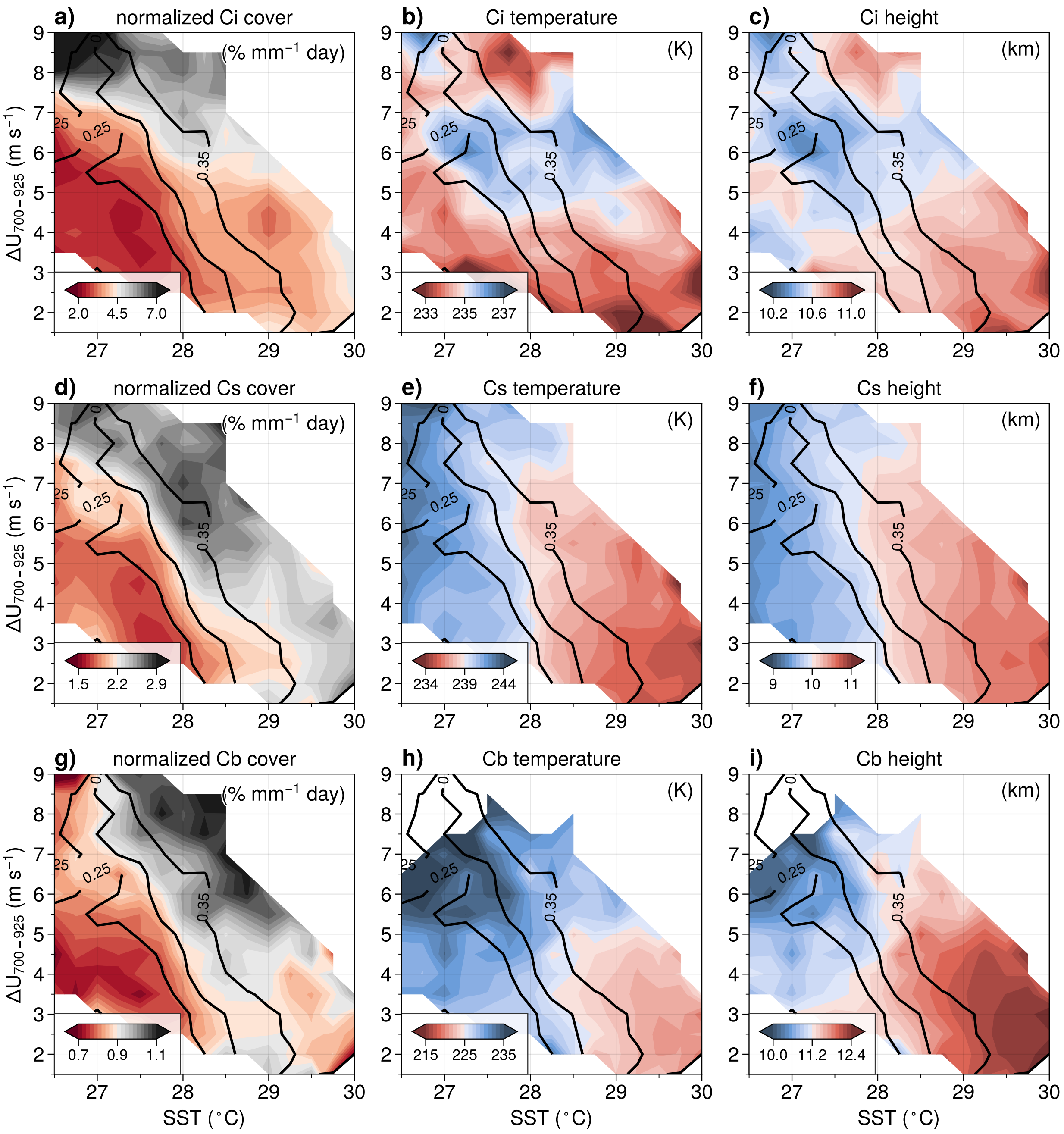

Figure 2.11. As in **Figure 2.10b**, but with shading indicating the means of (left column) precipitation-normalized ice cloud cover in % mm^{-1} day, (middle column) effective ice cloud temperature in K, and (right column) effective ice cloud height in km. The top, middle, and the bottom row shows those of cirrus (Ci), cirrostratus (Cs), and the top part of cumulonimbus (Cb), respectively. Note that the colormap of mean effective ice cloud temperature is inverted, such that warm colors indicate the stronger warming effect on the troposphere by longwave cloud radiative heating when cloud temperature is lower.

We emphasize that **Figure 2.11** shows the interesting finding that certain high cloud properties depend largely on low-level wind shear in addition to SST. Mean normalized cirrus cover is not only higher when SST exceeds 28°C, but also when low-level wind shear increases, a behavior especially robust above $\Delta U_{700\text{-}925}$ values of 5 m s^{-1} (**Figure 2.11a**). Mean cirrus temperature and height varies mainly with $\Delta U_{700\text{-}925}$ in a nonlinear manner, such that temperature maximizes in a $\Delta U_{700\text{-}925}$ range of 5-7 m s^{-1} (**Figures 2.11b-c**). As discussed in the previous paragraph, cirrostratus has a mild cloud cover change and a sudden mean temperature change with $\Delta U_{700\text{-}925}$ at 7 m s^{-1} (**Figures 2.11d-e**; note the greater temperature scale in colorbar than for cirrus). Mean cumulonimbus ice cloud cover increases with low-level wind shear, especially for greater than 5 m s^{-1}, along with increasing mean cloud top temperature (**Figures 2.11g-h**). All of these interesting dependences of cloud types and cloud properties on SST and shear would have implications for the longwave radiation budget of the atmosphere. A detailed investigation of the interesting cloud features and resulting radiative feedbacks controlled by vertical wind shear and SST requires a separate study. Prior studies have found that stronger deep-tropospheric wind shears can contribute to an increase in cloud cover by a reduction of horizontal overlap between clouds (Di Giuseppe & Tompkins, 2015; Saxen & Rutledge, 2000; Sulak et al., 2020), although how low-level wind shear contributes to this effect is not clear.

Clear-sky longwave radiative feedback ($\hat{Q}_{R,LW,clear}$; shading in **Figure 2.10c**) closely follows the moisture content of the atmosphere (shading in **Figure 2.10d**) and mean precipitation (contours in **Figures 2.10c-d**; or see **Figure 2.7c**) in SST-$\Delta U_{700\text{-}925}$ space. These relationships are consistent with the clear-sky effect of enhanced water vapor trapping longwave radiative flux in the troposphere, and precipitation being closely coupled with CSF (Bretherton et al., 2004).

2.5 Discussion

We compare the present results to previous observational studies of convective organization. Prior studies have proposed that more-organized deep convection leads to mid-tropospheric drying and stronger clear-sky longwave radiative cooling (Bony et al., 2020). However, the present study shows increasing mean $\hat{Q}_{R,LW,clear}$ (i.e., decreasing cooling per unit precipitation) and CSF following higher mean f_{DeepOrg}, at least for shear below 6 m s^{-1} (**Figures 2.7c and 2.10c-d**). Anvil cloud cover has been proposed to decrease with convection that is more organized at a fixed SST and precipitation (Stein et al., 2017), and anvil cover in an individual contiguous cloud has been shown to decrease when the underlying SST increases (Igel et al., 2014). Nonetheless, the present study shows increasing mean $\hat{Q}_{R,LW,cloud}$ and normalized cirrus ice cloud cover following higher mean f_{DeepOrg} that increases with $\Delta U_{700\text{-}925}$ and SST (**Figures 2.7a and 2.10a-b**). The discrepancies arise since quantities are examined by per unit precipitation in this study, representing the "efficiency" through which cloud covers and radiative effects are produced per unit precipitation, whereas previous studies examine the total effects. Relevantly, weaker precipitation produced by more aggregated convection at constant SST (Tobin et al., 2012) has been suggested to be an effect of not considering the anticorrelation between the area of convection and the degree of aggregation (Angulo-Umana & Kim, 2023; Semie & Bony, 2020). These apparent discrepancies may also partly originate from the different definitions of organized deep convection used, and from different foci on thinner cirrus and thicker anvil clouds. The literature discussed above considers the connectivity and "clumpiness" of clouds with low brightness temperatures in 10° × 10° boxes when defining convective organization, a scale larger than contiguous convective cells. On the other hand, the present method classifies a 1° × 1° scene as organized deep convective partly when it has a high stratiform rainfall contribution (c.f. Table 1;

Elsaesser et al., 2010), putting more weight on the precipitation structures that have obvious traits of mesoscale convective systems (Elsaesser & Kummerow, 2013), instead of aggregation on larger spatial scales. It should be emphasized again that the 30° × 30° domains are used to obtain average rain contributions from DeepOrg scenes that have mesoscale organization traits, but not examining the aggregation on a 30° × 30° scale.

While the clustering of self-similar tropical precipitating scenes explains a large fraction (~60%) of the variability of tropical precipitation (Elsaesser et al., 2010), the unexplained ~40% also points out the limitation of the method. This is partly evident in the strong low-level shear condition discussed in **Chapter 2.4.1**, which favors deep convection being organized while diminishing mean precipitation (**Figure 2.7**). The detailed variabilities in the horizontal shape or the intensity of organized deep convection that affect large-scale precipitation can also potentially affect radiative feedbacks, which is an important topic for future study.

In this study, monthly means over 30° × 30° domains in the tropics are examined due to limited data availability. To directly investigate the physical mechanisms discussed in this paper of how SST and vertical wind shear both affect convective organization and precipitation, such as the dynamical balance between convective cold pool and background wind profile, data with finer spatiotemporal resolution is required. It is thus desired to examine those mechanisms in a future study when data with sufficient resolution is available or by performing numerical simulations. Note that the study does not exhaustively discuss possible factors impacting tropical convective organization. Other meteorological factors, such as the presence of a coastal environment, would weaken the relationships between f_{DeepOrg}, SST, and wind shear (**Figure A2.12**), consistent with a previous study suggesting a different CSF-precipitation relationship due to coastal processes (Bergemann & Jakob, 2016).

2.6 Summary

The present study provides a global observational assessment of the relationships among tropical organized deep convection, precipitation, SST and SST*, vertical wind shear, and associated atmospheric radiative heating. Convective rain states (CRS) are derived using TRMM and GPM precipitation radar. The fractional contribution of organized deep convective CRS to total precipitation, $f_{DeepOrg}$, is used to measure tropical organized deep convective activity on monthly timescales and by 30° × 30° spatial means. $f_{DeepOrg}$ as a fractional precipitation contribution indicates variability in both the relative frequency and intensity of organized deep convective activity compared to other types of tropical precipitating systems.

Both SST and vertical wind shear are important regulators of tropical convective organization and precipitation. Median $f_{DeepOrg}$ shows a pick-up behavior with respect to SST above 27°C, and reaches a value of 0.3 at which the transition SST of organized deep convection is defined at 28.1°C (**Figure 2.2a**). As organized deep convection tends to produce more anvil and cirrus clouds, precipitation-normalized cirrus ice cloud cover and tropospheric longwave cloud radiative feedbacks ($\hat{Q}_{R,LW,cloud}$) also increases with SST above 27°C (**Figures 2.3a-b**), which help support upward motion associated with convective systems. Although SST* is a better indicator of tropical precipitation amount as shown in **Figure 2.4c** and previous studies (A. H. Sobel et al., 2002), SST* has a weaker control on $f_{DeepOrg}$ and $\hat{Q}_{R,LW,cloud}$ than SST (**Chapter 2.3.3**). Particularly at higher surface temperatures, SST and SST* decouple under the influence of interannual variability such as ENSO (**Figure 2.6**). The dependence of low-level moisture content and longwave radiative opacity on SST rather than SST*, which aids the bifurcation of convective states (Kerry Emanuel et al., 2014), may explain why tropical convective organization follows SST more than SST*.

Low-level wind shear ($\Delta U_{700-925}$) favors organized deep convective activity, evident from the transition SST of $f_{DeepOrg}$ decreasing from 28.5°C to 27°C as $\Delta U_{700-925}$ increases from 2 to 9 m s^{-1} (**Figures 2.7a-b**), consistent with the theories of low-level wind shear helping the development of mesoscale convection (Houze, 2004 and reference therein). In general, longwave cloud radiative feedbacks support organized convection as shear increases, such that larger mean $\hat{Q}_{R,LW,cloud}$ is present with higher $\Delta U_{700-925}$ at constant SST, following the increase in mean $f_{DeepOrg}$ (**Figures 2.10a-b**). Increased $\hat{Q}_{R,LW,cloud}$ with higher $\Delta U_{700-925}$ and SST is mainly promoted by increased cirrus ice cloud cover per unit precipitation, but it is also shaped by complicated variations in normalized cirrostratus ice cloud cover and cloud temperature with respect to low-level wind shear (**Figure 2.11**).

Mid-level wind shear ($\Delta U_{500-750}$) that is too strong (> 6 m s^{-1}) is shown to inhibit tropical organized deep convective activity (**Figures 2.8-2.9**). Similar conclusions were made in a previous study examining the cycle of the MJO over the Indo-Pacific warm pool, in which they suggest that a cut-off of moisture supply from convective regions to stratiform regions occurs in organized convective systems when strong mid-level wind shear is in presence (Barnes & Houze, 2013). Our result suggests that this mechanism also generally holds in the tropics on monthly timescales.

Precipitation has a more complicated relationship with vertical wind shear. When low-level wind shear is weaker, tropical mean precipitation increases with $\Delta U_{700-925}$ at constant SST, accompanied by the increase in mean $f_{DeepOrg}$. However, mean precipitation decreases with $\Delta U_{700-925}$ at higher low-level wind shear (**Figure 2.7c** above the reference line). This nonlinear relationship is also shown in mean column saturation fraction (CSF) and mean longwave clear-sky radiative feedback ($\hat{Q}_{R,LW,clear}$) as they are tightly connected to precipitation (Bretherton et al., 2004). It is possible that under conditions with very strong low-level wind shear, moisture in tropospheric boundary layer is diluted (Robe & Emanuel, 2001), or that the shear cannot be balanced by the cold pools produced by mesoscale convective systems (Rotunno et al., 1988), both of which could inhibit the potential intensity of convection by reducing effective CAPE while the latter mechanism still supports the presence of weaker organized convective systems that is reflected in increased mean f_{DeepOrg}.

Few observational studies have surveyed the large-scale controlling factors of organized deep convection over the global tropics. While SST is a robust indicator of large-scale convective instability, the present study demonstrates robust effects of vertical wind shear on the organization of deep convection and precipitation These effects likely influence subsequent cloud properties and radiative feedbacks in the tropics. (e.g., Hsiao, Hwang, et al., 2022). Differences in how global climate models represent high clouds and associated radiative heating in tropical ascending regions may contribute to spread in future tropical SST pattern projections, and could be a cause of why, for example, climate models tend to produce an El Niño-like warming pattern versus the La Niña-like tropical SST trend that is observed (S. Lee et al., 2022). The results provide an observational reference for global climate models on the relationship between large-scale meteorological conditions and cloud radiative effects, with convective organization being a possible underlying physical cause. Tropical cloud radiative feedbacks not only directly affect local radiative budgets and the maintenance of tropical variability (Adames & Maloney, 2021), but also help drive circulations that affect remote parts of the globe (Hsiao, Barnes, et al., 2022; Hsiao, Hwang, et al., 2022). How large-scale SST and vertical wind shear affect organization of tropical deep convection can also be compared to global cloud-resolving simulations, such as those produced by the DYnamics of the Atmospheric general circulation Modeled On Non-hydrostatic Domains models (DYAMOND; Stevens et al., 2019), to elucidate how biases in convection may lead to biases in global climate patterns.

CHAPTER 3

Tropical Longwave Cloud-radiative Feedback Derived by Different Precipitation Datasets[2]

3.1 Introduction

Tropical disturbances affect global extreme weather and the hydrological cycles through their moist dynamics and associated teleconnections (e.g., Ferrett et al., 2020; Frank & Roundy, 2006; Hsiao, Barnes, et al., 2022; Maloney & Hartmann, 2000; K-C Tseng et al., 2018). Convective systems and cloudiness are commonly coupled with tropical equatorial waves (Takayabu, 1994; M. Wheeler & Kiladis, 1999), and the longwave cloud-radiative feedback generated by convective clouds serves as an important mechanism modifying the development of these waves. In the Madden-Julian oscillation (MJO), the presence of convective clouds traps more longwave radiation in precipitating regions, imposing an anomalous heating effect on the atmosphere (Del Genio & Chen, 2015; R. H. Johnson et al., 2015; R. H. Johnson & Ciesielski, 2000; J.-L. Lin & Mapes, 2004b; Ma & Kuang, 2011). The radiative heating enhances upward velocity near the precipitation maximum, consistent with weak-temperature-gradient theory, which helps moisten the atmosphere and destabilize the MJO (Adames & Kim, 2016; Andersen & Kuang, 2012; Benedict et al., 2020; Chikira, 2014; Crueger & Stevens, 2015; Hu & Randall, 1994; M.-I. Lee et al., 2001; Raymond, 2001; A. Sobel et al., 2014; A. Sobel & Maloney, 2012; B. O. Wolding & Maloney, 2015; Zurovac-Jevtić et al., 2006). Longwave cloud-radiative feedback has also been suggested to support tropical cyclones (Ruppert et al., 2020), and to damp modeled

---

- [2] This chapter contains material that is published in *Geophysical Research Letters* as: Hsiao, W.-T., & Maloney, E. D. (2024). The Longwave Cloud-Radiative Feedback in Tropical Waves Derived by Different Precipitation Data Sets. *Geophysical Research Letters*, *51*(11), e2024GL109143.

equatorial Kelvin waves but support equatorial Rossby waves (Andersen & Kuang, 2012; Benedict et al., 2020; Medeiros et al., 2021).

The longwave cloud-radiative feedback can be described and measured in various ways. In moisture mode theories of convectively coupled disturbances such as the MJO, the feedback is represented by an enhancement factor of column-integrated convective heating due to cloud-radiative interaction (e.g., Ž. Fuchs & Raymond, 2002; Inoue et al., 2020; Kim et al., 2015; J.-L. Lin & Mapes, 2004b; Raymond, 2001; A. Sobel & Maloney, 2012; Sugiyama, 2009). Prior studies have shown that the radiative feedback is dependent on zonal wavelength (Adames & Kim, 2016) and precipitation magnitude (Kim et al., 2015). The feedback has also been incorporated into the "effective" gross moist stability parameter that effectively reduces the efficiency of moist static energy discharge from the column in regions of convection (e.g., Bretherton & Sobel, 2002; Raymond et al., 2009; Su & David Neelin, 2002). To specify our scope, this paper focuses on the feedback defined as the proportional factor between anomalous radiative heating and precipitation.

Accurately determining the magnitude of the radiative feedback is important for developing theories and better simulations of climate variability and tropical disturbances. Cloud-radiative heating is coupled with interannual and decadal variability in their internal dynamics (e.g., Hsiao, Hwang, et al., 2022; Rädel et al., 2016). Certain moisture mode theories of the MJO rely on the presence of radiative feedbacks to help maintain the moisture field that supports MJO convection (e.g., Adames & Kim, 2016; Jiang et al., 2020; A. Sobel & Maloney, 2012; C. Zhang et al., 2020). However, estimating the longwave cloud-radiative feedback using observations is difficult. Accurate observations of outgoing longwave radiation (OLR) are needed, which have been obtained through passive remote sensing by spaceborne satellites (Doelling et al., 2016; H.-T. Lee et al., 2007; Liebmann & Smith, 1996). In contrast, obtaining accurate global, continuous observations of surface precipitation are challenging due to scarce in-situ observations and large uncertainties in satellite retrievals, especially in oceanic regions that occupy the majority area in the tropics (e.g., Bolvin et al., 2021; Prakash et al., 2013; Prakash & Gairola, 2014; Prigent, 2010).

In this paper, we examine the sensitivity of the longwave cloud-radiative feedback using two versions of Global Precipitation Climatology Project (GPCP) products and the same OLR dataset, including comparisons to ground-based radar observations. Global climate-quality gridded precipitation products have been extensively used in studies of large-scale tropical systems and climate, especially for theoretical studies to determine model feedback parameters. While earlier versions of precipitation datasets [e.g., Xie and Arkins (1997), GPCPv1.3] rely on passive remote sensing of satellites, the recently updated GPCPv3.2 is believed to be more accurate by including observations of active remote sensing (**Chapter 3.2.1**). This study examines how much the implied radiative feedback is modified by this update. We will show that while the feedback magnitudes calculated are similar by GPCPv1.3 and earlier precipitation datasets as in prior studies (e.g., Adames & Kim, 2016; Inoue et al., 2020; Kim et al., 2015; J.-L. Lin & Mapes, 2004b), GPCPv3.2 yields a distinctly weaker feedback.

3.2 Methodology

3.2.1 Data

Global daily precipitation products, GPCP version 1.3 (GPCPv1.3; Huffman et al., 2001) and version 3.2 (GPCPv3.2; Huffman et al., 2023), are used. The main update for GPCPv3.2 is replacing the Threshold Matched Precipitation Index (TMPI) with the Integrated Multi-satellite Retrievals for GPM (IMERG) product, associated with inclusion of spaceborne precipitation radar observations from the Tropical Rainfall Measuring Mission (TRMM; Kummerow et al., 1998) and the Global Precipitation Mission (GPM; Hou et al., 2014). GPCPv3.2 has been shown to outperform GPCPv1.3 in oceanic regions in frequency of occurrence at different surface rain rates (Z. Li et al., 2023). To obtain the non-dimensional radiative feedback, precipitation rates can be represented in W m^{-2} instead of mm day^{-1} by multiplying by the latent heat of vaporization of water (L_v) and doing a unit conversion to mass using the density of water.

Negative anomalies of National Oceanic and Atmospheric Administration Interpolated OLR (NOAA OLR; Liebmann & Smith, 1996) are used as a proxy for anomalous atmospheric column-integrated radiative heating. This allows direct comparison to results of previous studies (e.g., Adames & Kim, 2016; J.-L. Lin & Mapes, 2004b). Two other OLR products that include satellite observations independent from those used by NOAA OLR, the NOAA Climate Data Record (CDR) of Daily OLR Version 1.2 (H.-T. Lee et al., 2007), and Clouds and the Earth's Radiant Energy System (CERES) synoptic 1-degree (SYN1deg) Edition 4.1 observed daily OLR (Doelling et al., 2016), are also used to test the sensitivity to the results to OLR products (Figures S1-S3 in the Supplemental Material). European Centre for Medium-Range Weather Forecasts Reanalysis v5 (ERA5; Hersbach et al., 2020) is also used to inform how the radiative feedback interacts with other atmospheric fields. All datasets above are regridded conservatively onto the 1° × 1° grid of NOAA OLR within 15°S-15°N and during 1 September 2000 to 31 August 2021 prior to all analyses.

Precipitation estimation from two ground-based radars is used for comparison to GPCP products. The Kwajalein Polarimetric S-band Weather Radar (KPOL; Schumacher & Houze, 2000) located at 167.73°E, 8.72°N on Kwajalein Atoll provides surface precipitation rate retrieved by the HIDRO algorithm (Cifelli et al., 2011). The National Center for Atmospheric Research (NCAR) S-band dual-polarization Doppler radar (S-Pol; S and Ka bands; Keeler et al., 2000) employed at

0.63°S, 73.10°E on Gan Island during the DYNAMO/CINDY/AMIE field campaign, referred to as S-Pol-Gan in this study, provides surface precipitation rate retrieved by a Z-R relation (Feng et al., 2014; Rutledge et al., 2018). Both radars provide 1-km gridded versions of daily precipitation over a scanning radius of 150 km. Data during 1 April 2014 - 31 December 2021 and 1 October 2011 - 15 January 2012 are used from KPOL and S-Pol-Gan, respectively. For direct comparison, both GPCP products and OLR are regridded onto the same grid as in the radar products, and each daily and spatial mean over the whole scanned area is used to create a time series for temporal filtering as described in the following subsection.

3.2.2 Signal filtering

For **Chapter 3.3.2**, a 20-100 day Lanczos band-pass filter with a 101-day window is applied to precipitation and radiative heating rates to isolate signals relevant to the MJO, with further refinements by zonal wavenumber per unit circumference of the Earth (k). The associated longwave-radiative feedback is then calculated as the negative of the slope of linearly regressed OLR onto precipitation anomalies. For validation using S-Pol-Gan, the above procedure is similarly performed but using a 30-60 day filter to obtain sufficient data points given the relatively short time range of the data.

In **Chapter 3.3.3**, the relationship between OLR and precipitation in other parts of wavenumber-frequency (k-ω) space is also examined. Following the harmonic analysis in Wheeler and Kiladis (1999), we calculate the wave-form OLR amplitude (R), precipitation amplitude (P), and the phase shift between wave-form OLR and precipitation (φ_R) in k-ω space using the procedure published by Hayashi (1971) as described in **Appendix B1**. The radiative feedback parameter in k-ω space, $r(k,\omega)$, is calculated at the peak of precipitation:

$$r = R\cos(\varphi_R)/P \tag{3.1}$$

Compared to estimating the feedback parameter by directly dividing R by P in spectral space (e.g., Inoue et al., 2020), a non-zero phase lag φ_R would lead to a smaller feedback parameter r.

To obtain the variability of meteorological variables of interest associated with the precipitation anomalies in certain tropical waves, their regressions onto wave-associated precipitation are calculated as described in **Appendix B1**. Details of statistical significance tests are described in **Appendix B2**.

3.3 Results

3.3.1 Differences in precipitation and the climatological radiative feedback

General differences between the two GPCP precipitation products are first examined (**Figure 3.1**). **Figure 3.1a** compares the global annual-mean precipitation between the two versions of GPCP. While their spatial patterns are qualitatively similar (**Figures A3.1a-b**), GPCPv3.2 has generally higher precipitation at the locations of maximum precipitation, such as in the Indo-Pacific warm pool, the Southern Pacific Convergence Zone (SPCZ), and the Inter-Tropical Convergence Zone (ITCZ). The climatological global tropical radiative feedback is examined in **Figure 3.1b**, calculated as in Peters and Bretherton (2005) by linearly regressing OLR onto precipitation using all grid points in **Figure 3.1a** with precipitation ≥ 50 W m^{-2}. Although GPCPv3.2 yields slightly weaker global radiative feedback due to its generally higher annual-mean precipitation (**Figure 3.1a**), the feedback difference yielded by the two versions of GPCP is subtle (0.02).

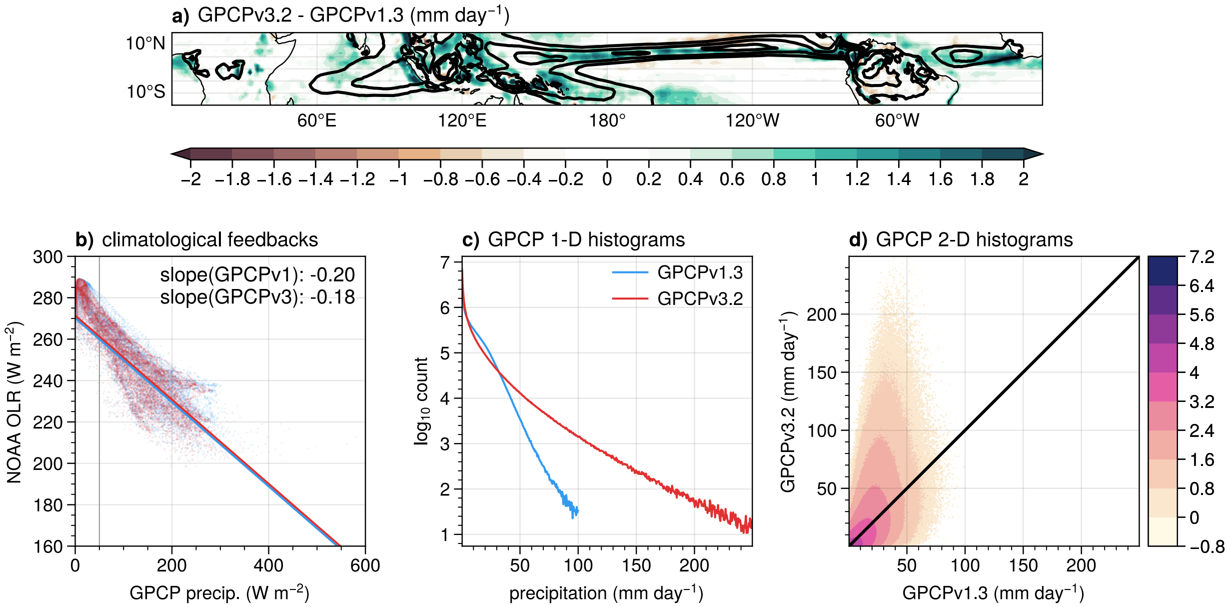

Figure 3.1. (a) global annual-mean precipitation from (contour) GPCPv1.3 at 5, 7, 9 mm day^{-1} and (shading) GPCPv3.2 minus GPCPv1.3 in mm day^{-1}. (b) a scatter plot of NOAA OLR versus precipitation of (light blue) GPCPv1.3 and (dark red) GPCPv3.2 in W m^{-2} using every grid point in (a), and the climatological feedback calculated using data with precipitation rates above 50 W m^{-2} (vertical gray lines) annotated at the upper-right corners with the associated linear-fit lines. (c) histograms of precipitation observations in GPCPv1.3 and v3.2 over the tropics (15°S-15°N), binned every 0.5 mm day^{-1}. (d) a joint histogram of both products with colors indicating log$_{10}$ of counts, and a one-to-one black line for reference.

Although the annual-mean maps of the two GPCP products are similar, their daily variability is not. **Figure 3.1c** demonstrates a very different pattern in the histogram of observed surface precipitation rates in GPCPv1.3 and v3.2, with GPCPv3.2 having more counts above 32 mm day^{-1}. A joint histogram of the two GPCP precipitation products shows consistent results (**Figure 3.1d**), the count distribution is skewed toward higher values of GPCPv3.2 above the one-to-one line. These differences are similar to the findings of Li et al. (2023). Increased occurrence of daily precipitation at higher values implies a weaker radiative feedback in tropical convective disturbances, which is the main focus in the following subchapters.

3.3.2 Precipitation and radiative feedback in the MJO

Precipitation and its longwave radiative feedback associated with the MJO are now examined. The radiative feedback is calculated, as shown in **Figure 3.2**, for a direct comparison with Adames and Kim (2016) using 20-100 day filtered data in the Indo-Pacific warm pool (60°E-180°, 15°S-15°N) where MJO activity is strongest (e.g., as in Hsiao et al., 2020). Without separating by zonal wavenumber, GPCPv1.3 yields a feedback magnitude of 0.15 (**Figure 3.2a**), whereas GPCPv3.2 yields 0.09 (**Figure 3.2b**), about half of GPCPv1.3. It is likely that the greater occurrence of heavy precipitation observed in GPCPv3.2 compared to GPCPv1.3 leads to the smaller regression slope of OLR onto precipitation on 20-100 day timescales. The updated estimate of the radiative feedback using GPCPv3.2 is smaller than those proposed in previous studies where it ranged from 0.1-0.2 (Adames & Kim, 2016; Bretherton et al., 2005; Bretherton & Sobel, 2002; J.-L. Lin & Mapes, 2004b; Peters & Bretherton, 2005).

With zonal filtering, GPCPv3.2 yields weaker feedbacks compared to GPCPv1.3 at all k (**Figure 3.2d**). On MJO spatial scales (k of 1-5), GPCPv1.3 yields feedback magnitudes of 0.17-0.19, and GPCPv3.2 yields 0.12-0.15. The associated wave growth rates are calculated following equation (25b) and associated parameters of Adames and Kim (2016), shown in **Figure 3.2e**. While radiative feedbacks still provide a strong scale selection mechanism since longer wavelengths have higher growth rates than shorter wavelengths, the overall strength of radiative feedbacks are weaker than with GPCPv1.3. This implies that with the updated feedback parameters using GPCPv3.2, moisture mode theory would support only waves with larger zonal extent (wavelengths > 7000 km), while shorter waves are damped. Hence, the updated feedback parameter leads to a weaker theoretical MJO growth rate, but a more obvious scale selection for a planetary zonal scale over shorter zonal scales.

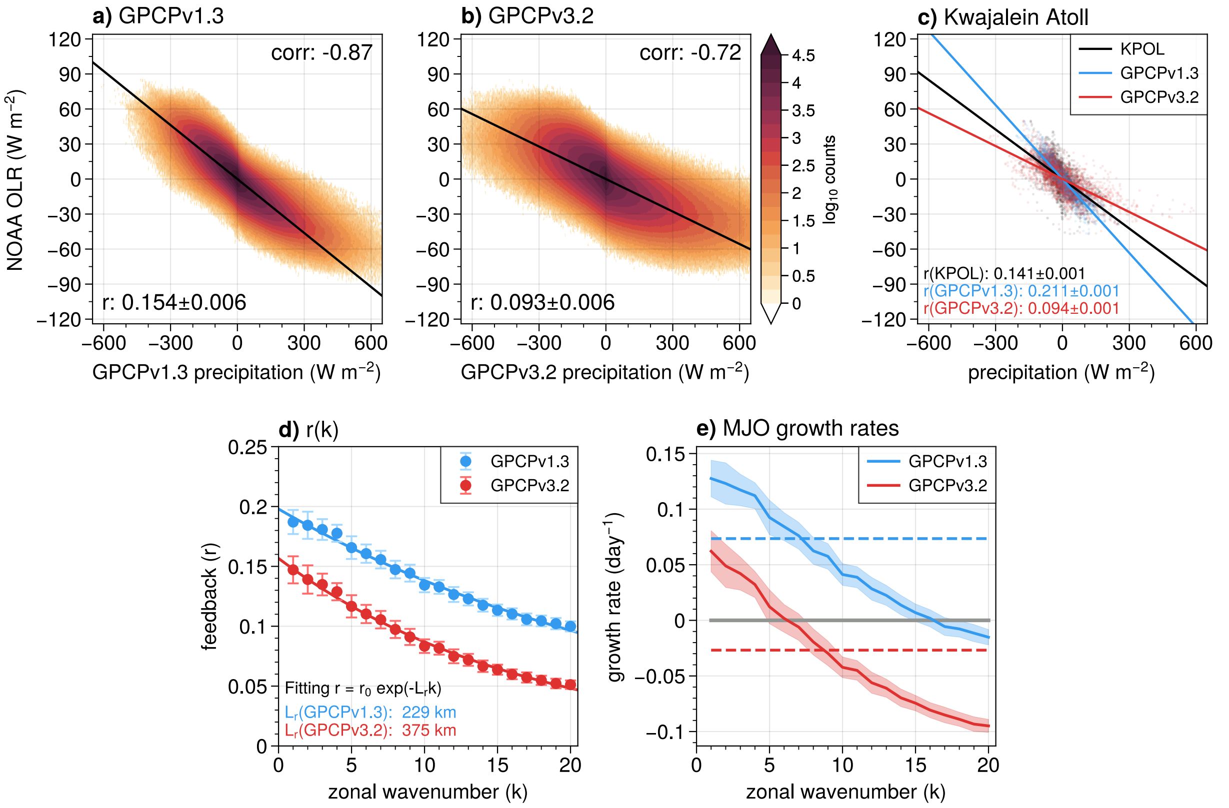

Figure 3.2. Bivariate histograms of 20-100 day filtered OLR and precipitation anomalies over the Indo-Pacific warm pool using (a) GPCPv1.3 and (b) GPCPv3.2. The contours are $\log_{10}$ counts, and the slope of the line shows the linear regression of OLR onto precipitation, with their 95% confidence interval (CI) and correlation coefficients (corr) annotated. (c) as in (a-b) but shows quantities located at the Kwajalein atoll (within 150-km radius from 167.73°E, 8.72°N) in a scatter plot using precipitation from (black) KPOL, (blue) GPCPv1.3, and (red) GPCPv3.2. (d) shows the radiative feedback calculated using single zonal wavenumbers per circumference of the Earth (k) from each version of GPCP, with error bars showing 95% CI and exponential fitting lines overlaid. (e) shows the MJO growth rate calculated as in Adames and Kim (2016) corresponding to (d), with the shading showing uncertainty using the 95% CI of r.

Further error estimation of the feedback is done using precipitation retrieved by ground-based radars. Shown in **Figure 3.2c** (also see **Figures A3.4a-c**), the feedback calculated using KPOL precipitation (0.15) lies in between those obtained by GPCPv1.3 (0.21) and v3.2 (0.09) at the Kwajalein atoll. Similar conclusions are found using S-Pol-Gan filtered by a 30-60-day window (**Figures A3.4d-f**), in agreement with Ciesielski et al. (2017). Previous studies have suggested overestimated oceanic total rainfall using TRMM and IMERG (Bolvin et al., 2021;

Prakash et al., 2013; Prakash & Gairola, 2014), which are products used in producing GPCPv3.2 precipitation. The above literature and evidence suggest that GPCPv3.2 may underestimate the radiative feedback of the MJO, and the actual feedback magnitude may fall between values estimated using GPCPv3.2 and GPCPv1.3.

3.3.3 Precipitation and radiative feedback in other tropical waves

Next, we examine precipitation and the longwave radiative feedback over k-ω spectral space. The precipitation power spectrum of GPCPv3.2 has larger magnitudes than GPCPv1.3 over all of k-ω space, especially over where the power is already large in GPCPv1.3 (**Figures 3.3a-c**). The radiative feedback parameter r (**Figures 3.3d-e**) shows a generally red noise-like distribution that is consistent with previous studies (Inoue et al., 2020; Yasunaga et al., 2019), but also with local peaks at where convectively coupled disturbances are more active, such as in regions of spectral space characterized by Kelvin waves, the n = 1 equatorial Rossby waves (ER), and the MJO (k of 1-5, ω of 0.01-0.05 day^{-1}). Due to the greater spectral power of GPCPv3.2, r yielded by GPCPv3.2 [using **equation (3.1)**] is overall smaller than using GPCPv1.3 (**Figure 3.3f**). Relevant to tropical wave dynamics, the increase in precipitation power from the update of GPCPv3.2 also implies a shorter convective adjustment time. This is true for all waves but especially obvious for westward-propagating tropical-disturbance (TD) -like waves [**Figure A3.4**, calculated following Yasunaga et al., (2019)]. This update implies a faster relaxation of moisture anomalies within the periods of these waves [a larger N_{mode} as indicated in (Adames et al., 2019; Adames & Maloney, 2021)], and thus these waves might be considered more dry gravity wave-like instead of moisture mode-like (Adames et al., 2019; Adames & Maloney, 2021).

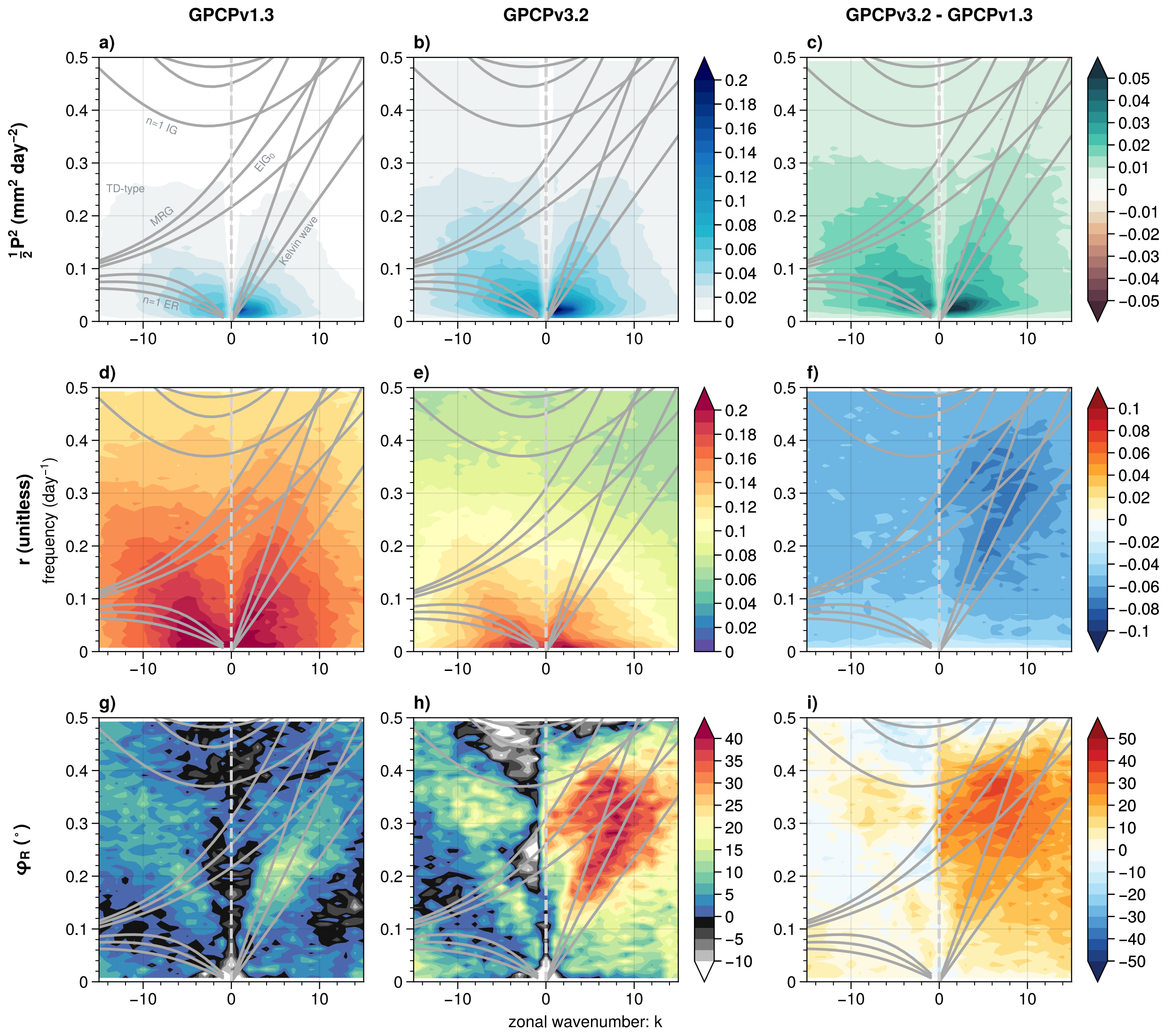

Figure 3.3. (a) the halved power spectrum of precipitation (mm^2 day^{-2}). (d) the radiative feedback parameter *r*. (g) the phase difference between OLR and precipitation (degree). (b,e,h) as (a,d,g) but yielded by GPCPv3.2, while (c,f,i) show their differences (GPCPv3.2 minus GPCPv1.3). The gray solid lines are the solutions for linear convectively coupled equatorial waves at equivalent depths of 12, 25, and 50 m, similar to those shown in Wheeler and Kiladis (1999), with associated wave types annotated in (a).

The phase shift between OLR and precipitation (φ_R) yielded by GPCPv3.2 and GPCPv1.3 shows apparent differences (**Figures 3.3g-i**). Both products generally yield positive or small φ_R, indicating that OLR anomalies lag or are nearly in phase with precipitation. In GPCPv1.3, φ_R has a peak near 20° in Kelvin waves at frequencies near 0.2 day^{-1} (5-day period), and a similar but slightly weaker phase shift for its westward-propagating counterpart. In contrast, a large asymmetry between eastward- and westward-propagating waves is shown in φ_R using GPCPv3.2. There are distinct peaks of φ_R of ~40° in eastward-propagating n = 0 inertia gravity waves (EIG_0) and Kelvin waves, while φ_R are generally smaller than 25° for westward-propagating waves. Large φ_R in Kelvin wave and EIG_0 domains leads to smaller r compared to the conventional method that directly divides OLR by precipitation spectral amplitudes [see **equation (3.1)**]. Why the phase shift only appears in fast eastward-propagating waves but not in westward-propagating waves is possibly related to the less top-heavy and vertically tilted structures in westward-propagating waves (Inoue et al., 2020). Consistent with our results for eastward-propagating waves, prior studies have found vertically-tilted structures in Kelvin waves and other gravity-modulated waves (Inoue et al., 2020; Kiladis et al., 2009; Mapes et al., 2006; Yasunaga & Mapes, 2012), which implies a lag in radiative heating due to the trailing high clouds produced by deep convection. However, large φ_R in Kelvin waves and EIG_0 and small φ_R in the MJO using GPCPv3.2 are different from Najarian and Sakaeda (2023), who suggest a 45° and 0° phase difference in the MJO and Kelvin waves, respectively. As Najarian and Sakaeda (2023) also include shortwave radiation for cloud-radiative forcings, it is possible that shortwave radiation has a non-negligible effect on the phase difference. Lags of radiative heating of around 5 days behind precipitation as shown in Ciesielski et al. (2017) and Del Genio and Chen (2015) suggest an φ_R of ~30° for the MJO (assuming a 60-day period), larger than our calculated φ_R of ~15° in the MJO band (**Figure 3.3h**). These inconsistencies may originate from the precise way variability associated with the MJO and Kelvin waves are defined, the geographical locations of interest, and the sensitivity to not only precipitation, but also OLR datasets. For example, the magnitudes of the φ_R calculated by our method are mildly sensitive to the selection of OLR products (**Figure A3.3**).

If the modified values of φ_R using GPCPv3.2 are more realistic, do they imply different dynamical processes in Kelvin waves than using GPCPv1.3? This is examined in **Figures 3.4e-f** showing relevant atmospheric fields regressed onto Kelvin-wave precipitation (see **Appendix B1** for method). The westward-tilted temperature structure in the troposphere, with cold mid-tropospheric anomalies occurring during peak precipitation, is consistent with previous observations (e.g., Ma & Kuang, 2011; M. Wheeler et al., 2000). The minimum of regressed deep convective inhibition (DCIN; defined as the excess of saturation moist static energy in 700-800 hPa to the moist static energy in 800-1000 hPa) is located more toward peak precipitation when using GPCPv3.2, which better supports theories in which DCIN controls the onset of deep convection associated with Kelvin waves (Ž. Fuchs et al., 2014; Raymond & Fuchs, 2007). Note that the extrema of regressed DCIN and GPCPv3.2 also coincide better with the peak of regressed ERA5 precipitation. A global climate model simulation conducted by Benedict et al. (2020) suggests that anomalous cloud-radiative heating modifies moist static energy profiles in the Kelvin waves, such that it damps the reduction in DCIN at peak Kelvin-wave precipitation . Our result yielded by GPCPv3.2 shows weaker radiative feedback, implying that such damping is weaker. The longitudinal lags between minimum DCIN and OLR are similar between the two GPCP products (5° lon yielded by GPCPv1.3, and 4° lon yielded by GPCPv3.2), so only the strength of the damping would be expected to be altered. However, it is unclear whether the distance between the damping and peak precipitation is important for wave dynamics, and a more detailed analysis is needed in future work. Similar conclusions are shown for EIG_0 in **Figure A3.6**.

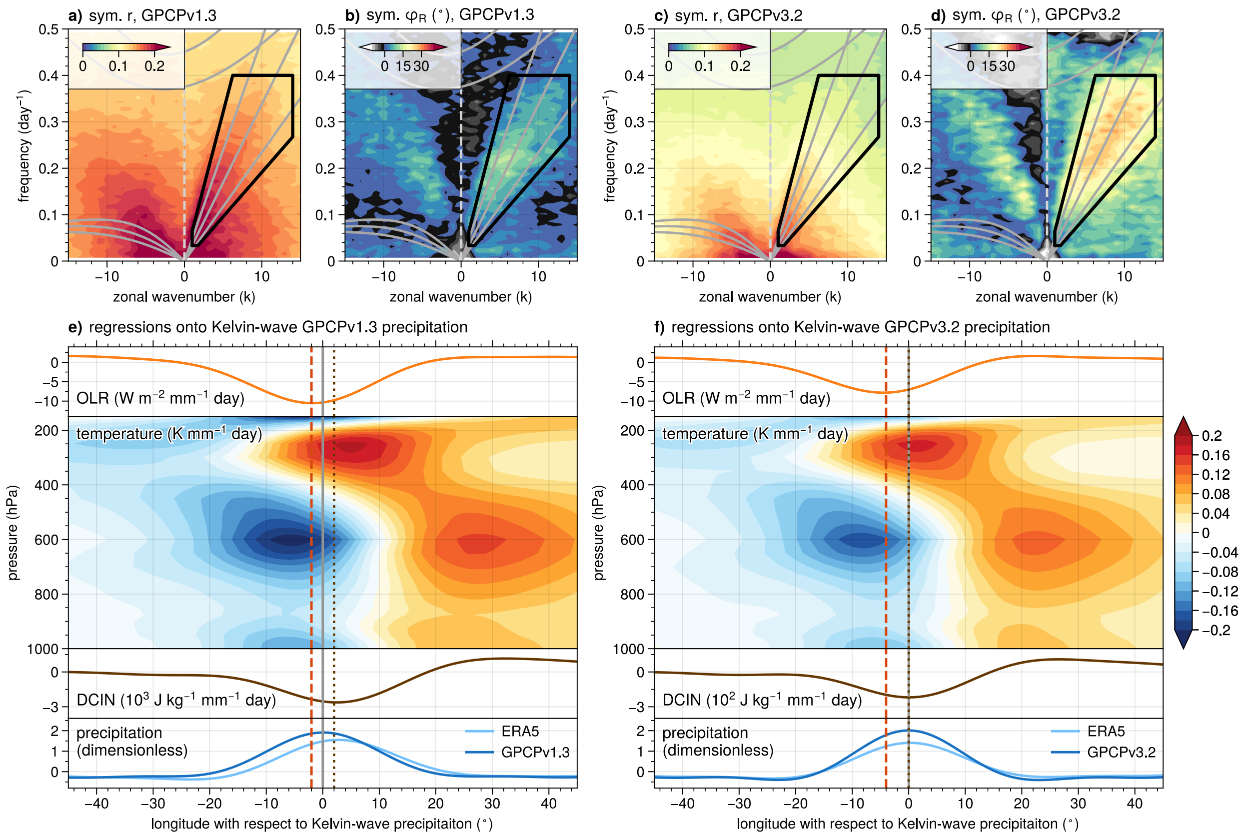

Figure 3.4. As in **Figures 3.3e, h**, but showing the latitudinally symmetric components of r and φ_R using (a-b) GPCPv1.3 and (c-d) GPCPv3.2. Areas enclosed by black lines in (a-d) are selected to isolate Kelvin-wave precipitation. Bottom plots show the regressions of (top row) OLR anomalies, (second row) air temperature anomalies, (third row) DCIN anomalies, and (fourth row) precipitation anomalies onto meridional-mean Kelvin-wave precipitation with lead-lag longitudes using (e) GPCPv1.3 and (f) GPCPv3.2. The longitudes of (dashed black lines) minimum OLR, (dotted black lines) minimum DCIN, and (solid gray lines) the center longitude of regressions is indicated in (e-f).]

3.4 Summary

The longwave cloud-radiative feedback has been hypothesized to be important for the dynamics of tropical atmospheric variability. This study examines the feedback measured by the ratio between negative OLR and surface precipitation anomalies, using two versions of daily GPCP precipitation products versus NOAA OLR. The annual-mean tropical precipitation in the two versions of GPCP are similar, which yields similar annual-mean climatological feedback. For daily-mean values, GPCPv3.2 has more frequent precipitation at higher values above 32 mm day^{-1} than in GPCPv1.3 (**Figure 3.1b**), which is associated with weaker radiative feedbacks for all types of tropical disturbances (**Figure 3.3f**).

The longwave cloud-radiative feedback has been hypothesized to explain the growth and the planetary zonal scale of the MJO under moisture mode theory (e.g., Adames & Kim, 2016; A. Sobel & Maloney, 2012). The radiative feedback associated with the MJO is calculated using 20-100 day-filtered precipitation and OLR over the Indo-Pacific warm pool (**Figure 3.2**). Without considering spatial scales, GPCPv3.2 yields a much weaker feedback (0.09) than using GPCPv1.3 (0.15). The zonal scale-dependence of the feedback is qualitatively similar using either GPCP product, in that the feedback decreases as zonal wavenumber increases, consistent with its role in preferentially supporting larger wavelengths for the MJO. When using GPCPv3.2 instead of GPCPv1.3, moisture mode theory suggests that higher wavenumbers are actually damped due to a weaker feedback, while growth only occurs at low zonal wavenumbers (wavelengths > 7000 km), suggesting a stronger growth at planetary scales for the MJO. Further comparison of the MJO radiative feedback with those yielded by ground-based radar precipitation suggests that while the feedback is overestimated in GPCPv1.3, GPCPv3.2 may underestimate the feedback. In summary, the result suggests that radiative heating provides a stronger scale-selection mechanism for the MJO than previously considered, although how much moistening is supported by radiative heating is still uncertain. This conclusion implies that other supporting feedbacks such as surface latent heat flux and frictional convergence (e.g., Hu & Randall, 1994; Maloney & Sobel, 2004; A. H. Sobel et al., 2008, 2010; A. Sobel & Maloney, 2013; de Szoeke & Maloney, 2020) might be more important than previously thought in destabilizing the MJO and possibly other tropical systems.

In the k-ω spectral space, the radiative feedback parameter r calculated by either precipitation product resembles a red noise-like distribution with spectral peaks at where convectively coupled waves are more active (**Figures 3.3d-f**). Since GPCPv3.2 has larger precipitation power than GPCPv1.3 (**Figures 3.3a-c**), the feedback r is overall smaller (**Figures 3.3d-f**). Interestingly, the phase shift between OLR and precipitation, φ_R, is as large as ~40° in certain fast eastward-propagating waves (Kelvin waves and n = 0 eastward inertia-gravity waves) in GPCPv3.2, with GPCPv1.3 demonstrating a smaller phase shift. The minimum of DCIN coincides better with peak Kelvin-wave precipitation in GPCPv3.2. Similar conclusions are found in EIG_0 (**Figure A3.6**). The updated phase relations using GPCPv3.2 imply a more important role for DCIN in supporting gravity wave-associated deep convection, while the implications for radiative feedbacks are not yet clear and warrant further study.

CHAPTER 4

Three-dimensional Structure of Radiative Effect in the Observed Madden-Julian Oscillation

4.1 Introduction

The Madden-Julian oscillation (MJO; Madden & Julian, 1971, 1972) is a dominant mode of convective activity and precipitation in the tropics, and also generates extreme weather in the extratropics through teleconnections (Kai-Chih Tseng et al., 2019; C. Zhang et al., 2013). Thus, understanding the dynamics of the MJO and being able to accurately simulate it are important for prediction. Different theories have been proposed to explain the general dynamics of the MJO (C. Zhang et al., 2020). In a body of theory commonly referred to as moisture mode theory, radiative feedbacks are proposed to be important for the existence of the MJO. Anomalously high radiative heating in the troposphere associated with higher convective activity, moisture and clouds drives upward motion that moistens the column, supporting further convective heating that aids the maintenance of the moisture mode, a process argued to be relevant to the MJO (Adames & Kim, 2016; Raymond & Fuchs, 2009; A. Sobel & Maloney, 2013; J.-Y. Yu & David Neelin, 1997). Global climate model studies that disable radiative interactions have been shown to weaken the MJO (Benedict et al., 2020; Crueger & Stevens, 2015; Landu & Maloney, 2011), in support of this hypothesis.

However, how radiation affects the dynamics of the MJO is not well understood because prior studies often oversimplify the distribution and effect of radiative processes. For example, in moisture mode theories, radiative heating in the atmosphere is implied to have an identical vertical profile to the apparent heat source (Q_1; Yanai et al., 1973). This is not true in observations, however, as longwave (LW) heating, shortwave (SW) heating, and their sum all have different vertical profiles to Q_1 (Ma & Kuang, 2011). In field observations, the emergence of the active phase of the MJO progresses from shallow convection, to deep isolated convection, and then to deep organized convection with stratiform structure, which are all associated with different radiative heating profiles (Ciesielski et al., 2017; Najarian & Sakaeda, 2023). These radiative heating profiles do not resemble the first and second baroclinic modes of condensational heating and have not been represented in theoretical models. How radiative heating impacts the detailed dynamics of the MJO is of interest, as a better simulation of the MJO would require a well-represented radiative effect (Kim et al., 2015; M.-I. Lee et al., 2001).

In moist static energy (MSE) budget diagnosis, which is commonly used to understand the dynamics of tropical convective systems, radiative heating is treated as a source of heating. However, there are indirect effects generated by radiatively driven circulations, which are proposed to be important in affecting tropical cyclone intensification (Ruppert et al., 2020) and mesoscale convective organization (Ruppert & Hohenegger, 2018), and for enhancing the Walker circulation (Schumacher et al., 2004). In the context of the MSE budget, the total effects of radiative processes are overlooked when only the effects on the temperature tendency are considered, while the effect of radiatively driven circulations is hidden within the vertical and horizontal advection terms in the MSE budget. The radiatively driven circulation near the surface can also modify surface turbulent heat flux, as found to be important also in driving tropical cyclone intensification (Ruppert et al., 2020) and decadal sea surface temperature pattern change in the tropics (Hsiao, Hwang, et al., 2022). These indirect effects of radiatively driven circulation are, however, difficult to diagnose and may require mechanism-denial simulations for their integrated importance to be entirely quantified.

In Chikira (2014), a framework using the weak-temperature-gradient (WTG) approximation is developed to analytically solve for the vertical velocity driven by individual apparent heating terms, which is applicable in the tropics and on MJO spatial and temporal scales (Adames & Maloney, 2021). The framework allows the quantification of the moistening caused by diabatic heating-driven circulations in the MJO. Wolding and Maloney (2016; 2015) use the framework to examine the radiatively-driven moistening in the MJO in a superparameterized atmospheric model (SPCAM; Arnold et al., 2015), and confirm that radiative moistening is necessary to maintain the MJO. Other modeling studies have used similar approaches (Janiga & Zhang, 2016). The robustness of this effect is, however, unknown in the real-world observations, as the vertical structure of radiative heating is needed and is difficult to obtain from observational products. The moistening effect of horizontal circulations driven by radiation has further not been examined in the MJO, either in simulations or observations. Aided by the newly released CERES product that provides the three dimensional (3-D) structure of radiative heating in the atmosphere with daily temporal resolution, we aim to comprehensively study how radiative heating perturbations from this product and associated circulations contribute to the MJO moisture budget.

4.2 MJO composites using OMI

4.2.1 Data

The daily-mean 1° × 1° version of National Oceanic and Atmospheric Administration Interpolated OLR (NOAA OLR; Liebmann & Smith, 1996) is used to diagnose regions of convection and provide an estimate of column-integrated longwave heating anomalies. Atmospheric zonal (u), meridional (v), and vertical (ω) winds, specific humidity (q), and dry static energy (DSE, denoted as s) are obtained from the European Centre for Medium-Range Weather

Forecasts Reanalysis v5 (ERA5; Hersbach et al., 2020), which has a native resolution of hourly and 0.25° × 0.25°. The 0.5° × 0.5°, daily-mean Global Precipitation Climatology Project version 3.2 (GPCPv3.2; Huffman et al., 2023) is used to diagnose surface precipitation. Note that GPCPv3.2 precipitation has larger variance at all wavelengths and frequencies in the tropics than GPCPv1.3 and will lead to larger amplitudes of precipitation in tropical convectively coupled waves than previous studies using GPCPv1.3 and other related products (Hsiao & Maloney, 2024). For surface latent heat (LH) and sensible heat (SH) fluxes, daily-mean 1° × 1° Objectively Analyzed air-sea Fluxes (OAFlux; L. Yu & Weller, 2007) are used.

The Level-3 product Clouds and the Earth's Radiant Energy System Synoptic 1 degree Edition 4.1 (CERES SYN1deg Ed4.1; Doelling et al., 2013, 2016; Loeb et al., 2018) provide radiative heating rates on pressure levels. The product is calculated by a radiative transfer model with satellite-retrieved cloud properties and top-of-atmosphere (TOA) radiative fluxes, and a real-time analysis of atmospheric conditions. Clear-sky radiative fluxes are generated by removing the clouds in the radiative transfer calculation, and the cloud radiative effect (CRE) is calculated in the present manuscript by subtracting the clear-sky fluxes from the all-sky fluxes. The resolution of CERES SYN1deg is 1° × 1°, and daily means are used. The radiative fluxes are provided at six vertical levels (TOA, 70 hPa, 200 hPa, 500 hPa, 850 hPa, and the surface) which are then used to calculate atmospheric radiative heating rates at five vertical levels centered at 35 hPa, 135 hPa, 450 hPa, 675 hPa, and 925 hPa. The vertical structure of the MJO radiative heating derived from CERES SYN1deg is generally consistent with previous studies using CloudSat (Ma & Kuang, 2011) and ground-based radar retrievals (Ciesielski et al., 2017; Najarian & Sakaeda, 2023; Shell et al., 2020).

The data products described above are averaged horizontally to a 1° × 1° grid and daily means are constructed. The CERES SYN1deg atmospheric radiative heating is linearly interpolated to the finer pressure coordinate of ERA5 with 25 levels over 1000-150 hPa. At locations where the surface elevation is higher than 200 m, the radiative heating rates below 675 hPa are set to zero to avoid unphysical values. Multiple criteria of surface elevation for this additional step are tested and do not affect the general features of diagnosed MJO radiation fields. Climatological anomalies of all data products are obtained by removing their linear trends and the first three harmonics of the annual cycle calculated using data during 01 September 2002 - 31 August 2021. A total of 19 years of anomalies during 01 July 2003 - 30 June 2021 are analyzed for all datasets.

4.2.2 Compositing method

A composite for the MJO lifecycle is constructed as the following. The all-season OLR MJO index (OMI; Kiladis et al., 2014) is normalized to have a zero mean and a unity standard deviation during 01 September 2002 - 31 August 2021. The MJO is then divided into 64 phases by linearly combining the two normalized orthogonal OMIs. Unfiltered precipitation anomalies from GPCPv3.2 are then linearly regressed onto each linear combination of OMIs representing each MJO phase, similar to the method used in Adames and Wallace (2014), but only for the extended boreal winter (November - April). Precipitation regressions of four example phases are demonstrated in **Figures 4.1a-d**, showing the MJO precipitation anomaly (P') progressing eastward through the Indo-Pacific warm pool. Note that the superscript prime (') in this study is used to denote MJO-associated anomalies, which are defined specifically by the regression procedure described above.

Next, the longitudes of the MJO precipitation centers are identified using the 64 regression maps at each MJO phase. The meridional means of P' between 20°S and 10°N at each phase is calculated, as shown in **Figure 4.1e**. A running-zonal smoothing using a Gaussian weighting with a standard deviation of 5° longitude is then applied, and the maximum precipitation point is labeled as the MJO precipitation center at each phase. A negative precipitation center can be similarly defined by finding the minimum point, which by definition is 180° out of phase with the positive precipitation center. The positive and negative precipitation centers are marked as green and yellow curves in **Figure 4.1e**, respectively.

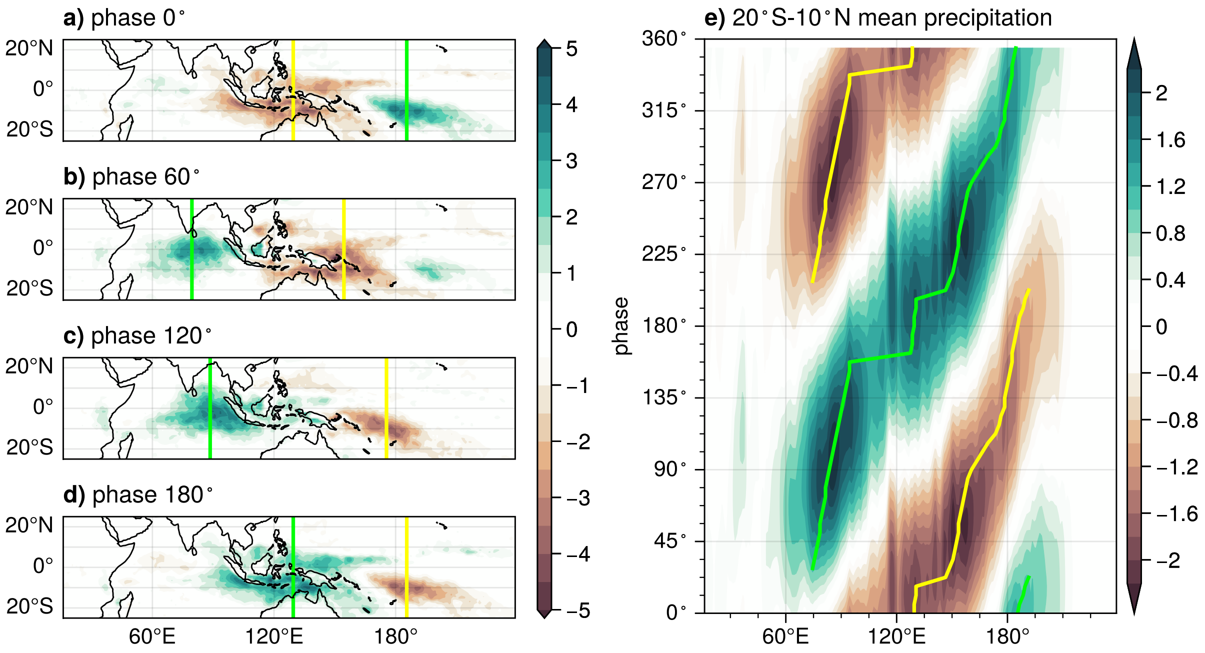

Figure 4.1. Regressed MJO precipitation (P') at certain OMI phases: (a-d) example at four phases as labeled, and (e) the meridional means in 20°S-10°N, with the identified MJO precipitation center. The identified MJO precipitation center longitudes (green lines) and their counterpart for precipitation minima (yellow lines) are also shown.

Finally, MJO composites for variables of interest centered on the precipitation maximum can be calculated by taking the average of the regression map at all 64 MJO phases, with the precipitation center defined as a reference longitude of 0°.

4.2.3 Basic fields

Basic composite MJO fields are first overviewed and compared to previous studies. **Figure 4.2a** shows the MJO-composite P’ (shading) and OLR’ (contours). An approximately circular region of positive precipitation anomalies is shown, maximized at the reference longitude (0°). The composite P’ and OLR’ have only hints of a “swallow-tail” structure on their western flank commonly found when identifying the MJO using dynamical fields (Adames & Kim, 2016; Maloney & Hartmann, 1998; Chidong Zhang & Ling, 2012), exhibited by the two local extrema at 10°S and 10°N near -30° longitude, possibly because of the use of the OMI index that is based on MJO-associated convective features but has less consistent large-scale circulation features (Kiladis et al., 2014). A southeastward extension of the OLR’ and P’ is shown, which is likely a manifestation of the southward detour of the MJO near the Maritime Continent toward the South Pacific Convergence Zone (SPCZ; as in **Figure 4.1d**).

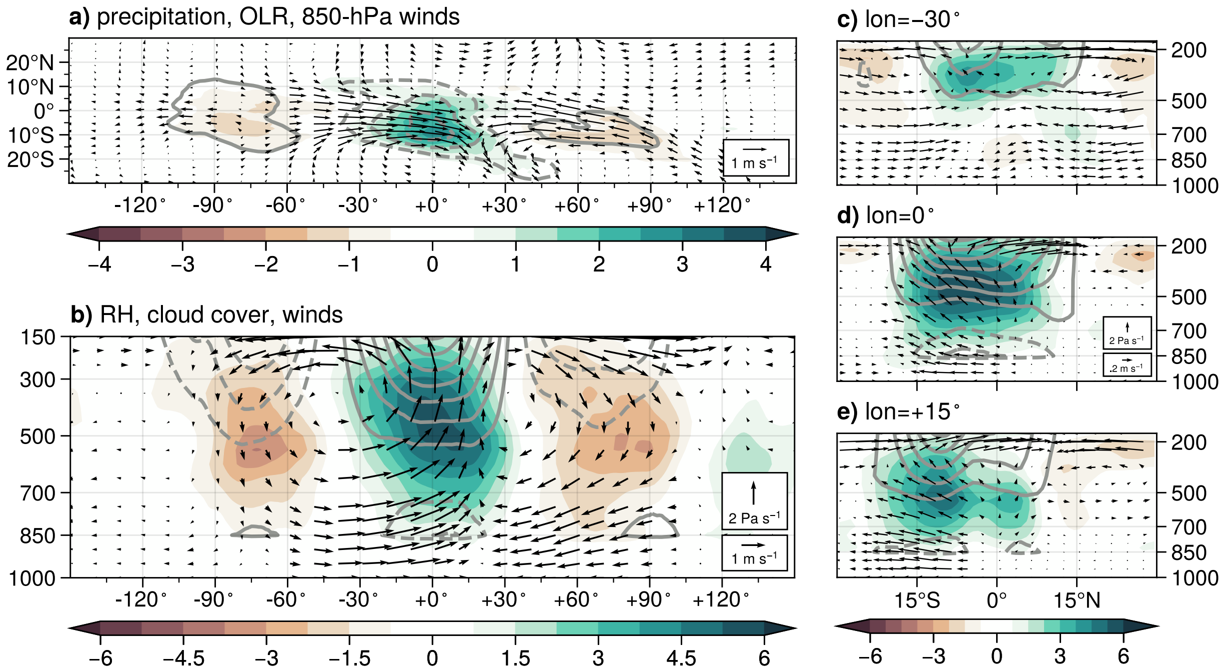

Figure 4.2. MJO-composite (a) P' (shading; mm day^{-1}), OLR' (contours; zero omitted; 4 W m^{-2} spacing), and 850-hPa horizontal winds (arrows; scale annotated) on latitude-longitude plane, (b) RH' (shading; %), cloud cover anomaly (contours; 0.5 % spacing), and velocity anomaly (arrows; scale annotated) on a pressure-longitude cross section at 10°S, and (c-e) as in (b) but showing pressure-latitude cross sections at -30°, 0°, and 15° longitudes.

A vertical cross section in **Figure 4.2b** demonstrates a westward tilted anomalous structure in relative humidity (RH; shading), with the maximum anomaly occurring at 400 hPa. Positive anomalies of cloud cover (contours) maximize near the top of the troposphere at the reference longitude. In the velocity field, low-level convergence occurs ahead of the reference longitude by 20°, with upper-level divergence occurring 10° ahead of the reference longitude, consistent with previous results (e.g., Maloney & Hartmann, 1998), indicating a westward-tilted circulation structure. Three longitudinal slices at -30°, 0°, and +15° are examined in **Figures 4.2c-e**. At 0° longitude (**Figure 4.2d**), the maximum in RH and high cloud cover anomalies are centered to the south of the equator. Behind the maximum P' at -30° longitude, the RH' and high cloud cover anomaly are also centered to the south of the equator, while there is a negative RH' in the lower troposphere at the equator, possibly induced by both the mean and eddy transport of moisture by meridional winds (Adames & Wallace, 2015; Andersen & Kuang, 2012; Maloney, 2009). Ahead of the maximum MJO at +15° longitude, two local maxima in RH and high cloud cover anomalies occur, one to the north near the location of the Northern Hemisphere ITCZ at 5°N, and one to the south near the location of the SPCZ at 10°S. At the northern anomalous RH maxima, the shallower positive RH anomaly and weaker cloud cover anomalies near the top of troposphere compared to the southern maximum suggests that congestus clouds are anomalously prominent in the north but deep convective clouds and high clouds are more dominant in the south. To summarize, the composite method used in this study replicates many features of the MJO observed in previous studies, and thus provides confidence it can be used for the following examination of radiative moistening.

4.3 Diagnosis of moistening induced by radiative effects

As elaborated in the **Chapter 4.1**, radiative heating not only heats the atmosphere, but it also induces circulations that transport moisture, which can be partly diagnosed under the WTG approximation. This subchapter describes a framework of quantifying the moisture advection associated with radiatively-induced circulation anomalies. Vertical advection can be diagnosed directly using the WTG approximation, and horizontal advection can be derived using results from numerical model integrations forced by observed radiative heating.

4.3.1 Vertical-advective moistening

Moistening generated by the vertical advection caused by radiatively-induced vertical velocity anomalies can be analytically derived using a WTG framework that is valid in the tropics on MJO spatial and temporal scales (Chikira, 2014; A. Sobel & Maloney, 2013; B. O. Wolding et al., 2016; B. O. Wolding & Maloney, 2015). WTG balance states that in the free troposphere,

$$\omega \approx Q_1(\partial s/\partial p)^{-1} \tag{4.1}$$

where ω is vertical pressure velocity, s is DSE, and Q_1 is the apparent heat source (Yanai et al., 1973). In other words, WTG balance implies that vertical velocity in the tropical atmosphere can be diagnosed if diabatic heating is known, an approximation found to hold above the 900-hPa level (not shown). We can further decompose Q_1 into the radiative heating term Q_R and the residual convective heating term Q_C, where the subscript C denotes "convective processes" including microphysical heating and turbulent DSE fluxes:

$$Q_1 = Q_R + Q_C \tag{4.2}$$

Thus, the vertical velocity can be decomposed into those induced by Q_R and Q_C. For the purpose of identifying the effect of radiation perturbations, the radiatively-driven vertical velocity (ω_R) derived under the WTG is only calculated above the 900-hPa level using CERES Q_R and ERA5 dry static stability, while set to zero below. The non-radiatively driven vertical velocity (ω_C) is then derived as the residual of ERA5 ω minus ω_R, as written in the following:

$$\omega_R = \begin{cases} Q_R(\partial s/\partial p)^{-1}, & p \leq 900\ hPa \\ 0, & p > 900\ hPa \end{cases} \tag{4.3a}$$

$$\omega_C = \omega - \omega_R \tag{4.3b}$$

Note that since ω_R is only derived above 900 hPa, ω_C below 900 hPa partly contains the vertical velocity coupled with radiative heating perturbations and boundary layer frictional convergence that are not analytically derivable under the WTG framework. Further decomposition can be made by decomposing ω_R into those induced by either the radiative heating rates of longwave ($Q_{R,LW}$) and shortwave ($Q_{R,SW}$) radiation and their clear-sky ($Q_{R,LW,cloud}$ and $Q_{R,LW,clear}$)

and cloud-radiative-effect (CRE) components ($Q_{R,SW,cloud}$ and $Q_{R,SW,clear}$), with the latter defined as the all-sky minus clear-sky radiative heating. The radiatively driven vertical velocity can then be used to derive the vertical moisture advection caused by these terms, a component of the "column process" (denoted by the subscript *col*) in Chikira (2014):

$$(\partial L_v q/\partial t)_{X,col} = \omega_X (\partial s/\partial p)^{-1} \tag{4.4}$$

where *X* can be substituted with the subscript notation of individual apparent heating components described in the text above, denoting the contribution by individual heating components (Q_X) and their induced vertical velocity (ω_X). The vertical moisture advection induced by the apparent heating terms can then be expressed as,

$$(\partial L_v q/\partial t)_{X,col} = \left(-\frac{\partial L_v q/\partial p}{\partial s/\partial p}\right) Q_X = \alpha Q_X \tag{4.5}$$

where L_v is the specific condensation heat of water, and α is the Chikira parameter (Chikira, 2014). α, the negative ratio of the vertical moisture gradient and the dry static stability, can be interpreted as a *moistening efficiency* indicating how much vertical advective moistening is induced per unit apparent heating. The above formulation allows an attribution of vertical velocity to individual radiative heating terms, and further attribution of vertical advective moistening induced by individual radiative heating terms. As conventional MSE budget separates the vertical advection of MSE ($-\omega \partial h/\partial p$) and apparent heating ($Q_X$), the vertical advection of DSE induced by Q_X ($-\omega \partial s/\partial p$) in fact cancels out Q_X under WTG, yielding the total effect of MSE budget by Q_X as αQ_X as shown in the following:

$$\omega_X \frac{\partial h}{\partial p} = \omega_X \frac{\partial L_v q}{\partial p} + \omega_X \frac{\partial s}{\partial p} \tag{4.6a}$$

$$\omega_X \frac{\partial h}{\partial p} + Q_X = \omega_X \frac{\partial L_v q}{\partial p} + \left(\omega_X \frac{\partial s}{\partial p} + Q_X\right) = \omega_X \frac{\partial L_v q}{\partial p} = \alpha Q_X \tag{4.6b}$$

Here, the WTG assumption is used in **equation (4.6b)** so that $\omega_X \partial s/\partial p + Q_X = 0$, The above derivation demonstrates that while the conventional MSE budget is mathematically valid, it is somewhat misleading in terms of being able to attribute a budget tendency to a particular apparent heating. Examining αQ_X helps identify the integrated effects on both MSE and moisture budgets of column processes by considering the coupled nature of vertical motion and apparent heating in a system under WTG balance.

The variability in α is horizontally small but vertically large, such that it has higher values in the lower troposphere (**Figure 4.3e**). This vertical distribution feature leads to stronger moistening if a diabatic heating profile is more bottom-heavy. This columnar efficiency of WTG moistening in the MJO is further measured by an effective moistening efficiency $\hat{\alpha}$, which can be defined for each diabatic heating terms as:

$$\hat{\alpha}_X = \frac{\langle \alpha Q_X \rangle'_{FT}}{\langle Q_X \rangle'_{FT}} \tag{4.7}$$

where $(')$ denotes the MJO anomaly associated with one standard deviation of OMI, derived by regression onto OMI (**Chapter 4.2.2**). The brackets denote mass-weighted vertical integration $\langle \cdot \rangle_{FT} = \int_{FT} \cdot\, dp$, where FT denotes free troposphere (900-150 hPa). Note that $\hat{\alpha}_X$ is equivalent to the average α weighted by the vertical structure of the MJO-associated apparent heating anomaly Q'_X. The column-integrated moisture and MSE budget over FT contributed by apparent heat Q'_X, following **equations 4.6** and **4.7**, can thus be written as:

$$\langle \omega_X \frac{\partial h}{\partial p} \rangle'_{FT} = \langle Q'_X \rangle_{FT} = \langle \omega_X \frac{\partial L_v q}{\partial p} \rangle'_{FT} = \hat{\alpha}_X \langle Q'_X \rangle_{FT} \tag{4.8}$$

4.3.2 Horizontal winds

Radiative heating induces vertical motion under the WTG balance, which implies that a vertically non-uniform radiative heating induces horizontal divergence under the anelastic approximation. While the horizontal divergence can be analytically solved using the solved vertical velocity in **Chapter 4.3.1**, the two-dimensional horizontal winds cannot be analytically diagnosed. A linear baroclinic model proposed by Watanabe and Kimoto (2000) is thus used to infer the horizontal winds coupled with radiative heating using the following procedures.

The model is integrated on a horizontal grid of T42 having approximately 2.8° resolution, and with 20 vertical layers. The regressed MJO radiative heating and ERA5 climatologies are regridded onto the model grid. The model is equipped with the background state of the regridded mean climatological field over the extended-boreal winter obtained by ERA5. The regridded MJO-regressed radiative heating terms at each of the 64 phases are imposed in the model for ten days, when the wind fields generated by each radiative heating term are saved. While the choice of the tenth day is somewhat arbitrary, using any day between the fifth day and the fifteenth day yields similar results. An MJO composite is then derived for these 64 phases for each radiative heating term to obtain their induced composite MJO circulation. These circulations are compared to the observed MJO circulations to infer possible effects on MJO dynamics.

Although the horizontal flow induced by radiation is able to transport heat and moisture, we cannot quantitatively derive its role in the MJO moisture budget directly, as the simulation setting does not allow us to resolve the eddy transport associated with timescales shorter than the MJO. For example, variations in activity associated with tropical synoptic disturbances have important first-order impacts on the MJO moisture budget (Maloney, 2009). We attempt to derive these terms diagnostically using the mean fields and the MJO-associated anomalies (**Chapter**

4.5.3). Another caveat of the validity of the simulation is that while the MJO-associated heating propagates eastward, the heating is imposed steadily in the simulations, but they should yield circulation patterns that are at least qualitatively representative of the MJO as shown in previous studies (e.g., Kai-Chih Tseng et al., 2019). The correlation coefficient calculated by predicting MJO-composite 850-hPa winds in the tropics (30°S-30°N) in ERA5 using winds driven by Q_1' in the linear baroclinic model is 0.82 for the u' (zonal wind) and 0.71 for v' (meridional wind), suggesting that the model well simulates the MJO-associated winds by imposing apparent heating.

4.4 Radiative moistening in the MJO composite

4.4.1 Vertical-advective moistening at the center of the MJO

As discussed in **Chapter 4.3.1**, the vertical profile of the moistening efficiency α (**Figure 4.3e**) implies that more bottom-heavy radiative heating is more efficient in moistening the atmosphere by vertical advection. Here, we examine the vertical profiles of atmospheric radiative heating and moistening rates averaged near the MJO precipitation maximum (20°S-10°N, -10°-10° relative longitudes) from the MJO composites (**Figure 4.3**), with the column integrated values over 900-150 hPa shown in **Table 4.1**. Note that the moistening rates in **Table 4.1** are given in units of K day^{-1} through multiplication by L_v and normalization by the specific heat capacity of air (c_p), yielding unitless values of $\hat{\alpha}$ (**equation 4.6**). Precipitation is also given in units of K day^{-1} through multiplication by L_v, yielding unitless contributions of individual moistening rates to precipitation.

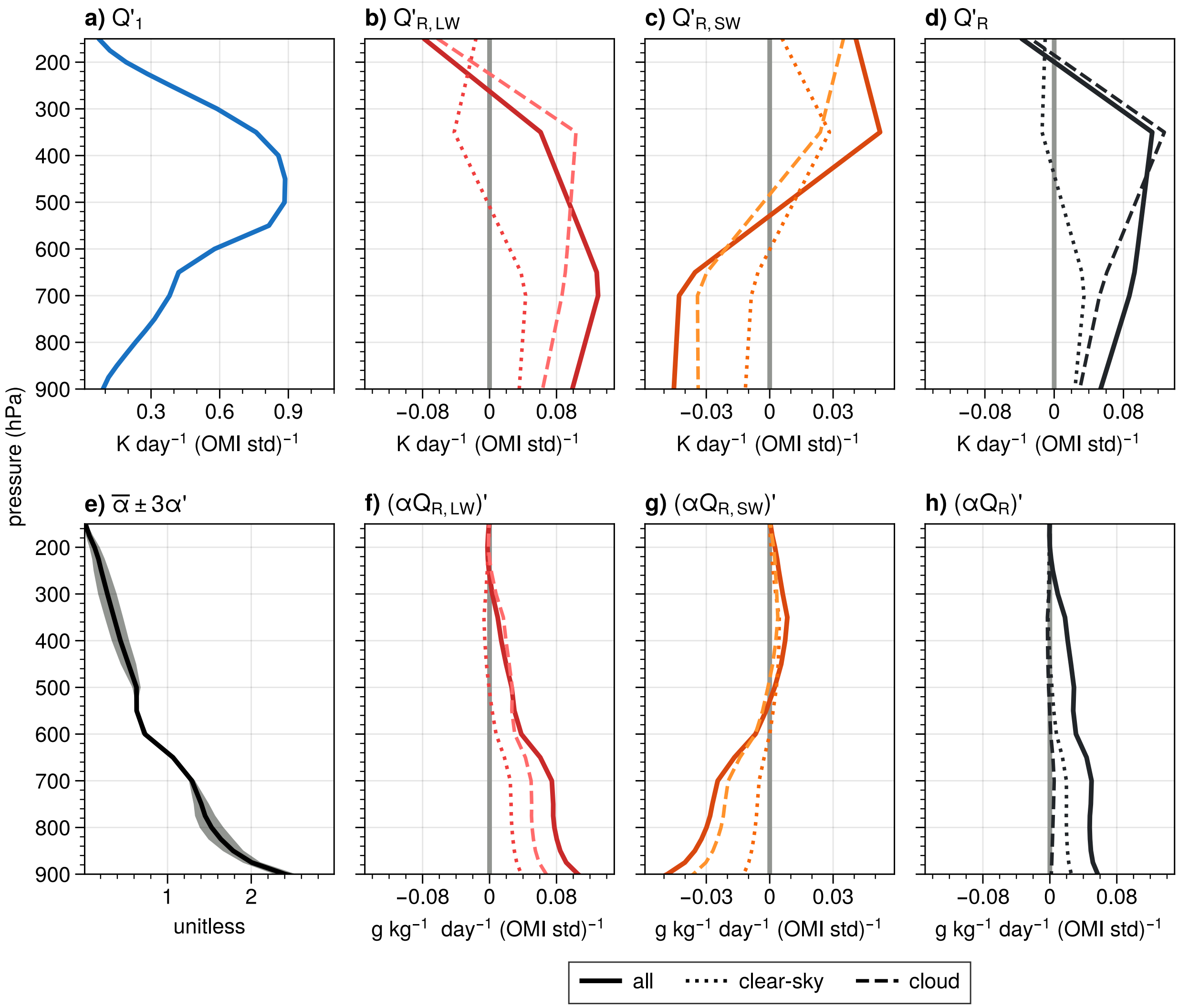

Figure 4.3. Vertical structures of MJO anomalies related to radiatively driven moistening near the composite MJO center, averaged over 20°S-10°N, ±10° relative longitudes: (a) apparent heat source Q_1', (b) LW radiative heating $Q_{R,LW}'$, (c) SW radiative heating $Q_{R,SW}'$, (d) total radiative heating Q_R', (e) the climatological Chikira parameter α with its tripled inter-MJO phase range, (f) LW radiative moistening anomalies $\left(\alpha Q_{R,LW}\right)'$, (g) SW radiative moistening anomalies $\left(\alpha Q_{R,SW}\right)'$, and (h) total radiative moistening anomalies $(\alpha Q_R)'$. For radiative terms, dotted lines indicate the clear-sky effect, dashed lines indicate the CRE, and thick solid lines indicate the total effect.

Table 4.1. Quantities related to radiative moistening calculated by column integrations of variables shown in **Figure 4.3**.

	900-150 hPa heating (K day^{-1})	900-150 hPa moistening (K day^{-1})	900-150 hPa $\hat{\alpha}_X$	moistening contribution to P’
$\boldsymbol{Q'_{R,LW}}$	**0.073**	**0.084**	**1.160**	**0.235**
$Q'_{R,LW,cloud}$	0.068	0.066	0.965	0.183
$Q'_{R,LW,clear}$	0.005	0.019	4.062	0.052
$\boldsymbol{Q'_{R,SW}}$	**0.001**	**-0.017**	**-12.91**	**-0.046**
$Q'_{R,SW,cloud}$	-0.004	-0.014	3.155	-0.039
$Q'_{R,SW,clear}$	0.006	-0.003	-0.492	-0.008
$\boldsymbol{Q'_R}$	**0.074**	**0.068**	**0.915**	**0.188**
$\boldsymbol{Q'_1}$ [#]	***0.487***	***0.396***	***0.813***	***1.105***

The column-integrated $Q'_{R,LW}$ is positive (0.070 K day^{-1}), mainly due to its CRE (0.065 K day^{-1}). $Q'_{R,LW}$ is mostly positive with a bottom-heavy heating structure that maximizes at 700 hPa, except near the top of the troposphere where a cloud-top cooling occurs above 300 hPa (**Figure 4.3b**). Decomposing the radiative heating into clear-sky and cloud-effect components, the overall magnitude of $Q'_{R,LW}$ is dominated by $Q'_{R,LW,cloud}$, although the bottom-heavy structure of $Q'_{R,LW}$ is largely shaped by the clear-sky component. Despite the fact that column-integrated $Q'_{R,LW,clear}$ is small (0.005 K day^{-1}), it has a vertically dipolar profile with a heating in lower troposphere and a cooling in upper troposphere that cancels out in the vertical integral, although it has an effect on

---

[#] **Table 4.1** shows the WTG moistening caused by Q'_1 for the purpose of comparing the moistening efficiency with different vertical heating profiles. As Q'_1 mainly consists of the latent heat release of vapor condensation (Q'_a), or $Q'_a \sim Q'_1$, the large WTG moistening generated by Q'_1 does not imply that the condensation process moistens the atmosphere. The generation of condensational heating sacrifices moisture and so the total moistening rate considering this process is $([\alpha - 1]Q_d)'$, which is commonly negative as suggested in Chikira (2014) as a process of convection removing water vapor from the atmosphere.

lowering the level of maximum LW heating. Since the maximum RH’ is located at 450 hPa and that $Q'_{R,LW,clear}$ is determined by the vertical gradient of RH’ (**Figure 4.5b**) (Fildier et al., 2023), a dipolar structure of $Q'_{R,LW,clear}$ exists. $Q'_{R,LW,cloud}$ has a top-heavy heating structure that maximizes at 350 hPa, as $Q'_{R,LW,cloud}$ tends to be largely positive near the bottom of high clouds (**Figure 4.4b**) (Webster & Stephens, 1980).

The bottom-heavy $Q'_{R,LW}$ yields a large moistening rate by LW radiation $\left(\alpha Q_{R,LW}\right)'$ at lower levels (**Figure 4.3f**) with a column-integrated value of 0.084 K day^{-1}. To examine how efficient the associated vertical profile is moistening the atmosphere under the WTG framework, the column effective moistening efficiency of LW $\hat{\alpha}_{R,LW}$ defined as the ratio between the column-integrated $\left(\alpha Q_{R,LW}\right)'$ and $Q'_{R,LW}$ is examined (see **Chapter 4.3.1**) and compared to the total apparent moistening efficiency $\hat{\alpha}_1$. While Q'_1 being top-heavy maximizes at 450 hPa, which yields $\hat{\alpha}_1 = 0.813$, $\hat{\alpha}_{R,LW} = 1.160$, which is larger. As idealized moisture mode theories commonly assume a constant vertical mode of diabatic heating (Adames & Kim, 2016; e.g., Ž. Fuchs & Raymond, 2002; A. Sobel & Maloney, 2013), $\hat{\alpha}_{R,LW} > \hat{\alpha}_1$ implies that the role of longwave destabilizing the atmosphere (by reducing the effective gross moist stability in some formulations) is underestimated in the previous studies by about 43%. The high efficiency of moistening is contributed by LW CRE with $\hat{\alpha}_{R,LW,cloud} = 0.965$ and clear-sky LW with $\hat{\alpha}_{R,LW,clear} = 4.062$, both having $\hat{\alpha}$ larger than $\hat{\alpha}_1$. The fact that $\hat{\alpha}_{R,LW} > 1$ also implies that the LW radiative effect to column MSE budget under WTG balance is larger than that considering the direct heating by LW radiation alone.

The column-integrated SW radiative heating anomaly ($Q'_{R,SW}$) is nearly zero (0.001 K day^{-1}). This is a result of both $Q'_{R,SW,clear}$ and $Q'_{R,SW,cloud}$ having a vertically dipolar structure with a cooling at the lower troposphere and a heating at the upper troposphere that approximately cancel

(**Figure 4.3c**). Anomalously positive high-cloud cover (**Figure 4.6b**) increases the multiple scattering and absorption of SW radiation at the upper troposphere, and leaves less SW radiative flux entering the lower troposphere, leading to the dipolar structure of $Q'_{R,SW,cloud}$. Anomalously positive RH maximizes at 450 hPa (**Figure 4.7b**) increases the absorption of SW radiation at the upper troposphere, and leaves less SW radiation entering the lower troposphere, leading to the dipolar structure of $Q'_{R,SW,clear}$.

The effect of SW radiation on the MJO is commonly overlooked due to its near-zero column-integrated heating when examining the MSE budget, without considering the circulation induced under the WTG framework. In fact, the dipolar structure of $Q'_{R,SW}$ leads to a non-zero and negative column-integrated moistening (-0.017 K day^{-1}). The cooling in the lower troposphere induces downward motion that transports dry air downward, while the heating in the upper troposphere induces upward motion that transports little moisture upward given the low specific humidities at those levels (**Figure 4.3g**). The role of SW thus damps moistening near the center of the MJO by ~20% of the magnitude of LW moistening in a column-integrated sense. Note that because of the near-zero column-integrated $Q'_{R,SW}$, the magnitude of $\hat{\alpha}_{R,SW}$ is very large because of a small denominator, and hence its exact value is highly sensitive to the method of calculation.

Since $Q'_{R,LW}$, which moistens the MJO, is an order of magnitude larger than $Q'_{R,SW}$, the column-integrated total radiative effect is positive (0.074 K day^{-1}), while $\hat{\alpha}_R < \hat{\alpha}_{R,LW}$ due to the damping of moistening by SW radiation. The total radiative moistening efficiency $\hat{\alpha}_R$ is still larger than $\hat{\alpha}_1$ by 13%, suggesting an underestimation of radiative moistening in WTG moisture mode theories that assume similar vertical structure of radiation and Q_1 anomalies. The contribution of total radiative moistening to surface precipitation is 0.188 as shown in **Table 4.1**, which is higher than the values of longwave cloud-radiative feedback previously estimated for convective systems (or sometimes referred to as the cloud enhancement factor) as the reduction of OLR per unit surface precipitation (0.10-0.15; J.-L. Lin & Mapes, 2004b). As the newly released GPCPv3.2 contains larger variability in precipitation and reduces the estimation of the radiative feedback to less than 0.1 (Hsiao & Maloney, 2024), our result considering the vertical advective moistening induced by radiation leads to a high integrated magnitude of the radiative feedback.

Note that the moistening rates $(\alpha Q_R)'$ and moistening efficiencies $\hat{\alpha}$ discussed in this subchapter could be quantitatively sensitive to the detailed vertical structure of the radiative heating, while the qualitative conclusions that SW radiation dries and LW radiation moistens the atmosphere efficiently still hold. Previous studies examining radiative heating anomalies in MJO active regions demonstrate that $Q'_{R,SW}$ has a similar dipolar structure a sign transition at around 500 hPa or 5 km (Ciesielski et al., 2017; Ma & Kuang, 2011; Najarian & Sakaeda, 2023; Shell et al., 2020). LW radiation structure is less consistent among studies although they all have a generally more bottom-heavy $Q'_{R,LW}$ compared to Q_1, that either monotonically decreases with height (Shell et al., 2020) or has multiple local maxima below 400 hPa (Ciesielski et al., 2017; Ma & Kuang, 2011; Najarian & Sakaeda, 2023). A dependence on the composite method of the MJO is also demonstrated by the inconsistency in vertical structure between studies using the same radiative heating product but different compositing technique (Ciesielski et al., 2017; Najarian & Sakaeda, 2023; Shell et al., 2020).

4.4.2 The three-dimensional spatial structure of MJO radiation

In this subchapter, we expand the scope to examine the 3-D structure of heating, moistening, and the circulation induced by radiative processes as shown in **Figures 4.4-4.8**. Besides the radiative heating [shading in panels (b-c)] and WTG moistening rates [shading in panel (a), red and blue thin contours in panel (b-c)] as discussed in the previous subsection, 3-D wind fields induced by radiation anomalies derived using a linear baroclinic model are also examined (arrows; see **Chapter 4.3.2** for simulation setups). The drivers of the spatial structures of the cloud radiative effects and clear-sky radiative effects, namely the cloud cover (thick gray contour lines in **Figures 4.4, 4.6**) and RH (thick gray contour lines in **Figures 4.5, 4.7**) anomalies, respectively, are also examined. Note that $(\alpha Q_{R,X})'$ has sporadic unphysically large values for moistening rates at lower levels, and so they are plotted after removing points with sharp changes on the horizontal directions in **Figures 4.4-4.8** for clarity (in particular, by removing points with horizontal gradients larger than one standard deviation over each level in 700-900 hPa).

4.4.2.1 LW radiative effect

The 3-D structure of MJO LW CRE anomalies and their effects on circulations and moistening are examined in **Figure 4.4**. **Figure 4.4a** shows that the column-integrated moistening coincides with high cloud cover anomaly, maximizing at a magnitude of 1 W m^{-2}. Both high cloud cover, the moistening, and cyclonic flow on the west side of the MJO center presents a shallow-tail structure, with two maxima at 10°N and 10°S latitude symmetric with respect to the equator, consistent with the Rossby wave response to a Gill-type heating (Gill, 1980). Positive high cloud cover and moistening is also high on the southeast side, which is a result of including central Pacific locations in the MJO composite, where it detours southward and propagates faster. In **Figure 4.4b**, MJO LW CRE is top-heavy and maximizes below the maximum positive high cloud cover anomaly. The heating anomaly is up-right instead of tilted vertically, while it shows some asymmetry in the zonal direction such that the heating extends to the west to -40° further than that to the east to +30°, consistent with more stratiform convective systems after the MJO precipitation maximum (Ciesielski et al., 2017; X. Lin & Johnson, 1996). The radiative heating at the MJO center and the radiative cooling behind and in front of the center drives an enhanced overturning circulation. While the high cloud cover anomaly and LW cloud-radiative heating anomaly maximizes at 10°S at 0° relative longitude with a large meridional extent (**Figure 4.4d**), behind the MJO at -30° relative longitude a narrow maximum occurs at 5°S with a secondary peak at 10°N (**Figure 4.4c**), leading to an enhanced meridionally converging flow below 700 hPa. The enhanced meridionally flow transports drier air equatorward and partially cancels the effect of radiation inhibiting the eastward propagation of the MJO, which will be discussed in **Chapter 4.5.2**. A secondary peak at 10°N in mid-high cloud cover within 300 to 500 hPa appears in front of the MJO at +15° relative longitude, causing a local maximum heating at 700 hPa.

Figure 4.5 shows the 3-D structure of MJO clear-sky LW radiative anomalies. The clear-sky LW radiation weakly enhances the column integrated moistening at the MJO center by 0.02 K day^{-1} (**Figure 4.5a**). Following the vertical gradient of the RH anomaly, a vertically dipolar $Q'_{R,LW,clear}$ with heating below and cooling above 500 hPa is generated that maximizes slightly ahead of the MJO precipitation center by 5° longitude (**Figure 4.5b**). The RH anomaly has a meridionally broad distribution to the north and south of the MJO center and ahead of the center at 15° longitude over 15°S-5°N, leading to a meridionally uniform heating at lower levels and cooling at upper levels at these reference longitudes (**Figures 4.5c, e**). The dipolar heating with opposite signs to the east and the west of the MJO center drives a weak circulation with a second baroclinic mode in both the zonal and meridional directions.

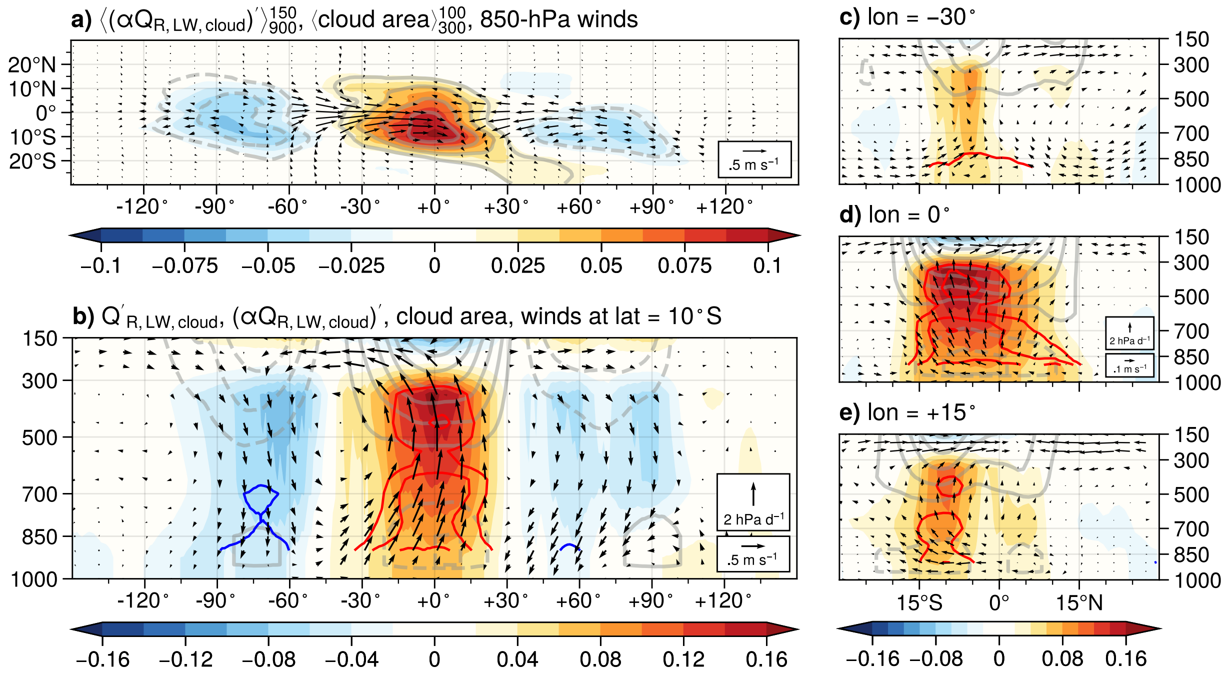

Figure 4.4. Anomalies in the composited MJO: (a) 900-150 hPa column-integrated $\left(\alpha Q_{R,LW,cloud}\right)'$ (shading; K day^{-1}), 100-300 hPa-averaged cloud area (gray contours; 0.5 % spacing), and 850-hPa horizontal winds (arrows; scale annotated) on the latitude-longitude plane, (b) $Q'_{R,LW,cloud}$ (shading), $\left(\alpha Q_{R,LW,cloud}\right)'$ (thin contours at 0.08, 0.12, and 0.16 K day^{-1}; positive in red and negative in blue), cloud area (thick gray contours; zero omitted; 0.5 % spacing), and winds (arrows; scale annotated) on a pressure-longitude cross section at 10°S, and (c-e) as in (b) but showing pressure-latitude cross sections at -30°, 0°, and 15° longitudes.

4.4.2.2 SW radiative effects

Figure 4.6 shows the 3-D structure of MJO SW CRE anomalies. The SW CRE weakly damps the column-integrated moistening at the MJO center by 0.02 K day^{-1} (shading in **Figure 4.6a**). A robust vertically dipolar structure is shown in $Q'_{R,SW,cloud}$, with a heating that maximizes at the tropopause following the cloud cover anomalies, and a cooling below 500 hPa that is strongest at the lowest levels (**Figure 4.6b**). Consistent with the discussion in **Chapter 4.4.1,** such a structure is generated by increased multiple scattering and absorption of SW radiative flux in regions of anomalously more high clouds. As $Q'_{R,SW,cloud}$ is induced by high clouds, it shows a horizontally similar pattern compared to $Q'_{R,LW,cloud}$: it is zonally asymmetric with a longer tail behind the MJO (**Figure 4.6b**), and has similar primary and secondary latitudinal peaks at different reference longitudes (**Figure 4.6c-e**). The dipolar vertical heating at the MJO center with opposite signed anomalies greater than 40° to the east and west induces a circulation with a second baroclinic mode structure, consistent with previous finding of SW radiative heating structure in convective systems (Ruppert & Hohenegger, 2018). The circulation partially cancels out the low-level winds induced by other MJO apparent heating terms, but enhances the upper-level winds (**Figure 4.2**).

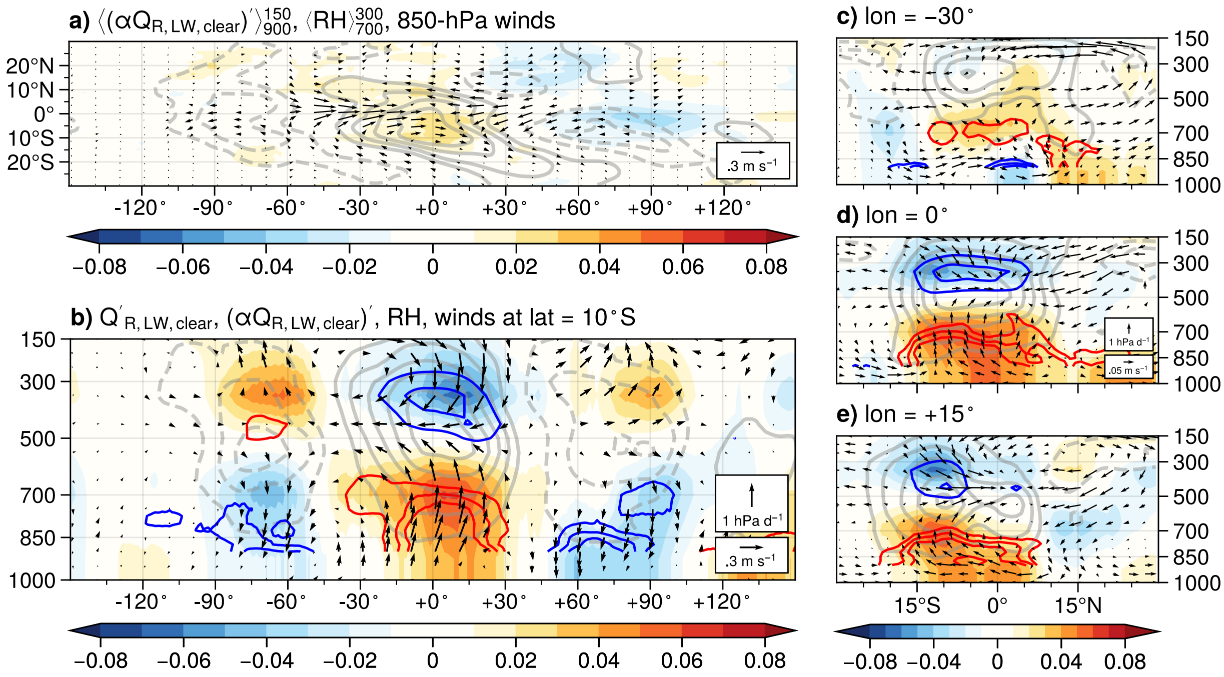

Figure 4.5. As in **Figure 4.4**, but for LW clear-sky heating (shading) and LW clear-sky moistening (thin contours), and thick gray contours for RH (0.5 % spacing).

Generated by the vertical gradient of RH’, clear-sky shortwave radiation anomalies have a similar structure but with an opposite sign to the clear-sky LW radiative effect, and are more top heavy (**Figure 4.7**). The magnitudes of its effect of moistening and circulation are small (**Table 4.1**), and so may not have major importance for the dynamics of the MJO, but are shown here for completeness.

4.4.2.3 The combined radiative effect

Since the LW CRE anomaly has the largest magnitude, the total effect of radiation on both circulations and moistening generally follows those induced by the LW CRE anomaly (**Figure 4.8**). One notable difference is that at -30° reference longitude behind the MJO center (**Figure 4.8c**), the vertical gradient of radiative heating at lower levels is higher than for the LW CRE anomaly alone due to the effect of SW anomalies, which induces strengthened meridional converging flow and westerlies to the west of MJO center below 700 hPa. This, as hinted previously, may weaken the inhibition of MJO propagation by WTG radiative moistening, which will be discussed later in **Chapter 4.5.3**.

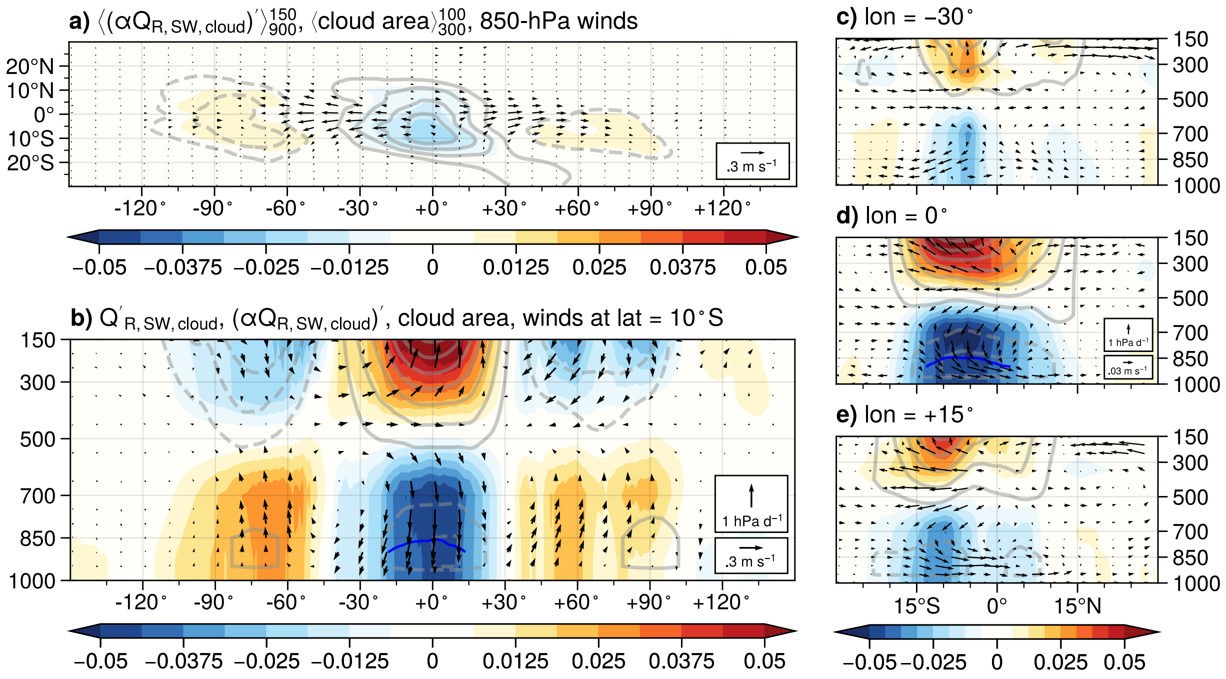

Figure 4.6. As in **Figure 4.4**, but for SW CRE heating (shading) and SW CRE moistening (thin contours), and thick gray contours for cloud area (0.5 % spacing).

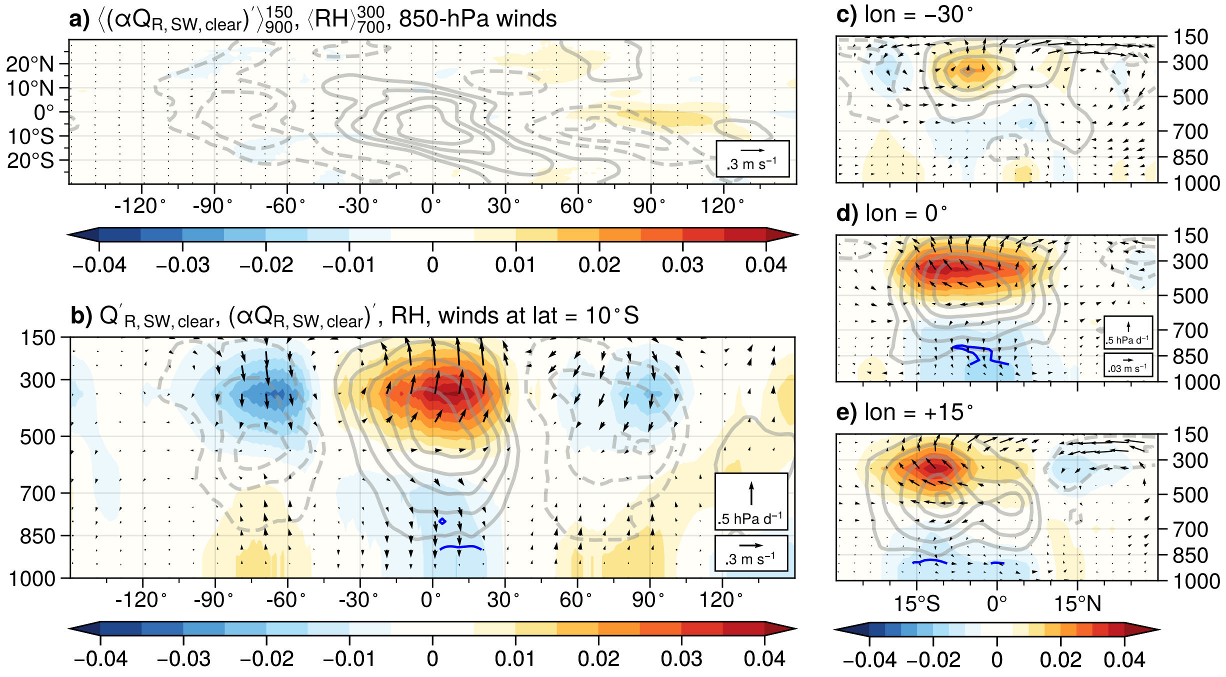

Figure 4.7. As in **Figure 4.4**, but for SW clear-sky heating (shading) and SW clear-sky moistening (thin contours), and thick gray contours for RH (0.5 % spacing).

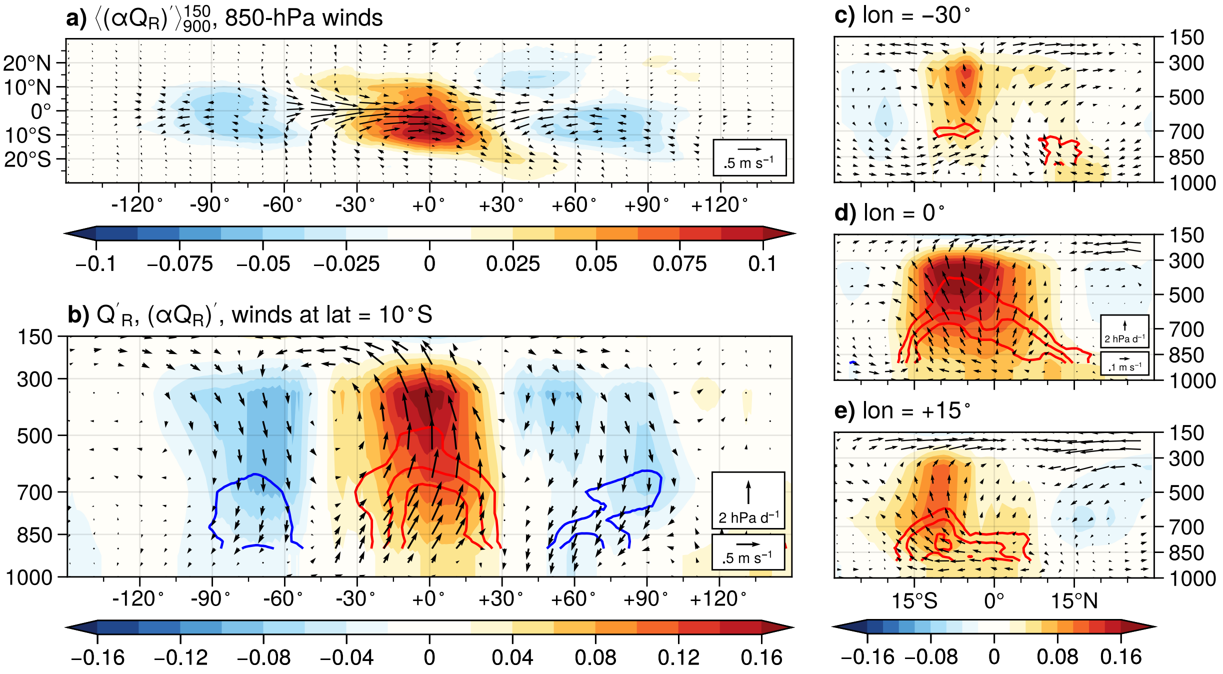
a) $\langle(\alpha Q_R)'\rangle_{900}^{150}$, 850-hPa winds

b) Q'_R, $(\alpha Q_R)'$, winds at lat = 10°S

c) lon = −30°

d) lon = 0°

e) lon = +15°

Figure 4.8. As in **Figure 4.4**, but for total radiative heating (shading) and total radiative moistening (thin contours).

4.5 Implication for MJO dynamics

4.5.1 MJO growth/propagation contributions

The section aims to quantitatively examine the impact of radiation on the dynamics of the MJO using the MSE (denoted as h) budget, with vertical advection and apparent heating terms decomposed using the WTG framework shown by **equation (4.6)**. The column-integrated MSE budget associated with the MJO at each phase can be decomposed as follows, with a reminder that superscript prime ($'$) denotes the MJO-associated anomaly (**Chapter 4.2.2**):

$$\langle\frac{\partial h'}{\partial t}\rangle_{tot} = \underbrace{-\langle u\frac{\partial h}{\partial x}\rangle'_{tot}}_{\substack{\text{zonal}\\ \text{advection}}} \underbrace{-\langle v\frac{\partial h}{\partial y}\rangle'_{tot}}_{\substack{\text{meridional}\\ \text{advection}}} \underbrace{-\langle \omega_C\frac{\partial h}{\partial p}\rangle'_{tot}}_{\substack{\text{non-radiative}\\ \text{vertical advection}}} \underbrace{+\langle \omega_R\frac{\partial h}{\partial p}\rangle'_{FT} + \langle Q'_R\rangle_{tot}}_{\substack{\text{total radiative effect}\\ \text{(FT vertival adv+total heating)}}} \tag{4.9}$$

$$+ LH' + SH'$$

where ⟨·⟩ denotes mass-weighted column integration over either the total troposphere (*tot*, 1000-150 hPa) or the free troposphere (*FT*, 900-150 hPa). Here, the radiative effect on MSE budget includes the induced WTG vertical advection in the free troposphere and also the direct effect of heating over the entire troposphere. Note that the sum of the two radiative effects is equal to the vertical advection of moisture under the WTG framework as shown by **equation (4.6)**, since the direct heating is canceled by the vertical advection of *s* to achieve zero *s* tendency. LH' and SH' denote the surface latent and sensible heat flux anomaly, respectively. Also note that the "non-radiative vertical advection" here also contains the vertical advection induced by radiation below 900 hPa, which cannot be estimated using the WTG framework. We then follow the variance budget decomposition of column-integrated MSE proposed by Andersen and Kuang (2012) to quantify how the WTG moistening induced by radiation contributes to the maintenance (S_m) and the propagation (S_p) of the MJO:

$$S_{m,Y} = \frac{\left\|\vec{Y}\cdot\overrightarrow{\langle h'\rangle}_{tot}\right\|}{\left\|\overrightarrow{\langle h'\rangle}^2_{tot}\right\|} \tag{4.10a}$$

$$S_{p,Y} = \frac{\left\|\vec{Y}\cdot\langle\partial\overrightarrow{h'}/\partial t\rangle_{tot}\right\|}{\left\|\langle\partial\overrightarrow{h'}/\partial t\rangle^2_{tot}\right\|} \tag{4.10b}$$

where ||·|| denotes the area average over the active MJO region (60°E-180°, 20°S-10°N), *Y* denotes a source term of the MSE budget on the RHS of **equation (4.7)**, and the vector symbols indicate that *Y* and *h* are functions of MJO phase and their inner product is calculated here.

The result of the decomposition is shown in **Figure 4.9**. Non-radiative processes ($-\omega_C \partial h/\partial p$) act to remove anomalously high MSE and causing the most negative contribution to the MSE maintenance (**Figure 4.9a**). The total radiative effect (RAD) has the most positive contribution to the MSE maintenance, dominated by the LW cloud effect, enhanced slightly by the clear-sky LW effect, and damped by the SW cloud effect (**Figure 4.9b**), consistent with the result in **Chapter 4.4**. For the MSE tendency budget (propagation), as the dominant LW cloud heating slightly lags the MJO center, the direct heating and the induced vertical advection of moisture by LW CRE slow down the MJO propagation (**Figures 4.9c-d**). However, the effect of LW CRE-driven horizontal circulation is not diagnosed in the present MSE budget analysis, which may damp the inhibition of MJO propagation by RAD as will be shown later in **Chapter 4.5.2**.

The residuals (RES) are not zero possibly due to the following reasons. The MSE budget is not strictly closed since (a) each MSE source term is calculated by regression onto OMI, (b) ERA5 impose additional tendency in MSE during data assimilation process, and (c) combining different observation products do not yield a closure of moisture, especially in the Indo-Pacific warm pool (Leitmann-Niimi et al., submitted). Nevertheless, comparing the magnitude of the non-zero residuals to the contribution by radiation shows that they do not hinder the robust effect of radiation on the maintenance and the propagation of the MJO.

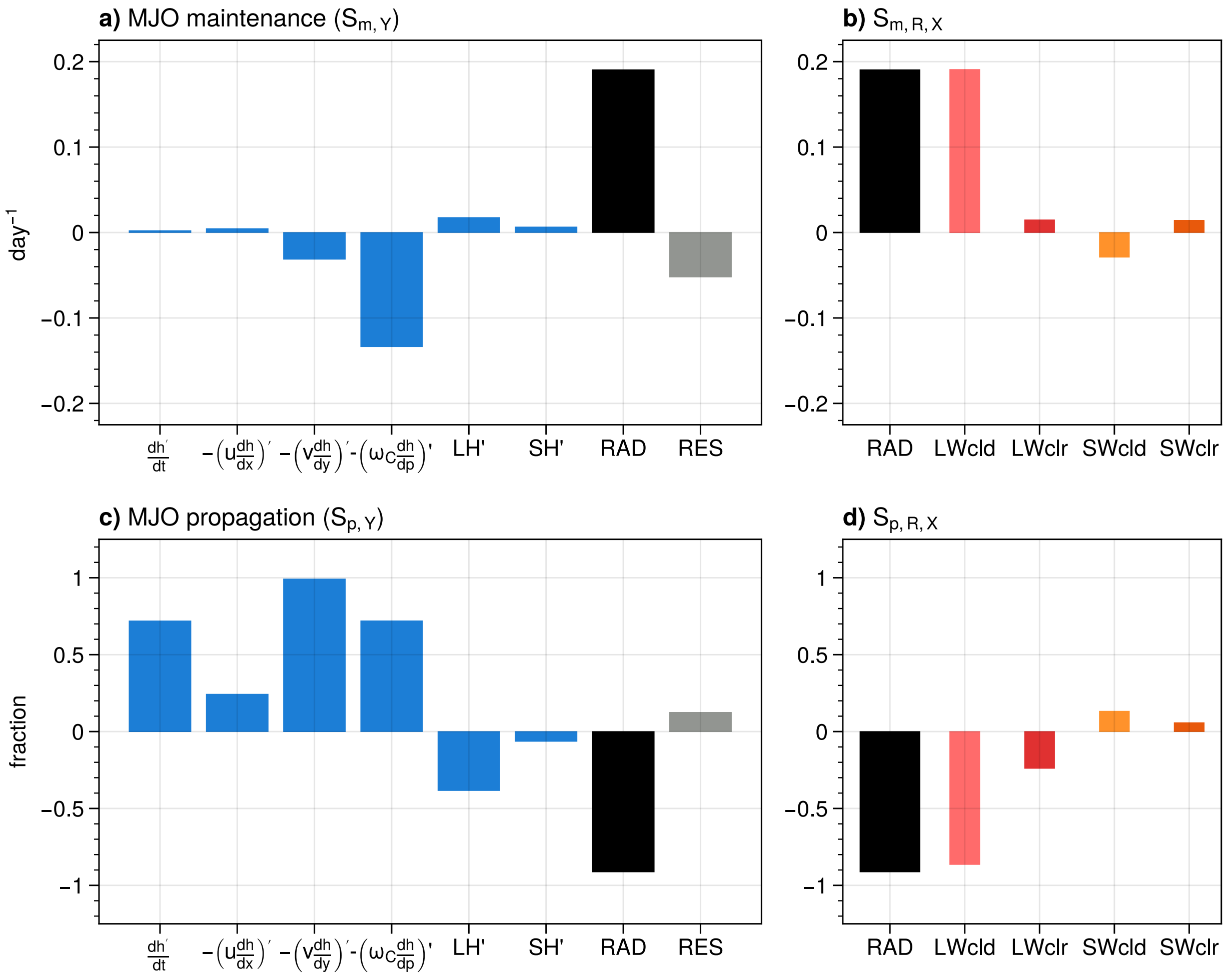

Figure 4.9. Contribution of each MSE source term to (a) MJO maintenance and (c) MJO propagation, with the notations same as in **equation (4.7)** but the total radiative effect as RAD and residual as RES. (b) and (d) shows the further decomposition for the total radiative effect of, from left to right, Q'_R, $Q'_{R,LW,cloud}$, $Q'_{R,LW,clear}$, $Q'_{R,SW,cloud}$, $Q'_{R,SW,clear}$.

4.5.2 Radiative contribution to MJO propagation

Horizontal advection of MSE greatly contributes to the propagation of the MJO (**Figure 4.9c**). The large positive contribution of MJO propagation by the meridional advection is consistent with previous studies that both mean flow and eddies transport drier air equatorward at lower levels behind the MJO center and provides anomalous moistening in front by reducing this drying effect (Adames & Wallace, 2015; Andersen & Kuang, 2012; Maloney, 2009). Positive contributions of propagation also come from the zonal advection, consistent with previous studies (Maloney, 2009). Although the total radiative effect (RAD) of WTG moistening strongly inhibits MJO propagation (**Figure 4.9c**), a question is how much of the horizontal advection terms is contributed indirectly through radiatively-driven horizontal circulation as shown in **Figures 4.4-4.8** which modifies the integrated radiative effect. Although the linear baroclinic model simulations provide radiatively driven horizontal winds, their total advection of MSE cannot be calculated due to lack of information on the effects of disturbances with timescales shorter than the MJO on horizontal advection (Maloney, 2009; i.e., the high-frequency eddy transportation terms; Peters et al., 2008). Instead, we simply compare the radiatively-driven horizontal winds at lower troposphere (850 hPa) derived in the simulations to the MJO-composite winds in ERA5 to elucidate the qualitative role of radiation on horizontal advection.

The spatial pattern of radiatively-driven zonal (u_R') and meridional winds (v_R') are largely collocated with and reinforce the MJO-composite winds (comparing contours to shading in **Figures 4.10c-d**), indicating that radiation enhances the general pattern of circulation in the MJO. Although Q_R' only consist of ~15% of total diabatic heating (**Table 4.1**), 850-hPa u_R' is ~30% of u' and v_R' is ~50% of v' behind the MJO center. This is likely due to the more bottom-heavy nature of radiative heating anomalies that drives stronger circulations at lower levels and the finding is consistent with Schumacher et al. (2004) who found that radiative heating drives tropical circulation maxima at lower levels.

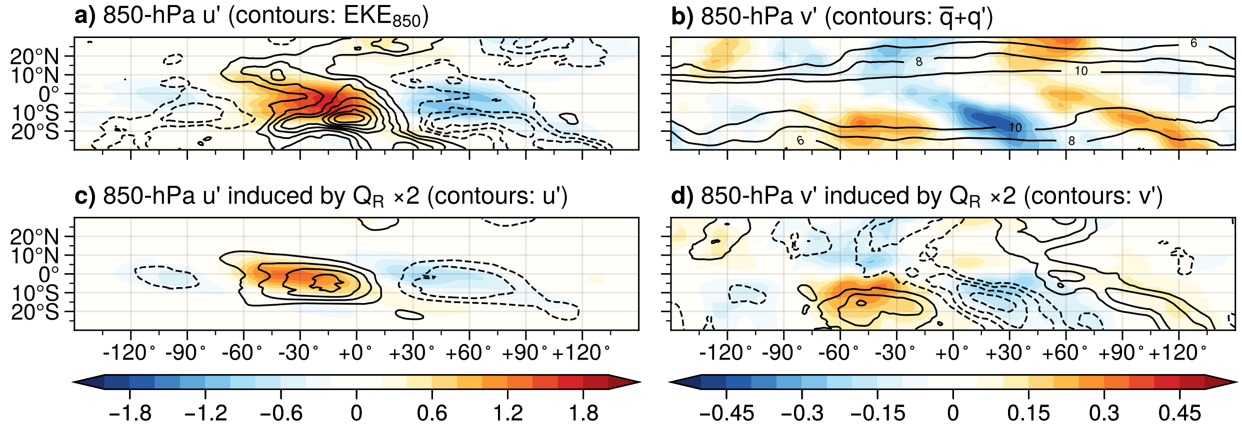

Figure 4.10. MJO-composite anomalies at 850 hPa: (a) u' (shading) and EKE850 (contours every 0.3 J kg^{-1} s^{-1} and zero omitted); (b) v' (shading) and total specific humidity $\bar{q} + q'$ (contours at 6, 8, and 10 g kg^{-1}); (c) u'_R multiplied by two (shading) and u' (contours every 0.2 m s^{-1} and zero omitted); (d) v'_R multiplied by two (shading) and v' (contours every 0.05 m s^{-1} and zero omitted).

As the background moisture decreases poleward (contours in **Figure 4.10a**), the MJO meridional wind anomalies contribute to the propagation of the MJO as it advects drier air equatorward to the west of the MJO center and reduces this effect to the east. The advection by v'_R yields a similar zonal pattern to the advection by v' (**Figure 4.11**), indicating a positive contribution of radiation to MJO propagation. As MJO westerly anomaly implies higher synoptic eddy activity associated with drying by eddy moisture transport, positive u' to the west and negative u' at lower levels to the east of the MJO center would enhance MJO propagation (e.g., Maloney, 2009; A. Sobel & Maloney, 2013). The reinforced 850-hPa zonal wind pattern by radiation thus implies further radiative contribution to the propagation of the MJO by high-frequency synoptic moisture transport. Stronger u' at 850 hPa correlates well with the eddy kinetic energy at 850 hPa (EKE850) defined as EKE850 = $(u''_{850} + v''_{850})/2$ (**Figure 4.10a**), where $('')$ indicates the 30-day high-pass filtering. Consistently, meridional-mean u' at 850 hPa has a negative linear relationship with the column-integrated eddy MSE transport $(v''\partial h''/\partial y)$ as shown in **Figure 4.12a**, and the slope (-3.62 J m^{-3}) can be used to diagnose the eddy MSE transport generated by u_R' by its multiplication by the slope (**Figure 4.12b**, red thick line). The diagnosed radiatively induced eddy transport is negative to the east and positive to the west of the MJO precipitation center, which helps the propagation of the MJO. Finally, we diagnose the quantitative contribution of radiatively-driven meridional MSE advection to MJO propagation in **Figure 4.13**, and found that it consists of 23% of the positive contribution by total meridional advection, which damps the inhibition by RAD by 24%.

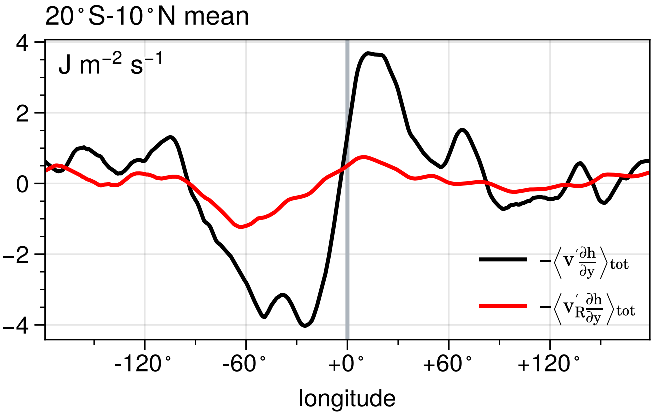

Figure 4.11. Meridional mean of 1000-150 hPa column-integrated MSE advection over 20°S-10°N by (black line) MJO *v* anomaly and (red line) MJO radiatively-driven *v* in the composited MJO.

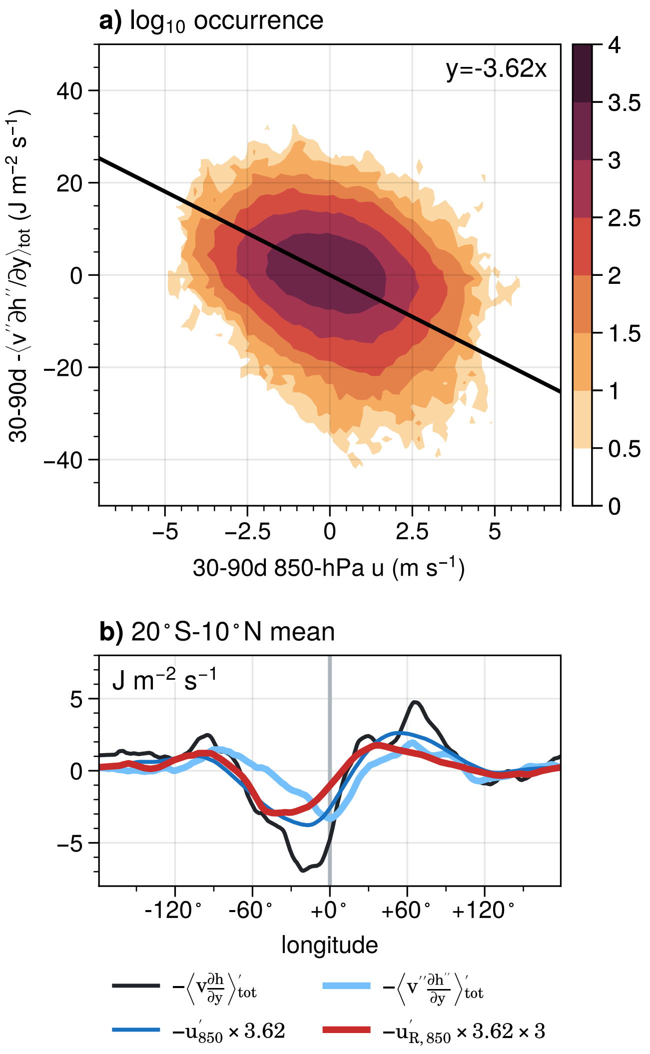

Figure 4.12. (a) joint frequency of occurrence of 30-90 day-filtered 850-hPa u and 30-90 day-filtered $\langle v''\partial h''/\partial y\rangle_{tot}$ shown in a logarithmic scale, with the slope derived by the leading eigenvector of the covariance matrix of the two variables on the axes. (b) Meridional mean of related quantities over 20°S-10°N as annotated at the bottom, including the eddy MSE transport diagnosed by u' (dark blue line) and u'_R (thick dark red line).

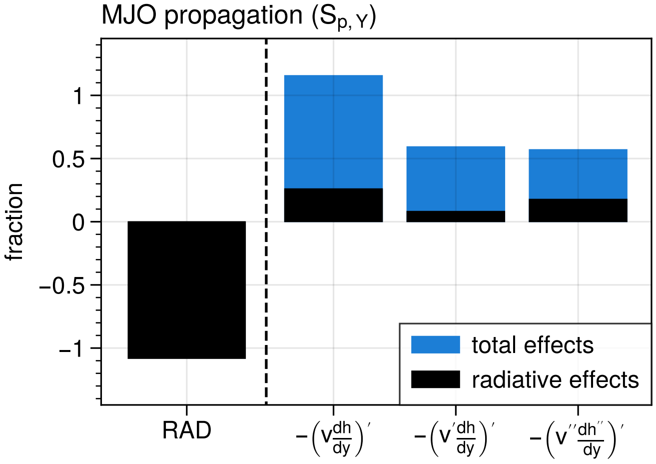

Figure 4.13. As **Figure 4.9d**, but from a calculation of **equation (4.10)** performed with meridional-mean Y, $\langle h' \rangle_{tot}$, and $\langle dh'/dt \rangle_{tot}$ to allow a diagnosis for high-frequency contribution using the regression in **Figure 4.12**. The columns from left to right show the contribution by RAD, and the contributions by different components of meridional MSE advection. Radiative contributions are in black, and the following numbers in parentheses are the fractional contribution by radiation: total meridional advection (23%), which includes meridional advection driven by MJO wind anomaly (14%) and meridional advection driven by high-frequency disturbances (31%). The total meridional advection by radiative effects damps 24% of negative contribution to MJO propagation by RAD.

To sum up, although the WTG moistening by radiation (RAD) strongly inhibits the propagation of the MJO, the horizontal circulation driven by radiation could damp this inhibition by enhanced meridional advection and synoptic disturbances behind the MJO. In addition, the fact that radiation drives ~30% of zonal wind also implies that radiation may also contribute to wind-induced latent heat flux anomalies, although LH' is a second order term to inhibit the propagation and enhance the maintenance of the MJO according to the budget derived (**Figure 4.9**).

4.5.3 Importance of radiation on the MJO enhancement events

So far, the role of radiation on the dynamics of the composite MJO lifecycle constructed using OMI is discussed extensively. The composite MJO, however, is perfectly cyclic with no growth or weakening of the system by definition. In this subsection, we examine how radiation anomalies contribute to the growth and weakening of the active region in individual MJO events.

The tropospheric-integrated $d(L_v q)/dt$ and the free tropospheric-integrated (αQ_R) within the MJO-band are extracted over the spectral range of planetary zonal wavenumber 1-5 and frequency of 30-90 days following Hayashi (1971) during 01 September 2002 to 31 August 2021. The MJO center longitude on each calendar day is identified as the maximum of the filtered precipitation anomaly averaged over 20°S-10°N, and is only included when the OMI magnitude is greater than or equal to 0.5 and when the precipitation maximum is propagating eastward with a physically reasonable speed ≤ 15 m s^{-1}. The results are not sensitive to the selection criteria over 0.0-1.0 OMI magnitudes and 10-23 m s^{-1} propagation speeds. The Lagrangian tendency of the meridional-mean $\langle D(L_v q)/Dt \rangle_{tot}$ anomaly at the MJO center longitude is then calculated, as shown in the x-axis of **Figure 4.14**. About half of the MJO events grow (right half of the plot) while the other half decay. To elucidate the role of radiation, the meridional-mean $\langle \alpha Q_R \rangle_{FT}$ anomaly at the MJO center longitude is calculated (y-axis of **Figure 4.14**). The points above the line where $\langle D(L_v q)/Dt \rangle'_{tot} = \langle \alpha Q_R \rangle'_{FT}$ are the days when MJO cannot grow without radiation (blue dots), while the MJO can grow with radiation below the line (red dots). When the humidity at the MJO center is growing (right half of the plot), only during 10% of the days the MJO center can be moistened without radiative effects (red dots).

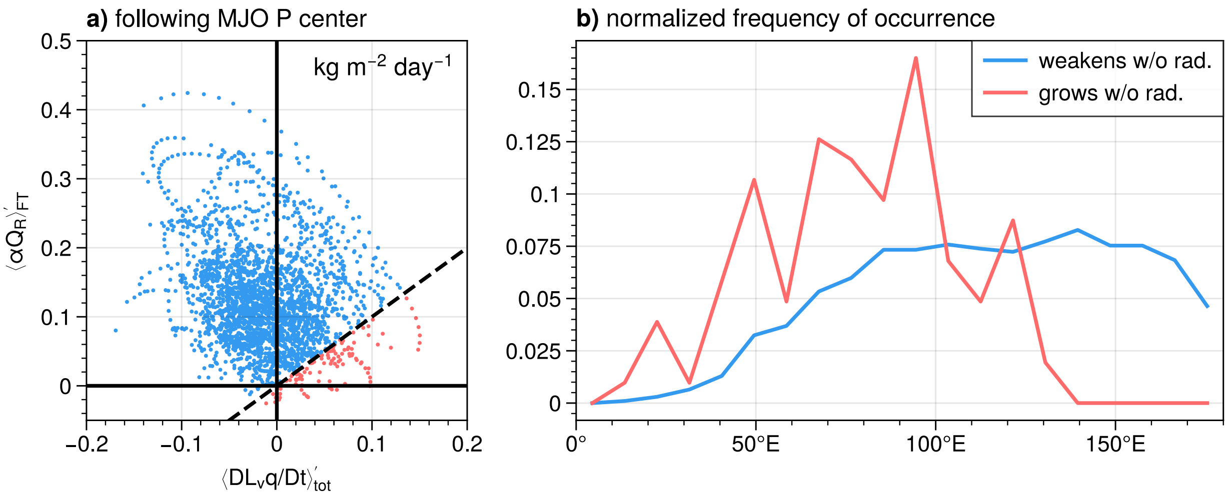

Figure 4.14. (a) A scatter plot of (x-axis) total moistening and (y-axis) radiative moistening at the MJO center. The dashed line indicates when radiative moistening is equal to the total moistening. The MJO center is dried without radiation above the dashed line (blue dot) and vice versa (red dots). (b) The longitudinal frequency of occurrence of the red and the blue dots shown in (a).

Inspecting the frequency of occurrence of MJO center longitude (**Figure 4.14b**) shows that the events that grow without radiation are more likely to occur in the Indian ocean (50°E-100°E) than in the western Pacific (100°E-150°E). This implies other processes anomalously enhance the MJO over the Indian ocean. The normalized contribution to 1000-150 hPa column-integrated moisture tendency following the MJO center in the two regions (**Figure 4.15**) shows that the Indian ocean has less moisture damping by precipitation tendency. The damping by precipitation tendency being the only term that has a higher value in the Indian ocean over the western Pacific implies that this term contributes to the anomalously less fractional contribution of moistening by radiation in the Indian ocean. This regional difference may be explained by the lower precipitation efficiency in the Indian ocean over the western Pacific (R. L. Li et al., 2022).

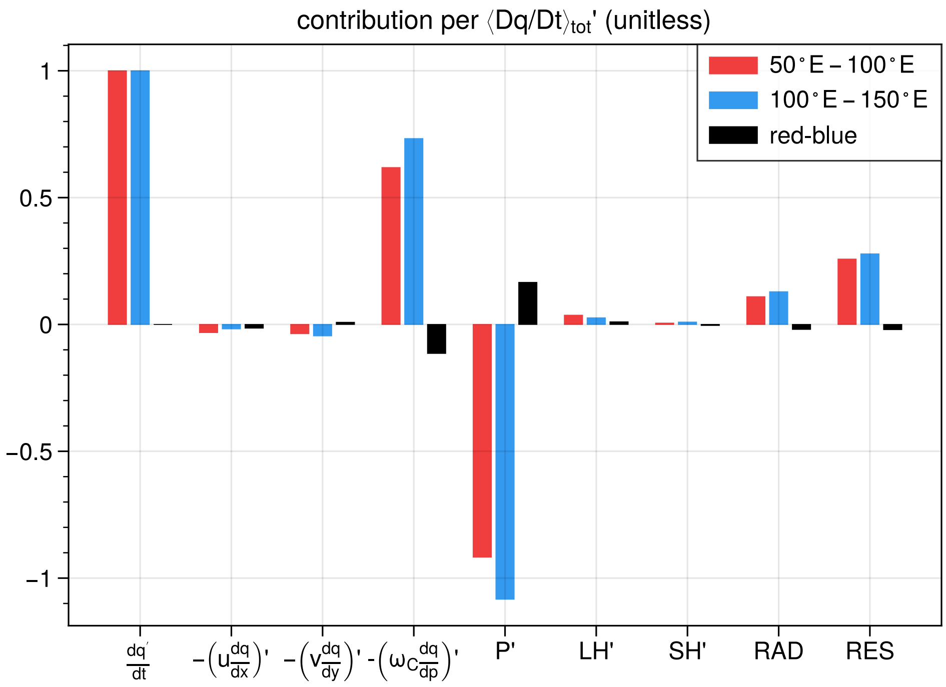

Figure 4.15. Contribution of individual moistening terms per unit column-integrated moisture tendency following the MJO center in all the growing events as identified in **Figure 4.14a**. Red indicates the averages of events when the MJO center lies in 50°E-100°E, and blue for 100°E-150°E. Black bars indicate the value of red minus blue bars.

4.6 Summary

Radiative feedbacks drives the dynamics of the MJO not only through the direct heating of the atmosphere, but also through moistening effects driven by the radiatively driven circulation. This study aims to provide a thorough examination of the three-dimensional structures of radiative heating and radiatively driven circulations and moistening of the MJO using observational datasets including CERES SYN1deg (**Figures 4.4-4.8**).

Column moistening processes by the advection of radiatively driven vertical velocity are diagnosed using a WTG framework (**Figure 4.3** and **Table 4.1**). LW CRE dominates contributions to moistening by vertical advection at the MJO convective center. Contributed by the bottom-heavy LW clear-sky radiative heating, which imposes upward motion at lower levels where the vertical moisture gradient is large, the total LW radiative effect moistens the MJO more efficiently than Q_1' per unit column heating. SW radiative heating has a near-zero column-integrated value. However, its dipolar vertical structure with heating aloft and cooling below generates a damping of the moistening at the MJO convective center. The total radiative feedback of column heating and associated moistening by vertical advection dominates the maintenance of the MJO among other sources in the MSE budget (**Figure 4.9**). Further analysis tracking the center of MJO convective events reveals that radiative feedback is essential for 90% of amplifying MJO events (**Figure 4.14**). The 10% of events that do not require radiative feedback to amplify occurs more frequently in the Indian ocean, which is aided by the weaker precipitation tendency that removes less atmospheric moisture when the MJO amplifies (**Figure 4.15**).

Radiative heating anomalies also induce horizontal circulations. While the radiatively driven horizontal winds are not analytically derivable, simulations conducted by a linear baroclinic model allow us to infer the horizontal winds driven by MJO radiation heating anomalies (**Figures 4.4-4.8**). It is found that despite $\langle Q_R' \rangle_{FT}$ being 15% of $\langle Q_1' \rangle_{FT}$ (**Table 4.1**), the low-level winds driven by radiative heating perturbations are more robust than for Q_1' per unit column heating (**Figure 4.10**), likely due to the bottom heaviness of the radiative heating structure that drives low-level circulations more efficiently. Q_R' enhances the overall anomalous circulation of the MJO, accounting for 30% of the lower troposphere zonal wind anomalies and 50% of meridional wind anomalies (**Figure 4.10**). Although the WTG moistening by radiative effects strongly inhibits the propagation of the MJO (**Figure 4.9**), radiatively driven horizontal winds likely damp such inhibition by ~25% (**Figures 4.11-4.13**). Enhanced low-level zonal wind also suggests that LH' can be partly driven by radiation.

As suggested in the WTG framework, the vertical structure of radiative heating is critical in determining the column moistening or drying efficiency per unit column heating. A robust example is that $\langle Q'_{SW} \rangle_{FT}$ is nearly zero while generating column drying due to its outsized influence on moisture advection in the lower troposphere (**Table 4.1**). As most studies use OLR as a proxy of the column-integrated radiative heating anomalies, overly simplifying the vertical structure of this heating (which is typically assumed to be the same as Q_1) can cause large errors in estimating the moistening driven by radiative effects. This study provides an overview of how MJO radiative heating profiles and associated circulations present themselves in observational-derived products, which helps deepen our understanding of MJO dynamics, and may also provide process-based diagnostics to help identify possible errors in the radiative effects in numerical models that lead to deficient MJO simulations.

CHAPTER 5

Spatially Inhomogeneous Longwave Cloud-radiative-convective Feedback in Tropical Intraseasonal Variability

5.1 Introduction

Tropical intraseasonal variability significantly contributes to tropical precipitation variability and affects circulations over the globe (C. Zhang et al., 2013 and reference therein). Such variability is largely maintained by radiative feedbacks (e.g, Andersen & Kuang, 2012; J.-L. Lin & Mapes, 2004b; Maloney, 2009). High clouds generated at its deep convective center absorb longwave (LW) radiative fluxes emitted from the lower troposphere, which heats up the atmosphere and induces upward motion that aids the moistening of the convective center. The process effectively reduces the gross moist stability (Raymond et al., 2009), and thus aids the growth of tropical intraseasonal variability (Adames & Kim, 2016; Z. Fuchs & Raymond, 2005; A. Sobel & Maloney, 2013). This LW cloud radiative feedback (LW CRF) is also found to support mesoscale convection and tropical cyclones (Ruppert et al., 2020; Ruppert & Klocke, 2019).

Despite the importance of the LW CRF to the dynamics of tropical variability, the understanding of such feedbacks is limited. For example, LW CRF is typically considered to be constant in theoretical models despite there being attempts to quantify it by precipitation strength and by zonal wavenumber (Adames & Kim, 2016; Kim et al., 2015). Thinking about how LW CRF is generated through production of high clouds by deep convection, the feedback should not be constant, as the structure of convection should highly modulate the associated high cloud amounts. For example, Hsiao et al. (2024) show that more mesoscale organization leads to more efficient production of cirrus clouds and thus stronger LW CRF, aided by higher sea surface temperature (SST) and high low-level wind shear. Lin and Mapes (2004a) proposed that deep-layer wind shear helps the spreading of high clouds and modulates outgoing longwave radiation (OLR) over the western tropical Pacific. If these physical processes modify the strength of LW CRF, as different spatial locations have different large-scale fields providing different convective environments, the spatial pattern in the LW CRF should be non-constant.

The study focuses on examining the spatial pattern of the LW CRF in the austral summer Madden-Julian oscillation (MJO), the dominant mode of tropical intraseasonal variability. The LW CRF is quantified using CERES (see **Chapter 5.2.1**), which provides atmospheric radiative heating profiles and observational precipitation datasets. We show that the feedback is not spatially uniform in **Chapter 5.3**, and the possible causes of such spatial variability are examined in **Chapter 5.4**. Implications for MJO dynamics is discussed in **Chapter 5.5**. Conclusions are provided in **Chapter 5.6**.

5.2 Methodology

5.2.1 Data and filtering method

The top-of-atmosphere (TOA) OLR (denoted as R) is commonly used to calculate atmospheric longwave radiative heating perturbations above the tropical warm-pool ocean when assuming surface longwave radiative flux anomalies are negligible. The daily-mean 1° × 1° National Oceanic and Atmospheric Administration Interpolated OLR (NOAA OLR; Liebmann & Smith, 1996) is used to estimate the heating perturbations.

To obtain a more accurate estimate of the atmospheric radiative feedback, the Level-3 product Clouds and the Earth’s Radiant Energy System Synoptic 1 degree Edition 4.1 (CERES SYN1deg Ed4.1; Doelling et al., 2013, 2016; Loeb et al., 2018) is used, which provides daily-mean radiative heating rates on pressure levels with a 1° × 1° horizontal resolution. Radiative fluxes in the product are generated by a radiative transfer model, with inputs of satellite-retrieved cloud properties and TOA radiative fluxes, and a real-time analysis of atmospheric conditions. The radiative fluxes are provided at six vertical levels (TOA, 70 hPa, 200 hPa, 500 hPa, 850 hPa, and the surface) which are then used to calculate atmospheric radiative heating rates at five vertical levels centered at 35 hPa, 135 hPa, 450 hPa, 675 hPa, and 925 hPa. Clear-sky radiative fluxes are calculated by removing the retrieved clouds properties in the radiative transfer model, and the cloud radiative effect (CRE) is defined in the present study by subtracting the clear-sky heating from the all-sky heating. We focus on the LW CRE, denoted as Q_R, in this study. Cloud covers (C) are also provided in CERES SYN1deg in four different pressure ranges, for high clouds (C_{high}; 0-300 hPa), mid-high clouds ($C_{\mathrm{mid-high}}$; 300-500 hPa), mid-low clouds ($C_{\mathrm{mid-low}}$; 500-700 hPa), and low clouds (C_{low}; 700-1000 hPa), which are plotted in this study in pressure coordinate using their mid-point pressure levels.

Atmospheric zonal (u), meridional (v), and vertical (ω) winds, specific humidity (q), and dry static energy (DSE; denoted as s) in the European Centre for Medium-Range Weather Forecasts Reanalysis v5 (ERA5; Hersbach et al., 2020) are used, which has a native resolution of hourly and 0.25° × 0.25° but regridded to daily means and 1° × 1°. The 0.5° × 0.5°, daily-mean Global Precipitation Climatology Project version 3.2 (GPCPv3.2; Huffman et al., 2023) is used for surface precipitation (P) after regridding to 1° × 1°. With the inclusion of spaceborne precipitation radar observations from the Tropical Rainfall Measuring Mission (TRMM; Kummerow et al., 1998) and the Global Precipitation Mission (GPM; Hou et al., 2014), GPCPv3.2 yields larger daily surface precipitation variability in tropical marine regions compared to the previous global precipitation products (Hsiao & Maloney, 2024; Z. Li et al., 2023), such as GPCP version 1.3 (GPCPv1.3; Huffman et al., 2001). Particular analyses in this manuscript are also performed using GPCPv1.3 to test the robustness of findings.

To isolate the anomalies associated with the MJO, a temporal band-pass Lanczos filter for 30-90 day variability with a 101-day window is applied to the data products described above after removing the first three harmonics of the climatologies and the trends in 01/09/2002-31/08/2021. Filtered data centered over 01/07/2003-30/06/2021 are retained. The present study primarily studies the austral-summertime MJO radiative feedback, so data over the extended-austral summer (November-April, or NDJFMA) is used. The filtered anomalies are denoted by a subscript prime (‘). For example, R’ and P’ denote 30-90 day-filtered OLR and surface precipitation anomalies, respectively.

5.2.2 Defining LW CRF

The LW CRF is estimated in two approaches in this study. The OLR LW CRF (f_{OLR}) is defined as the linear regression slope of -R’ onto P’, which is a commonly used quantity to estimate LW CRF (Adames & Kim, 2016; Kim et al., 2015; e.g., J.-L. Lin & Mapes, 2004b; Peters & Bretherton, 2005). Here, P’ originally in units of mm day^{-1} is converted to W m^{-2} by multiplying the latent heat of condensation (L_v) and the density of water to yield a non-dimensional f_{OLR}. While -R’ does not strictly represent MJO atmospheric LW CRE, the advantage of using NOAA OLR is that the product retrieves OLR over the whole globe using a consistent series of satellite observations by the Advanced Very-High-Resolution Radiometer (AVHRR) equipped on NOAA-16 and NOAA-18. This consistency provides better confidence in the spatial variability of LW CRF as discussed later in the manuscript.

The LW CRF is also estimated using the weak-temperature-gradient (WTG) moistening LW CRF (f_{m}) to better characterize the integrated effect of LW CRE on the column moistening of MJO convection. Under WTG approximation, which is applicable over the tropical warm pool above 900 hPa, apparent heating generated by LW CRE is balanced by an associated component of upward motion to achieve zero local DSE tendency. This vertical motion driven by LW CRE can be expressed as:

$$\omega_R = \begin{cases} Q_R(\partial s/\partial p)^{-1}, & p \leq 900\,hPa \\ 0, & p > 900\,hPa \end{cases} \tag{5.1}$$

The vertical velocity driven by LW CRE vertically advects moisture, causing a column moistening effect, which can be expressed as:

$$\left(\frac{\partial L_v q}{\partial t}\right)_{R,col} = \left(-\frac{\partial L_v q/\partial p}{\partial s/\partial p}\right) Q_R = \alpha Q_R \tag{5.2}$$

where the Chikira parameter α (Chikira, 2014), the negative ratio of moisture stratification to dry static stability, represents the efficiency of moistening per unit apparent heating. The mass integration of the moistening rates over free troposphere (FT; 900-150 hPa) is then used to indicate the moistening driven by Q_R:

$$\langle \alpha Q_R \rangle_{FT} \equiv \frac{1}{g} \int_{900\,hPa}^{100\,hPa} \alpha Q_R \, dp \tag{5.3}$$

This term represents the effect of circulation driven by LW CRE on moistening and moist static energy (MSE) tendencies through vertical advection, instead of representing temperature tendency imposed by LW CRE such as by OLR or Q_R. Finally, f_{m} is estimated as the linear regression slope of $\langle \alpha Q_R \rangle'_{FT}$ onto P'. Similar as in calculating f_{OLR}, both $\langle \alpha Q_R \rangle'_{FT}$ and P' are converted to the units of W m^{-2}, with $\langle \alpha Q_R \rangle'_{FT}$ multiplying the specific heat of air at constant pressure (c_p), to yield a non-dimensional f_{m}. As column moisture is more directly associated with deep convective activity (e.g., Bretherton et al., 2004), we believe that f_{m} more directly represents the radiative-convective feedback that destabilizes the atmosphere, as demonstrated implicitly in effective and critical gross moist stabilities (Inoue & Back, 2015; Raymond et al., 2009; Yasunaga et al., 2019) and in moisture mode theories (Adames & Kim, 2016; Z. Fuchs & Raymond, 2005; A. Sobel & Maloney, 2013).

While of using f_{m} to estimate LW CRF has the advantage of more accurate meaning for tropical deep convective systems, a caveat is that as CERES SYN1deg incorporates different geostationary satellite observations for cloud retrieval, the spatial pattern of f_{m} can be partly affected by the artifacts of instrumental biases at different longitudes. However, we found that the spatial discontinuity at the edges of geostationary satellite scenes of the filtered C', Q_R', and f_{m} is not apparent, likely because the temporal filtering removes the climatologies and trends. We further compare f_{m} to f_{OLR} and found very similar spatial patterns (**Figures 5.2a-b**), thus suggesting that possible artifacts from geostationary satellite observations do not affect our main conclusions.

5.3 The spatially non-uniform LW CRF

5.3.1 Intraseasonal OLR does not entirely match intraseasonal precipitation

To motivate the study of the spatial pattern of LW CRF, we first show that LW CRF is not spatially uniform over the Indo-Pacific warm pool - the active region of the MJO, by taking the following "minimalist's approach". We simply inspect the MJO amplitudes of *P*' and *R*' defined as their root-mean-square over the entire periods of interest (**Figures 5.1c-d**). Comparing *P*' amplitude (**Figure 5.1c**) to climatological *P* (**Figure 5.1a**) shows that *P*' has larger amplitudes in the following regions, outline by the red contours at 100 W m^{-2}: the Intertropical Convergence Zone (ITCZ) extended zonally from the tropical Indian ocean to the tropical central Pacific near

150°W, 10°N, with sporadic local maxima over the Maritime Continent to the east of Malay Peninsula, north of Borneo, and east of Luzon; the Southern Pacific Convergence Zone (SPCZ), extended zonally from Timor Sea to the tropical south-central Pacific at around 150°W, 20°S. However, *R*' amplitude (**Figure 5.1d**) does not match the spatial pattern of *P*' amplitude (**Figure 5.1c**), in that only the tropical Indian ocean and a part of the SPCZ region extended from Timor Sea to Coral Sea outlined by the red contours at 16 W m^{-2} matches where there are high *P*' amplitudes, while *R*' amplitude is small over the Maritime Continent and the western to central Pacific ITCZ, and the east edge of SPCZ. These results imply that LW CRF may be stronger over the tropical Indian ocean and near northern Australia, but weaker over the Maritime continent, the Pacific ITCZ, and the eastern edge of SPCZ.

Inspecting the meridional mean over the active latitudes of the MJO (20°S-10°N) shows a consistent result (**Figure 5.1e**). *P*' and *R*' amplitudes approximately covary over 60°E-135°E but deviate to the east of 135°E, such that *P*' amplitude is higher but *R*' amplitude is either similar or smaller to that to the west. The ratio of meridional mean *R*' to *P*' amplitudes (**Figure 5.1e**), as a rough indicator of the zonal structure of LW CRF, is high in the tropical Indian ocean from 0.2 at 60°E decreasing eastward to 0.16 at 100°E, and locally peaking near 0.18 in the Timor Sea at 120°E, and decreasing eastward to 0.12 at 180°E. **Figure 5.1** is reproduced using GPCPv1.3 precipitation and shows a similar mismatch in the spatial patterns of *P*' and *R*' amplitudes, but with overall lower values of *P*' amplitude and higher ratios of *R*' to *P*' amplitudes (**Figure A5.1**). The mismatch of *P*' and *R*' amplitudes indicates a rich spatial structure of LW CRF. However, while both MJO *P*' and *R*' amplitudes have been individually studied in previous studies, little attention is given to this mismatch. One example of previous studies is that Lin and Mapes (2004b) found a similar zonal structure in the ratio of OLR to precipitation in their Figure 13c compared to **Figure 5.1f** in the present study.

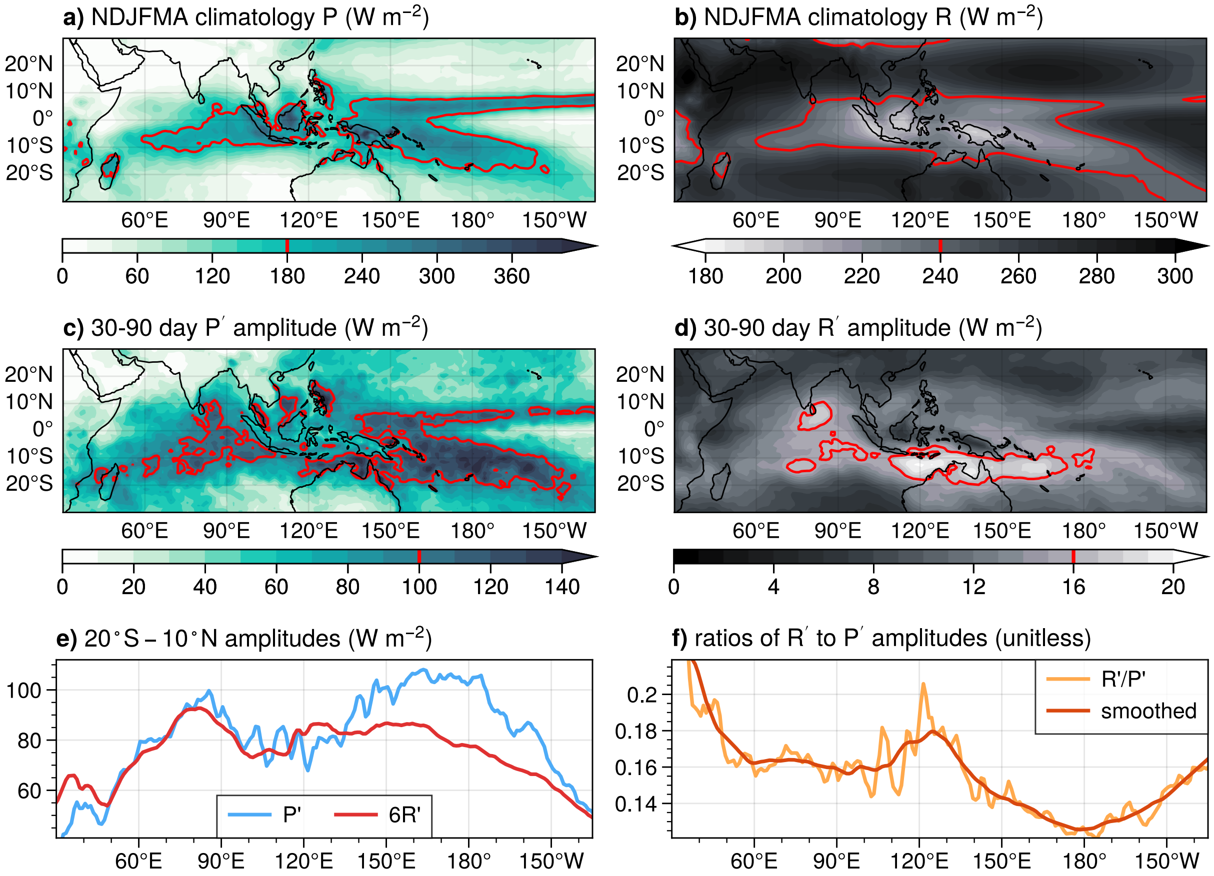

Figure 5.1. Extended austral-summer climatologies of (a) surface precipitation (*P*) and (b) OLR (*R*). (c) composite *P*' amplitude, (d) composite *R*' amplitude, (e) 20°S-10°N meridional-mean *P*' and 6×*R*' amplitudes, and (f) the ratios of 20°S-10°N meridional-mean *R*' to *P*' amplitudes and the smoothed by 21°-longitude running mean.

5.3.2 The spatial structure of LW CRF

The spatial structure of the WTG moistening LW CRF (f_m) defined in **Chapter 5.2.2** is calculated (**Figure 5.2a**). Note that grids with land area > 90% are masked in gray color since αQ_R commonly has unphysical values below 650 hPa. f_m has a complicated spatial pattern. Relatively higher values above 6% occur over the tropical Indian ocean, with very high values above 9% near the coast of Arabian Sea. Relatively lower values below 6% are frequently found in the tropical Pacific ocean, with very low values below 4% concentrated near the ITCZ at 180° longitude (compared to **Figure 5.1a**). Values are very small in the Indian ocean south of 20°S. The maximum values above 10% occur to the northwest of Australia, extending from the south of Java to the Timor and Arafura Seas. Sporadic local maxima are located near islands and coastlines, such as to the west of Luzon, the south of the Indochina Peninsula, and the west of the Bay of Bengal. The spatial patterns of f_m and f_OLR (**Figure 5.2b**) are very similar, which indicates that longitudinally-dependent satellite instrumental biases do not affect the spatial pattern of f_m (see **Chapter 5.2.2**).

The rich spatial structure of LW CRF is intriguing in its implication for the MJO, as the dynamics of the MJO is strongly modulated by LW CRF (**Chapter 5.1**). While the implication for the MJO dynamics will be examined in **Chapter 5.5**, a first question is *why does the spatial pattern exist?* How efficient MJO precipitation generates LW CRF varies by location. Since LW CRE is mostly generated by high clouds (Webster & Stephens, 1980), we examine the spatial pattern of the high-cloud cover production efficiency, defined as the linear regression slope of C'_high onto P' (the C'_high-P' slope; **Figure 5.2c**). The C'_high-P' slope has a very similar spatial structure to f_m and f_OLR, such that all the maxima and minima regions described in the previous paragraph over the oceanic grid points match, suggesting that C'_high is the main physical driver of LW CRE. The question is then asked: *why does the spatial pattern of the* C'_high-P' *slope exist?*

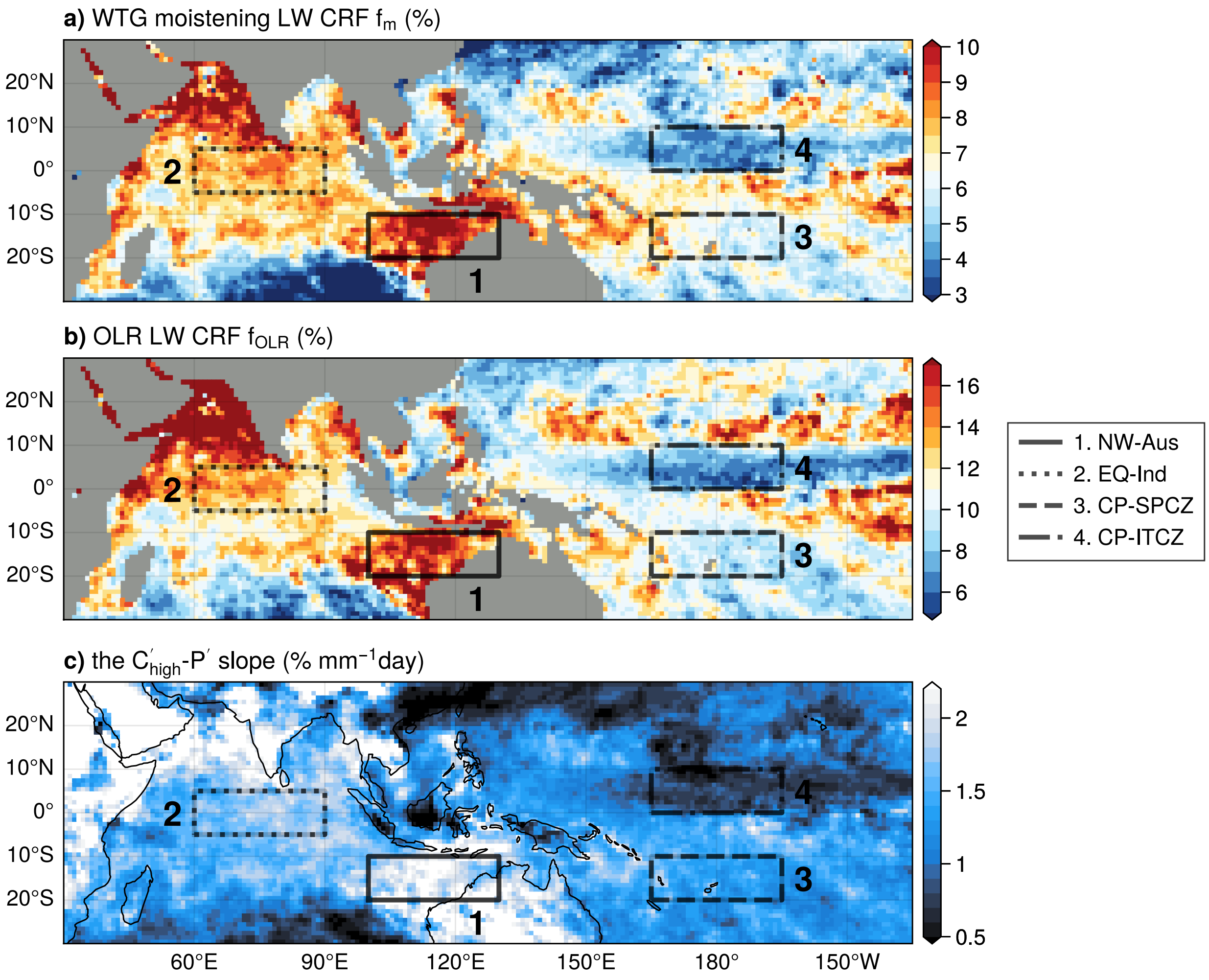

Figure 5.2. The spatial patterns of (a) f_{m} (%), (b) f_{OLR} (%), and (c) the C'_{high}-P' slope (% mm^{-1} day). Four characteristic regions as described in text are enclosed and annotated. Note that a diverging color map is chosen for (a-b) to more clearly show the spatial pattern with respect to the domain-mean LW CRF.

5.4 The cause of the different values of LW cloud-radiative feedback

5.4.1 Overview

Chapter 5.3.2 suggests that MJO precipitation produces high clouds differently by location, which is the underlying reason why the rich spatial structure of LW CRF exists. Here, we briefly overview relevant physical processes for high cloud production by convection. High clouds are mostly generated by deep convection, when convective plumes reaches the tropopause region where the level of neutral buoyancy locates in the convective environment, which leads to large-scale detrainment that transports moisture and hydrometeors into the stratiform regions of the convective system (Houze, 2004 and reference therein). These high clouds rain and partly diminish within the convective system's life span through stratiform precipitation, and the remnants linger at the upper troposphere as thin cirrus clouds that even present in the less convective environments (B. Wolding et al., 2023). On the other hand, precipitation generated by systems that are not associated with deep convection are not likely to support high cloud production. Thus, the variability in the C'_{high}-P' slope is likely linked to the depth of convection. Other factors also likely affect the variability in high cloud amounts, such as the fraction of water transportation from convective to stratiform regions (as the term CA in Gamache & Houze, 1983), and aerosol types and concentrations that could modify the radiative properties and the lifetime of high clouds.

To discuss the possible causes of such spatial patterns more clearly in the this section, four regions of distinct f_{m} characteristics are selected for convenience: (1) Northwest of Australia (NW-Aus; 100°E-130°E, 20°S-10°S), (2) Equatorial Indian Ocean (EQ-Ind; 60°E-90°E, 5°S-5°N), (3) Central-Pacific ITCZ (CP-ITCZ; 165°E-165°W, 0°-10°N), and (4) Central-Pacific SPCZ (CP-SPCZ; 165°E-165°W, 20°S-10°S). The order is ranked by the areal mean values of f_{m}, as well as for f_{OLR} and the C'_{high}-P' slope (**Table 5.1**). NW-Aus is selected to examine why there is maxima f_{m}; EQ-Ind is selected to be compared with CP-SPCZ on why the tropical Indian ocean has generally larger f_{m} than in the tropical western-to-central Pacific; CP-ITCZ is selected to examine why there is minima f_{m}.

Table 5.1. The areal mean averages of f_m, f_{OLR}, and the C'_{high}-P' slope, with their 95% confidence intervals in parentheses. The average composite P' amplitude is also shown for reference. Note that grids with land area > 90% are excluded while averaging.

	1. NW-Aus	2. EQ-Ind	3. CP-SPCZ	4. CP-ITCZ
f_m (%)	9.50	7.90	6.32	4.35
f_{OLR} (%)	15.65	13.10	9.77	7.33
the C'_{high}-P' slope (% mm^{-1} day)	2.03	1.71	1.37	0.78
P' amplitude (mm day^{-1})	3.02	3.39	4.51	3.33

5.4.2 Vertical structure of convection and clouds

The vertical structure of convection in the four regions of interest are examined (**Figure 5.3**). Note that the vertical profiles here should be interpreted as the result of the collective behavior of all types of convective systems, as we are inspecting the multiyear composites of 30-90 day-filtered signals. The amplitude of filtered apparent heat source (Yanai et al., 1973), Q_1', has different magnitudes in the four regions (**Figure 5.3a**), mostly depending on surface precipitation rates. To examine the difference in their structures, the areal-mean Q_1' amplitudes are normalized by the areal-mean P' amplitudes, in which all four lines collapse to a similar range (**Figure 5.3d**). All regions have Q_1' amplitudes maximizing at 500 hPa, except for EQ-Ind that maximizes at 450 hPa, indicating that EQ-Ind has more top-heavy latent-heat release likely generated by more stratiform precipitation in convective systems. This helps explain why EQ-Ind has higher f_m than in CP-SPCZ. Although the Q_1' amplitude maximized at 500 hPa for NW-Aus, the associated convection apparently has a deeper structure shown in **Figure 5.3a** such that despite its low overall magnitude compared to EQ-Ind and CP-ITCZ, it has higher values above 300 hPa. This also indicates that very-deep convection is present in NW-Aus, which can explain the high values of f_m

in NW-Aus. Shown in **Figure 5.3d**, CP-ITCZ has the highest Q_1' amplitude peak at 700 hPa, indicating that there is fractionally more shallow convection per unit precipitation in this region, which limits high cloud generation. This can explain the low values of f_m over CP-ITCZ.

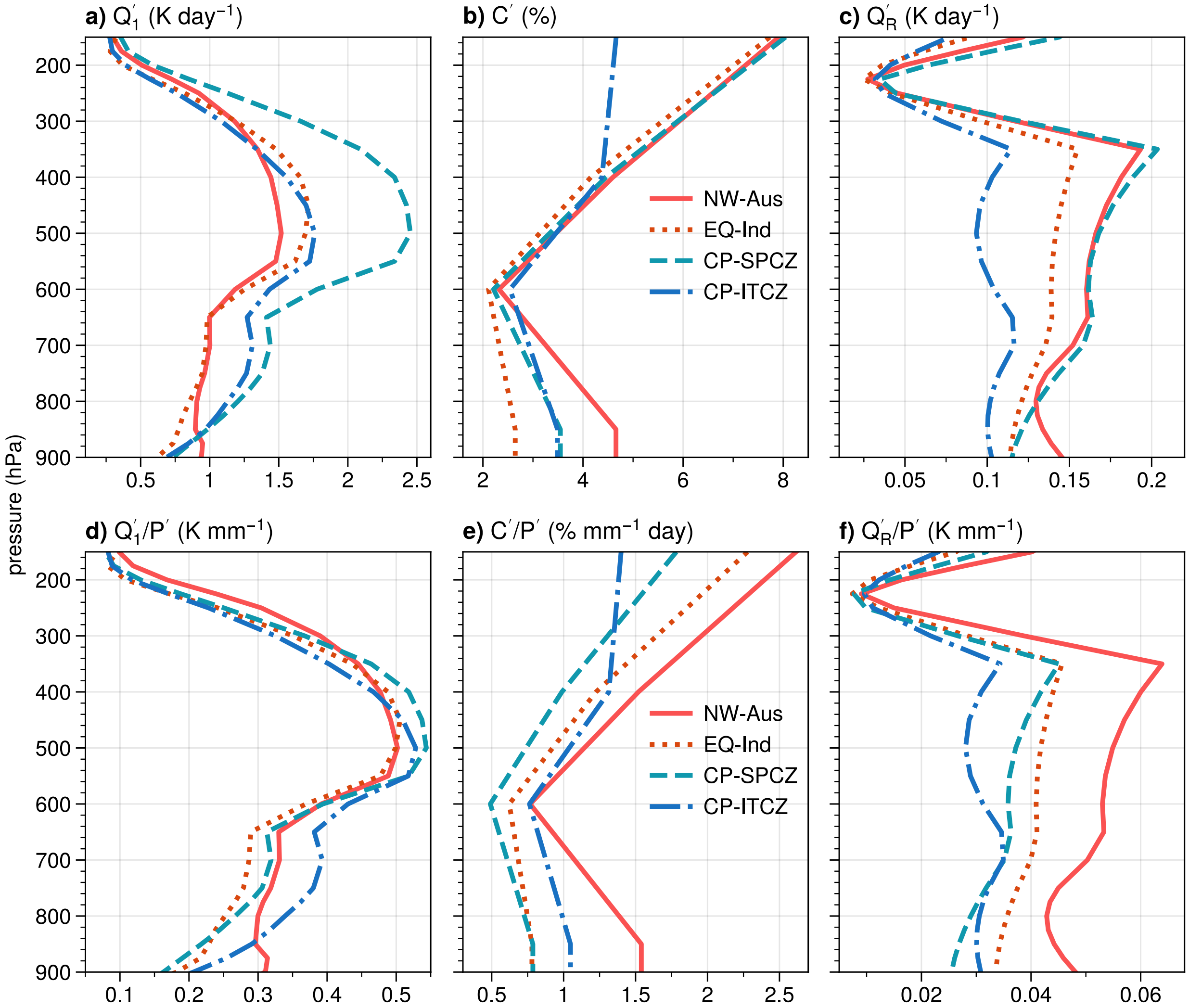

Figure 5.3. Areal-mean composite MJO amplitudes of (a) apparent heat source, Q_1', (b) cloud cover, C', and (c) LW CRE, Q_R'. (d-f) as (a-c) but divided by the areal-mean precipitation (P') amplitudes. Note that grids with land area > 90% are excluded while averaging.

Next, the vertical structure of C' amplitude is examined, with a focus on high clouds (C'_{high}; at 150 hPa). CP-ITCZ has a C'_{high} amplitude of 4.5%, much lower than around 8% found in the other three tropical regions, which is consistent with its shallower convection and very low f_m. This translates to a weak LW CRE (**Figure 5.3c**). It is interesting that EQ-Ind, CP-SPCZ, and CP-ITCZ have similar C'_high near 8% with EQ-Ind slightly lower (**Figure 5.3b**), despite having different *P*' amplitudes (**Table 5.1**). This seems to be a coincidence though, as they have different values in other temporal spectral bands such as the 2-10 day range (**Figure A5.2**). The C'_high-*P*' ratios are thus mostly determined by *P*' amplitudes in these three regions, such that NW-Aus > EQ-Ind > CP-SPCZ in the ratios (**Figure 5.3e**). Q'_R amplitude appears sensitive to C'_high amplitude, such that a 0.2% difference between EQ-Ind (C'_high amplitude = 7.73%) and NW-Aus (C'_high amplitude = 7.91%) leads to a 0.05 K day^{-1} difference at 350 hPa (**Figure 5.3c**). However, since CP-SPCZ has a very high *P*' amplitude, the normalized Q'_R amplitude becomes comparable to EQ-Ind and substantially lower than NW-Aus (**Figure 5.3f**).

5.4.3 Mesoscale organization of convection

Mesoscale organized convection consists of not only the convective area, but also a large area with upper-tropospheric stratiform clouds (Houze, 2004). After convection dissipates, these stratiform clouds attenuate and become optically thin cirrus clouds with reduced OLR, causing a net heating of the atmosphere in the form of LW CRE (Ackerman et al., 1988). Thus, compared to ordinary deep convection without mesoscale organization, mesoscale convection generates more high clouds and imposes more atmospheric LW CRE. **Chapter 2** found that higher sea surface temperature (SST) and stronger low-level wind shear magnitudes in 700-925 hPa (S_LL) helps the organization of tropical deep convection, consistent with mesoscale meteorology theories (Hsiao et al., 2024). A higher degree of mesoscale organization is associated with increasing cirrus cloud cover and LW CRE produced per unit surface precipitation, which motivates an examination of whether the distribution of favorable environments for mesoscale convective organization matches the regions with higher LW CRF in this study.

Inspired by the conditioning method in Hsiao et al. (2024) and **Chapter 2**, f_m and the C'_{high}-P' slope are calculated only using locations and days that have SST and S_{LL} lie in particular ranges, which are shown by the two-dimensional (2-D) bins in **Figure 5.4a-b**. The two quantities have similar patterns in the SST-S_{LL} phase space, in that they increase with SST, and increase with S_{LL} when SST is above 30°C. The result that f_m and the C'_{high}-P' slope increase with SST and S_{LL} is consistent with Hsiao et al. (2024), although they calculate LW CRF using monthly means and raw values instead of MJO anomalies. As f_m is higher when SST and S_{LL} are both high, we select the range of SST $\geq$ 30°C and $S_{LL} \geq 8$ m s^{-1} and plot the frequency of occurrence by location when the criteria are met to see if locations with high occurrence coincide regions with high f_m (**Figure 5.4c**). Over the east half of NW-Aus, the condition favorable for mesoscale organization frequently occurs (~10%), indicating that the high f_m in NW-Aus might be generated by more organized convection favorable to develop at this location.

The region of high frequency of occurrence of high SST and S_{LL} in NW-Aus coincides with the region where strong mesoscale organized convective systems occur associated with Indonesian-Australian monsoon (Mapes & Houze, 1992; Pope et al., 2009). These convective systems are reported to have squall-line structures, and the strong low-level wind shear plays an important role in the dynamics of these systems (Keenan & Carbone, 1992). This region does not have particularly low climatological OLR (**Figures 5.1a**), while having a high amplitude of *R*' (**Figure** 5.**1d**), suggesting a strong modulation of mesoscale systems by the MJO. Consistently, previous studies found that high precipitation in this region develop preferentially during certain phases of the MJO (Hendon & Liebmann, 1990; M. C. Wheeler & Hendon, 2004), consistent with the "Deep West Regime" of the monsoonal rainfall pattern (Pope et al., 2009). The strong LW CRF in NW-Aus is thus suggested to be associated with these monsoonal squall-line systems supported by strong low-level wind shear, of which the activity is largely modulated by MJO phases.

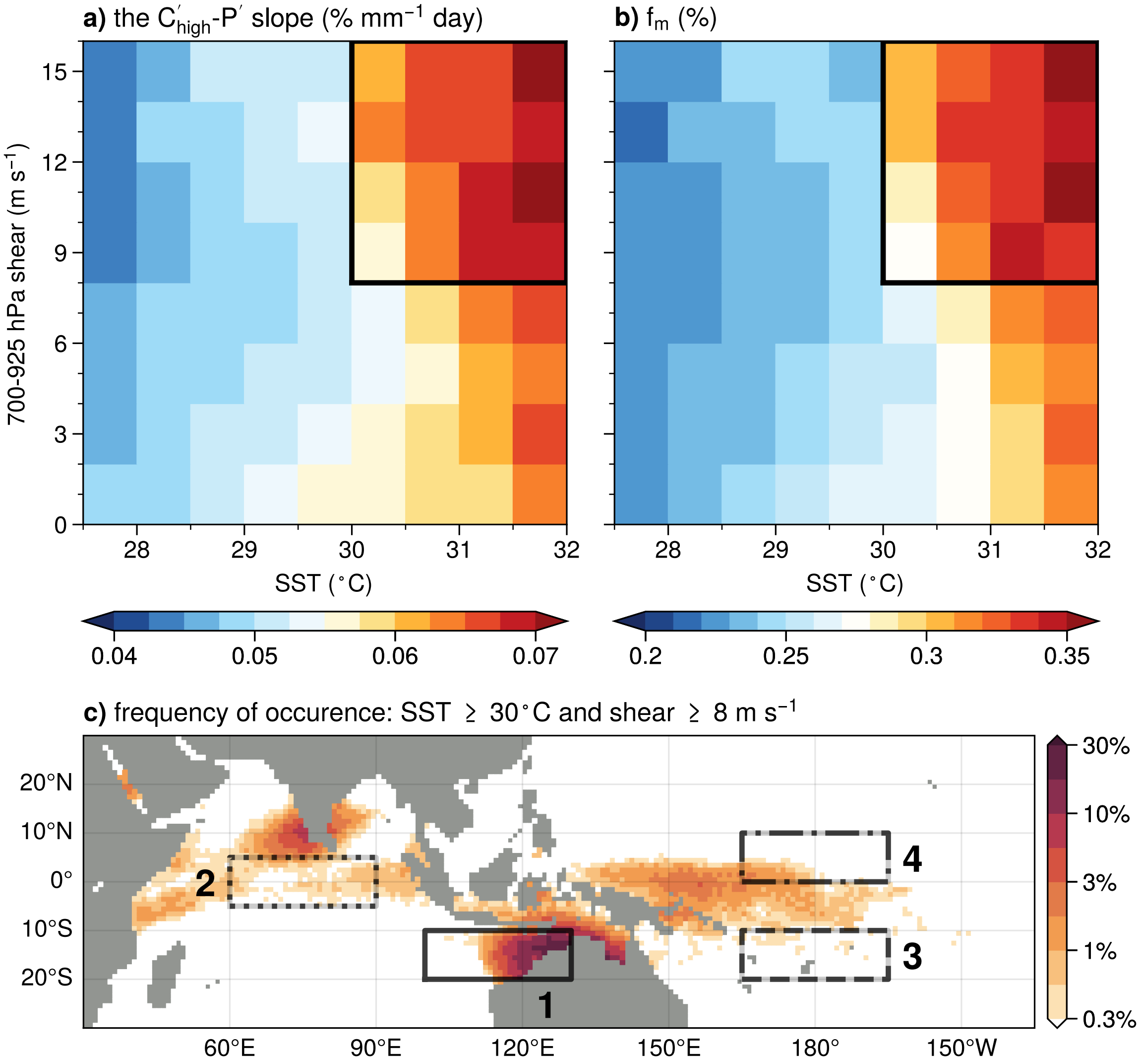

Figure 5.4. (a) The C'_{high}-P' slopes and (b) f_m calculated using data points that satisfy the 2-D bins of raw SST and 700-925 hPa low-level wind shear intensity S'_{LL}. (c) the frequency of occurrence when daily-mean SST ≥ 30°C and when $S'_{LL} \geq 8$ m s^{-1}, as the range of selection is indicated by the box in (a-b). Note that the frequency of occurrence is shown in a logarithmic color scale.

5.4.4 Different heights of ITCZ and SPCZ

As discussed in **Chapter 5.4.2**, the CP-ITCZ and CP-SPCZ regions have very different vertical structures of *C*' and Q_R' amplitudes and f_{m}, despite them being located in the central tropical Pacific at the same longitudes. CP-ITCZ has much shallower convection structure, and lower C_{high}' amplitude than the other three regions of interest, which leads to low Q_R' amplitudes and low f_{m} (**Figure 5.3**). The extended-austral summer climatology Q_R shows that the ITCZ at 180° longitude has a shallower heating with high values largely below 500 hPa with a more bottom-heavy structure, while the SPCZ has a heating that reaches to 300 hPa (**Figure 5.5a**). This is also evident in climatological cloud cover (**Figure 5.5b**), in that there is less high cloud cover near the top of troposphere but more low clouds at 5°N, compared to the profile near 10°S. Q_R' amplitude is large near 400 hPa and for *C*' amplitude at 150 hPa above the SPCZ, while both are not as apparent above the ITCZ (**Figures 5c-d**). To sum up, CP-ITCZ has the weakest LW CRF among all regions of interest because the ITCZ has convective systems that are shallower.

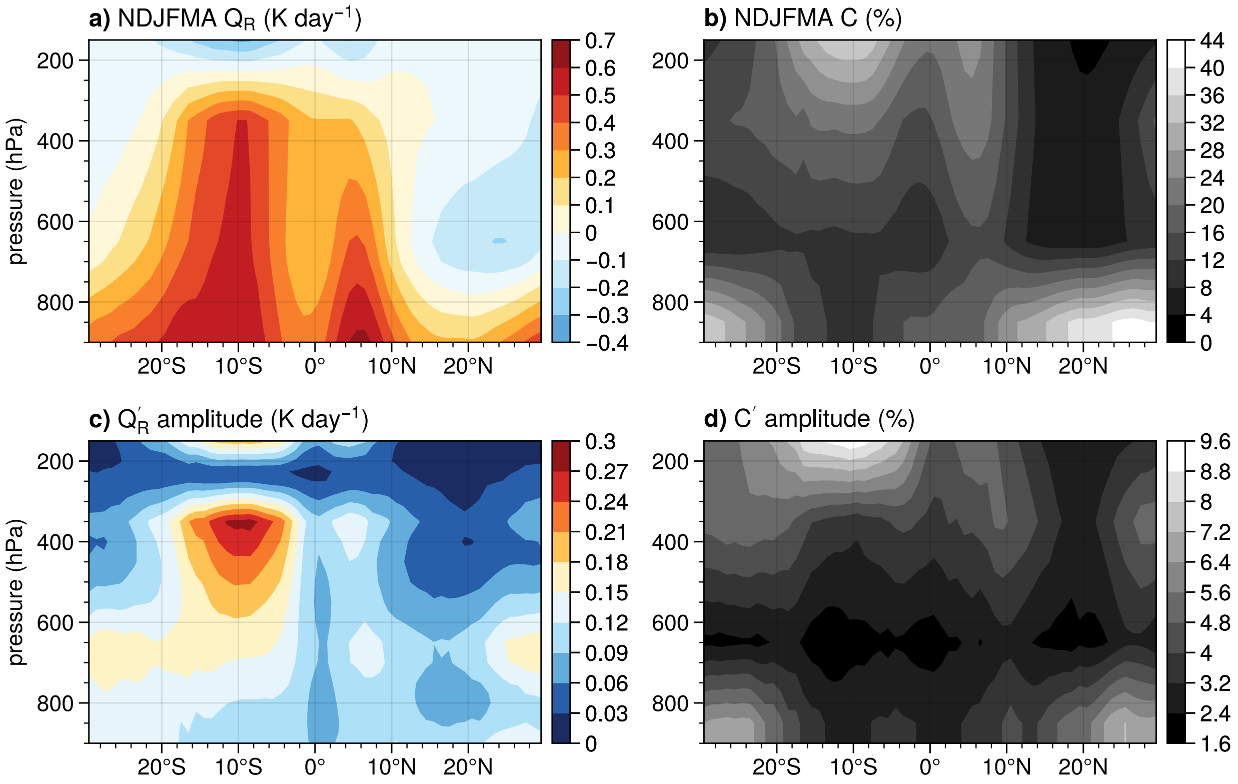

Figure 5.5. Pressure-latitude cross sections at 180° longitude: (a) climatological NDJFMA Q_R, (b) climatological NDJFMA C, (c) Q_R' amplitude, and (d) C' amplitude.

5.4.5 Precipitation efficiency

As discussed in **Chapter 5.4.2**, while CP-SPCZ and EQ-Ind have similar vertical structures of C_{high}' and Q_R' amplitudes, CP-SPCZ has weaker LW CRF due to the large *P*'. One possible mechanism could be that deep convective systems produce a similar amount of stratiform clouds in the two regions, while the ones in CP-SPCZ remove raindrops in the convective region more efficiently, making f_{m} smaller. Thus, whether spatial inhomogeneity of precipitation efficiency contributes to the spatial pattern of LW CRF deserves examination. Following Li et al. (2022), the bulk precipitation efficiency associated with 30-90-day anomalies is calculated as the linear regression slope of *P*' to the column-integrated specific humidity MJO anomaly $\langle q' \rangle_{tot}$ (**Figure 5.6a**). Note that this quantity is equivalent to the inverse of the commonly defined convective adjustment time. It is shown that CP-SPCZ does have the largest precipitation efficiency shown on the map, which leads to the smaller LW CRF in the region than in EQ-Ind. In NW-Aus, the precipitation efficiency is quite low, which could accentuate the strength of LW CRF. Why such spatial pattern of precipitation efficiency exists is not clear.

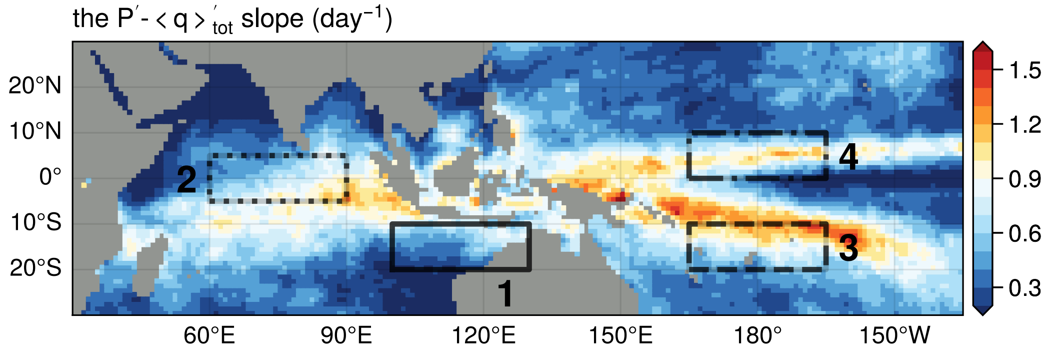

Figure 5.6. The bulk precipitation efficiency estimated as the linear regression slope of *P*’ to the 1000-150 hPa integrated specific humidity MJO anomaly $\langle q' \rangle_{tot}$.

5.4.6 Synopsis

How the factors discussed affect the LW CRF in each region is organized as in **Table 5.2**. NW-Aus has the highest f_m because it satisfies all the features discussed that aid stronger LW CRF. On the other hand, CP-ITCZ has the lowest f_m because none of the features for stronger LW CRF are satisfied.

Note that we do not exhaustively discuss all the possible factors that could impact the strength of LW CRF. For example, aerosol concentration may affect the lifetime of high clouds, which could contribute to cloud cover. These other factors are beyond the scope of this study and can be examined in future research.

Table 5.2. Features that contribute positively to stronger LW CRF. (+, o, -) denote whether the features are strongly shown, not apparent, and opposed, respectively.

	Convection is Deep	Presence of high SST and S_{LL}	Precipitation efficiency is low	f_m ranking
1. NW-Aus	+	+	+	1
2. EQ-Ind	+	o	o	2
3. CP-SPCZ	+	o	-	3
4. CP-ITCZ	-	o	o	4

5.5 Possible effects on the MJO

Possible effects on the dynamics of the MJO by the spatially inhomogeneous LW CRF are now discussed. As the MJO primarily initiates in the tropical Indian ocean (e.g., Matthews, 2008; Wang & Li, 2022), it is possible that the generally stronger LW CRF in the region compared to the tropical western Pacific helps destabilize the MJO more and boost the survival rate of the MJO in the region.

When the austral-summertime MJO propagates eastward, it commonly detours to the south and passes through the NW-Aus region (e.g., Hudson & Maloney, 2022). The strong LW CRF in NW-Aus found in this study can help strongly support the MJO with such a pathway. Echoing previous studies proposing that the southward detour of the MJO is favored by its interaction with the Indonesian-Australian monsoon (Kim et al., 2017), strong LW CRF in the monsoon region associated with stronger shear suggests that the monsoon-MJO interaction is highly relevant to the mean behavior of the MJO. Along with the barrier effect of the Maritime Continent (Ling et al., 2019), the shallow convective structure of the ITCZ and the weak LW CRF in the tropical western-to-central Pacific, the environment near the equator and to its north is less favorable for the growth of large-scale convective systems. This may help explain why the MJO is more active in the southern hemisphere during the extended austral summer despite the maximum climatological precipitation being located to the north.

In Mayta and Adames Corraliza (2023), they show that the MJO is only a “moisture mode” over the tropical Indian ocean but not in the tropical western Pacific. As LW CRF is an important destabilizing factor in moisture mode theories (Adames & Kim, 2016; Z. Fuchs & Raymond, 2005; A. Sobel & Maloney, 2013), our finding of stronger LW CRF over the tropical Indian ocean than in the tropical western Pacific suggests a possible cause.

5.6 Summary

Longwave cloud-radiative feedback (LW CRF) is an important feedback that destabilizes the austral-summertime MJO. The spatial pattern of LW CRF in the MJO is, however, overlooked although already being implied by the analyses in previous studies (**Figure 5.1**). This study assesses the spatial pattern of LW CRF in the MJO using two metrics: f_{OLR}, defined as the negative slope of intraseasonal OLR anomalies (R’) regressed onto intraseasonal precipitation anomalies (P’), and f_{m}, defined as the slope of intraseasonal free-tropospheric moistening derived under a WTG balance ($\langle \alpha Q_R \rangle'_{FT}$) regression onto P’. A rich spatial inhomogeneity is found in f_{OLR} and f_{m}, both showing a similar spatial pattern (**Figure 5.2**). The high cloud production efficiency, estimated by the slope of intraseasonal high cloud cover anomalies (C'_{high}) regressed onto P’, has a similar spatial pattern to f_{OLR} and f_{m}, implying that the variability in high cloud production efficiency causes the spatial pattern of LW CRF, consistent with radiative transfer theories.

The spatial pattern of f_{m} is examined, along with the selection of four characteristic regions where f_{m} shows prominent features (**Figure 5.2a**), with their abbreviations indicated in the parentheses as follows. The zonally extended region from Timor Sea to the Coral Sea south of

Indonesia and north of Australia (NW-Aus) has the highest $\mathrm{f_m}$. The tropical Indian ocean (EQ-Ind) has generally higher f_{m} than in the tropical Pacific. The tropical western-to-central Pacific near 180° longitude, where the climatological ITCZ is located near 5°N (CP-ITCZ), has the lowest $\mathrm{f_m}$. However, f_{m} is higher than CP-ITCZ but lower than EQ-Ind in the climatological SPCZ located near 10°S (CP-SPCZ). The area averaged f_{m} with other quantities related to LW CRF are organized in **Table 5.1**.

NW-Aus has a high frequency of occurrence of high SST over 30°C and strong low-level (700-925 hPa) wind shear ($\mathrm{S_{LL}}$) over 8 m $\mathrm{s^{-1}}$, an environment favorable for the mesoscale organization of deep convection (**Figure 5.4**). The environment associated with the Indonesian-Australian monsoon helps the development of squall line-like convective systems that produce high clouds more effectively. This likely contributes to the highest f_{m} observed over NW-Aus. The bulk precipitation efficiency estimated by the slope of P' linearly regressed onto the intraseasonal column-integrated precipitable water $\langle q' \rangle_{tot}$ has a rich spatial distribution, which also contributes to the spatial pattern of f_{m} (**Figure 5.6**). The precipitation efficiency is low over NW-Aus, which enhances the f_{m}; the efficiency is higher over CP-SPCZ than over EQ-Ind, which likely results in the higher f_{m} in EQ-Ind than the CP-SPCZ. Convection over the CP-ITCZ is found to be much shallower than over the other three regions on both climatological or intraseasonal timescales (**Figures 5.3 and 5.5**), which contributes to weak C'_{high} and the lowest f_{m} observed over the MJO active region. A synopsis of how these factors qualitatively modulate f_{m} is organized as in **Table 5.2**.

The spatial pattern of f_{m} has implications for the dynamics of the MJO. Higher f_{m} over EQ-Ind than CP-SPCZ may enhance the likelihood of the MJO initiating over the Indian ocean than in the tropical Pacific. Very high f_{m} over NW-Aus may help the propagation of the MJO southeastward through the Timor Sea prior to entering the tropical western Pacific, which may be a result of the MJO interacting with the Indonesian-Australian monsoon. Very low f_m over CP-ITCZ along with the barrier effect of the Maritime Continent makes the Northern Hemisphere hostile for intraseasonal convective systems, which partly explain why the austral-summertime MJO is more active over the Southern Hemisphere.

The present study provides an overview of how LW CRF associated with the MJO is spatially distributed using observational datasets. The findings imply that the MJO is heavily influenced by multiscale interactions, including the interactions between large-scale environments and the properties of deep convection, clouds, and the resultant atmospheric LW CRE. As models struggle to simulate realistic MJO variability, similar diagnosis can be applied in these simulations and provide a process understanding of the biases in the models. It is also of interest whether this spatial pattern of LW CRF exists for other spatiotemporal spectral bands outside of the intraseasonal timescales, or if they have different patterns. For example, the climatological ratio of OLR over P has a different spatial pattern (**Figures 5.1a-b**). The manuscript serves as a preliminary attempt to study the spatial pattern of the feedback between radiation and tropical convection, and indeed more future studies should be conducted to understand the nature and the implications of the pattern.

CHAPTER 6

Summary

The present dissertation investigates various topics related to the interaction between radiative feedbacks and tropical organized convective systems. How large-scale meteorological conditions interact with tropical mesoscale organized convection and radiative feedbacks was examined in **Chapter 2**. Sensitivity of longwave radiative feedback estimation to observational data sets of precipitation was investigated in **Chapter 3**. The three-dimensional structure of the radiative effect and how it drives circulation and moistens the MJO was studied in **Chapter 4**, and the rich horizontal spatial structure of longwave cloud-radiative feedback in the MJO was examined in **Chapter 5**. The main findings from these chapters are summarized below. And future perspectives are provided.

6.1 Main findings of this dissertation

Chapter 2 - Observed Relationships between Sea Surface Temperature, Vertical Wind Shear, Tropical Organized Deep Convection, and Radiative Effects:

Organized deep convective activity has been routinely monitored by satellite precipitation radar from the Tropical Rainfall Measuring Mission (TRMM) and Global Precipitation Mission (GPM). Organized deep convective activity is found to increase not only with sea surface temperature (SST) above 27°C, but also with low-level wind shear. Precipitation shows a similar increasing relationship with both SST and low-level wind shear, except for the highest low-level wind shear. These observations suggest that the threshold for organized deep convection and precipitation in the tropics should consider not only SST, but also vertical wind shear. The longwave cloud radiative feedback, measured as the tropospheric longwave cloud radiative heating per amount of precipitation, is found to generally increase with stronger organized deep convective activity as SST and low-level wind shear increase. Organized deep convective activity, the longwave cloud-radiative feedback, and cirrus ice cloud cover per amount of precipitation also appear to be controlled more strongly by SST than by the deviation of SST from its tropical mean. This study hints at the importance of non-thermodynamic factors such as vertical wind shear for impacting tropical convective structure, cloud properties, and associated radiative energy budget of the tropics.

This study uses tropical satellite observations to demonstrate that vertical wind shear affects the relationship between sea surface temperature and tropical organized deep convection and precipitation. Shear also affects associated cloud properties and how clouds affect the flow of radiation in the atmosphere. Although how vertical wind shear affects convective organization has long been studied in the mesoscale community, the study attempts to apply mesoscale theory to explain the large-scale mean organization of tropical deep convection, cloud properties, and radiative feedbacks. The study also provides a quantitative observational baseline of how vertical wind shear modifies cloud radiative effects and convective organization, which can be compared to numerical simulations.

Chapter 3 - The Longwave Cloud-Radiative Feedback in Tropical Waves Derived by Different Precipitation Data Sets:

Anomalous tropical longwave cloud-radiative heating of the atmosphere is generated when convective precipitation occurs, which plays an important role in the dynamics of tropical disturbances. Defining the observed cloud-radiative feedback as the reduction of top-of-atmosphere longwave radiative cooling per unit precipitation, the feedback magnitudes are sensitive to the observed precipitation data set used when comparing two versions of Global Precipitation Climatology Project, version 1.3 (GPCPv1.3) and the newer version 3.2 (GPCPv3.2). GPCPv3.2 contains larger magnitudes and variance of daily precipitation, which yields a weaker cloud-radiative feedback in tropical disturbances at all frequencies and zonal wavenumbers. Weaker cloud-radiative feedbacks occur in GPCPv3.2 at shorter zonal lengths on intraseasonal timescales, which implies a preferential growth at planetary scales for the Madden-Julian oscillation. Phase relationships between precipitation, radiative heating, and other thermodynamic variables in eastward-propagating gravity waves also change with the updated GPCPv3.2.

Chapter 4 - Three-dimensional structure of radiative effect in the observed Madden-Julian oscillation:

Three-dimensional structure of radiative heating in the boreal-winter MJO is examined using spaceborne satellite-derived radiative fluxes. A weak-temperature-gradient (WTG) framework is used to diagnose the moistening of the MJO by the radiatively driven vertical advection. Upward motion driven by the longwave cloud radiative effect dominantly moistens regions near the MJO convective center, although bottom-heavy clear-sky longwave radiative heating enhances the magnitude and the efficiency of the moistening per unit column heating. Despite a near-zero column integrated shortwave radiative heating, the WTG framework indicates that shortwave feedbacks dry the atmosphere near the MJO convective center by inducing downward motion at lower levels. The anomalous MJO horizontal circulation coupled to the radiative heating structure is also inferred by simulations in a linear baroclinic model. Behind the MJO center, total radiative heating drives confluent meridional flow advecting drier air and enhances westerlies strengthening drying caused by synoptic disturbances, both of which may contribute to the propagation of the MJO. Inspecting individual amplifying MJO events show that they cannot grow without radiative feedback for over 90% of the days. The study provides a more complete diagnosis of the maintenance and the propagation of the MJO moisture field contributed not only by the direct effects of radiative heating, but also the indirect effects induced by the three-dimensional circulation driven by the radiative heating.

Chapter 5 - Spatially inhomogeneous longwave cloud-radiative-convective feedback in tropical intraseasonal variability:

Tropical longwave-cloud-radiative feedback on intraseasonal timescales (LW CRF) is quantified as either using the negative outgoing longwave radiation anomaly or the moistening anomaly induced by atmospheric longwave-cloud-radiative heating under the weak-temperature-gradient balance produced per unit surface precipitation anomaly. The austral summertime LW CRF has a rich horizontal spatial structure: it is very strong over the oceanic regions to the northwest of Australia; it is generally stronger in the tropical Indian ocean than in the tropical western-to-central Pacific; it is very weak over the tropical central Pacific where the climatological intertropical convergence zone (ITCZ) is located. The spatial structure shows correspondence with the pattern of high cloud production efficiency per unit surface precipitation. Strong low-level wind shear associated with the Indonesian-Australian monsoon and high sea surface temperatures likely help the mesoscale organization of convection to the northwest of Australia, causing the strong LW CRF. The tropical western-to-central Pacific has higher precipitation efficiency than the tropical Indian ocean, causing the generally weaker LW CRF. The central-Pacific climatological ITCZ consists of convection much shallower than other tropical warm-pool regions, causing weak high cloud production efficiency and weak LW CRF. The spatial pattern of LW CRF may partly explain why the austral-summer Madden-Julian oscillation likely initiates over the Indian ocean and propagates southeastward prior to entering the Pacific ocean.

6.2 Future outlook

As the present dissertation attempts to investigate tropical organized deep convection in observations, the resolution of data sets is not sufficient to comprehensively examine physical processes on convective scales. For example, **Chapter 2** found a robust positive relationship between tropical organized convective activity and low-level wind shear strength. But how the shear actually helps the organization of convection, for example, whether the RKW theory is followed (Rotunno et al., 1988), is unresolved in the available data sets. Use of higher-resolution data sets from observations is thus desired in future research to provide a better understanding of the drivers of tropical convective organization. An example would be utilizing geostationary satellite observations to track the evolution of mesoscale convective systems (Feng et al., 2021) with their associated radiative properties, and to examine how large-scale meteorological environments interact with them. These kinds of analyses would also help explain the spatial pattern of radiative feedbacks as shown in **Chapter 5**, when the statistics of the life cycles and the structures of convective systems at different locations can be obtained.

Studies conducted in the dissertation use data over 2000s-2020s in a similar climatological state, without considering the changing global climate. How the radiative feedbacks in tropical organized convective systems drift over time or vary with long-term climate variability is a topic worth investigating in the future. For example, the WTG balance suggests that when the tropical troposphere becomes more stable under global warming, the circulation as well as convective detrainment would be weakened per unit precipitation (e.g., Hsiao et al., 2020), and we might expect less high cloudiness produced by convection. This implies that feedbacks destabilizing the MJO could contribute to MJO growth differently as global climate changes. As tropical organized convective systems impact human livelihoods over the globe, examining how the findings in this dissertation fluctuate with long-term climate variability would be valuable.

REFERENCES

Abbot, D. S. (2014). Resolved Snowball Earth Clouds. *Journal of Climate*, *27*(12), 4391–4402.

Ackerman, T. P., Liou, K.-N., Valero, F. P. J., & Pfister, L. (1988). Heating Rates in Tropical Anvils. *Journal of the Atmospheric Sciences*, *45*(10), 1606–1623.

Adames, Á. F., & Kim, D. (2016). The MJO as a Dispersive, Convectively Coupled Moisture Wave: Theory and Observations. *Journal of the Atmospheric Sciences*, *73*(3), 913–941.

Adames, Á. F., & Maloney, E. D. (2021). Moisture mode theory's contribution to advances in our understanding of the madden-Julian oscillation and other tropical disturbances. *Current Climate Change Reports*, *7*(2), 72–85.

Adames, Á. F., & Wallace, J. M. (2014). Three-Dimensional Structure and Evolution of the MJO and Its Relation to the Mean Flow. *Journal of the Atmospheric Sciences*, *71*(6), 2007–2026.

Adames, Á. F., & Wallace, J. M. (2015). Three-Dimensional Structure and Evolution of the Moisture Field in the MJO. *Journal of the Atmospheric Sciences*, *72*(10), 3733–3754.

Adames, Á. F., Kim, D., Clark, S. K., Ming, Y., & Inoue, K. (2019). Scale Analysis of Moist Thermodynamics in a Simple Model and the Relationship between Moisture Modes and Gravity Waves. *Journal of the Atmospheric Sciences*, *76*(12), 3863–3881.

Adler, R. F., Sapiano, M., Huffman, G. J., Wang, J., Gu, G., Bolvin, D., et al. (2018). The Global Precipitation Climatology Project (GPCP) Monthly Analysis (New Version 2.3) and a Review of 2017 Global Precipitation. *Atmosphere*, *9*(4). https://doi.org/10.3390/atmos9040138

Alfaro, D. A. (2017). Low-Tropospheric Shear in the Structure of Squall Lines: Impacts on Latent Heating under Layer-Lifting Ascent. *Journal of the Atmospheric Sciences*, *74*(1), 229–248.

Andersen, J. A., & Kuang, Z. (2012). Moist Static Energy Budget of MJO-like Disturbances in the Atmosphere of a Zonally Symmetric Aquaplanet. *Journal of Climate*, *25*(8), 2782–2804.

Angulo-Umana, P., & Kim, D. (2023). Mesoscale convective clustering enhances tropical precipitation. *Science Advances*, *9*(2), eabo5317.

Arnold, N. P., Branson, M., Kuang, Z., Randall, D. A., & Tziperman, E. (2015). MJO Intensification with Warming in the Superparameterized CESM. *Journal of Climate*, *28*(7), 2706–2724.

Barnes, H. C., & Houze, R. A., Jr. (2013). The precipitating cloud population of the Madden-Julian Oscillation over the Indian and west Pacific Oceans. *Journal of Geophysical Research*, *118*(13), 6996–7023.

Benedict, J. J., Medeiros, B., Clement, A. C., & Olson, J. G. (2020). Investigating the role of cloud-radiation interactions in subseasonal tropical disturbances. *Geophysical Research Letters*, *47*(9), e2019GL086817.

Bergemann, M., & Jakob, C. (2016). How important is tropospheric humidity for coastal rainfall in the tropics? *Geophysical Research Letters*, *43*(11), 5860–5868.

Bolvin, D. T., Huffman, G. J., Nelkin, E. J., & Tan, J. (2021). Comparison of Monthly IMERG Precipitation Estimates with PACRAIN Atoll Observations. *Journal of Hydrometeorology*, *22*(7), 1745–1753.

Bony, S., Stevens, B., Frierson, D. M. W., Jakob, C., Kageyama, M., Pincus, R., et al. (2015). Clouds, circulation and climate sensitivity. *Nature Geoscience*, *8*(4), 261–268.

Bony, S., Stevens, B., Coppin, D., Becker, T., Reed, K. A., Voigt, A., & Medeiros, B. (2016). Thermodynamic control of anvil cloud amount. *Proceedings of the National Academy of Sciences of the United States of America*, *113*(32), 8927–8932.

Bony, S., Semie, A., Kramer, R. J., Soden, B., Tompkins, A. M., & Emanuel, K. A. (2020). Observed modulation of the tropical radiation budget by deep convective organization and lower-tropospheric stability. *AGU Advances*, *1*(3). https://doi.org/10.1029/2019av000155

Bretherton, C. S., & Sobel, A. H. (2002). A Simple Model of a Convectively Coupled Walker Circulation Using the Weak Temperature Gradient Approximation. *Journal of Climate*, *15*(20), 2907–2920.

Bretherton, C. S., Peters, M. E., & Back, L. E. (2004). Relationships between Water Vapor Path and Precipitation over the Tropical Oceans. *Journal of Climate*, *17*(7), 1517–1528.

Bretherton, C. S., Blossey, P. N., & Khairoutdinov, M. (2005). An Energy-Balance Analysis of Deep Convective Self-Aggregation above Uniform SST. *Journal of the Atmospheric Sciences*, *62*(12), 4273–4292.

Chen, P.-J., Chen, W.-T., Wu, C.-M., & Yo, T.-S. (2021). Convective cloud regimes from a classification of object-based CloudSat observations over Asian-Australian monsoon areas. *Geophysical Research Letters*, *48*(10). https://doi.org/10.1029/2021gl092733

Chikira, M. (2014). Eastward-Propagating Intraseasonal Oscillation Represented by Chikira–Sugiyama Cumulus Parameterization. Part II: Understanding Moisture Variation under Weak Temperature Gradient Balance. *Journal of the Atmospheric Sciences*, *71*(2), 615–639.

Ciesielski, P. E., Johnson, R. H., Jiang, X., Zhang, Y., & Xie, S. (2017). Relationships between radiation, clouds, and convection during DYNAMO. *Journal of Geophysical Research, D: Atmospheres*, *122*(5), 2529–2548.

Cifelli, R., Chandrasekar, V., Lim, S., Kennedy, P. C., Wang, Y., & Rutledge, S. A. (2011). A New Dual-Polarization Radar Rainfall Algorithm: Application in Colorado Precipitation Events. *Journal of Atmospheric and Oceanic Technology*, *28*(3), 352–364.

Coppin, D., & Bony, S. (2015). Physical mechanisms controlling the initiation of convective self-aggregation in a General Circulation Model. *Journal of Advances in Modeling Earth Systems*, *7*(4), 2060–2078.

Crueger, T., & Stevens, B. (2015). The effect of atmospheric radiative heating by clouds on the Madden-Julian Oscillation. *Journal of Advances in Modeling Earth Systems*, *7*(2), 854–864.

Del Genio, A. D., & Chen, Y. (2015). Cloud-radiative driving of the Madden-Julian oscillation as seen by the A-Train. *Journal of Geophysical Research, D: Atmospheres*, *120*(11), 5344–5356.

Di Giuseppe, F., & Tompkins, A. M. (2015). Generalizing Cloud Overlap Treatment to Include the Effect of Wind Shear. *Journal of the Atmospheric Sciences*, *72*(8), 2865–2876.

Doelling, D. R., Loeb, N. G., Keyes, D. F., Nordeen, M. L., Morstad, D., Nguyen, C., et al. (2013). Geostationary Enhanced Temporal Interpolation for CERES Flux Products. *Journal of Atmospheric and Oceanic Technology*, *30*(6), 1072–1090.

Doelling, D. R., Sun, M., Nguyen, L. T., Nordeen, M. L., Haney, C. O., Keyes, D. F., & Mlynczak, P. E. (2016). Advances in Geostationary-Derived Longwave Fluxes for the CERES Synoptic (SYN1deg) Product. *Journal of Atmospheric and Oceanic Technology*, *33*(3), 503–521.

Elsaesser, G. S., & Kummerow, C. D. (2013). A Multisensor Observational Depiction of the Transition from Light to Heavy Rainfall on Subdaily Time Scales. *Journal of the Atmospheric Sciences*, *70*(7), 2309–2324.

Elsaesser, G. S., Kummerow, C. D., L'Ecuyer, T. S., Takayabu, Y. N., & Shige, S. (2010). Observed Self-Similarity of Precipitation Regimes over the Tropical Oceans. *Journal of Climate*, *23*(10), 2686–2698.

Emanuel, K. (2018). 100 years of progress in tropical cyclone research. *Meteorological Monographs*, *59*. https://doi.org/10.1175/AMSMONOGRAPHS-D-18-0016.1

Emanuel, Kerry, Wing, A. A., & Vincent, E. M. (2014). Radiative-convective instability. *Journal of Advances in Modeling Earth Systems*, *6*(1), 75–90.

Feng, Z., McFarlane, S. A., Schumacher, C., Ellis, S., Comstock, J., & Bharadwaj, N. (2014). Constructing a Merged Cloud–Precipitation Radar Dataset for Tropical Convective

Clouds during the DYNAMO/AMIE Experiment at Addu Atoll. *Journal of Atmospheric and Oceanic Technology*, *31*(5), 1021–1042.

Feng, Z., Leung, L. R., Liu, N., Wang, J., Houze, R. A., Jr, Li, J., et al. (2021). A global high-resolution mesoscale convective system database using satellite-derived cloud tops, surface precipitation, and tracking. *Journal of Geophysical Research*, *126*(8). https://doi.org/10.1029/2020jd034202

Ferrett, S., Yang, G.-Y., Woolnough, S. J., Methven, J., Hodges, K., & Holloway, C. E. (2020). Linking extreme precipitation in Southeast Asia to equatorial waves. *Quarterly Journal of the Royal Meteorological Society*, *146*(727), 665–684.

Fildier, B., Muller, C., Pincus, R., & Fueglistaler, S. (2023). How moisture shapes low-level radiative cooling in subsidence regimes. *AGU Advances*, *4*(3), e2023AV000880.

Frank, W. M., & Roundy, P. E. (2006). The Role of Tropical Waves in Tropical Cyclogenesis. *Monthly Weather Review*, *134*(9), 2397–2417.

Fuchs, Ž., & Raymond, D. J. (2002). Large-Scale Modes of a Nonrotating Atmosphere with Water Vapor and Cloud–Radiation Feedbacks. *Journal of the Atmospheric Sciences*, *59*(10), 1669–1679.

Fuchs, Z., & Raymond, D. J. (2005). Large-Scale Modes in a Rotating Atmosphere with Radiative–Convective Instability and WISHE. *Journal of the Atmospheric Sciences*, *62*(11), 4084–4094.

Fuchs, Ž., Sessions, S. L., & Raymond, D. J. (2014). Mechanisms controlling the onset of simulated convectively coupled Kelvin waves. *Tellus. Series A, Dynamic Meteorology and Oceanography*, *66*(1), 22107.

Gadgil, S., Joseph, P. V., & Joshi, N. V. (1984). Ocean–atmosphere coupling over monsoon regions. *Nature*, *312*(5990), 141–143.

Gamache, J. F., & Houze, R. A., Jr. (1983). Water budget of a mesoscale convective system in the tropics. *Journal of the Atmospheric Sciences*, *40*(7), 1835–1850.

Gill, A. E. (1980). Some simple solutions for heat-induced tropical circulation. *Quarterly Journal of the Royal Meteorological Society*, *106*(449), 447–462.

Graham, N. E., & Barnett, T. P. (1987). Sea Surface Temperature, Surface Wind Divergence, and Convection over Tropical Oceans. *Science*, *238*(4827), 657–659.

Hayashi, Y. (1971). A Generalized Method of Resolving Disturbances into Progressive and Retrogressive Waves by Space Fourier and Time Cross-Spectral Analyses. *Journal of the Meteorological Society of Japan. Ser. II*, *49*(2), 125–128.

Held, I. M., & Soden, B. J. (2006). Robust Responses of the Hydrological Cycle to Global Warming. *Journal of Climate*, *19*(21), 5686–5699.

Hendon, H. H., & Liebmann, B. (1990). The Intraseasonal (30–50 day) Oscillation of the Australian Summer Monsoon. *Journal of the Atmospheric Sciences*, *47*(24), 2909–2924.

Hersbach, H., Bell, B., Berrisford, P., Hirahara, S., Horányi, A., Muñoz-Sabater, J., et al. (2020). The ERA5 global reanalysis. *Quarterly Journal of the Royal Meteorological Society*, *64*, 29.

Hou, A. Y., Kakar, R. K., Neeck, S., Azarbarzin, A. A., Kummerow, C. D., Kojima, M., et al. (2014). The Global Precipitation Measurement Mission. *Bulletin of the American Meteorological Society*, *95*(5), 701–722.

Houze, R. A. (1989). Observed structure of mesoscale convective systems and implications for large-scale heating. *Quarterly Journal of the Royal Meteorological Society*, *115*(487), 425–461.

Houze, R. A., Jr. (2004). Mesoscale convective systems. *Reviews of Geophysics* , *42*(4). https://doi.org/10.1029/2004RG000150

Houze, R. A., Jr, Rasmussen, K. L., Zuluaga, M. D., & Brodzik, S. R. (2015). The variable nature of convection in the tropics and subtropics: A legacy of 16 years of the Tropical Rainfall Measuring Mission satellite. *Reviews of Geophysics* , *53*(3), 994–1021.

Hoyos, C. D., & Webster, P. J. (2012). Evolution and modulation of tropical heating from the last glacial maximum through the twenty-first century. *Climate Dynamics*, *38*(7), 1501–1519.

Hsiao, W.-T., & Maloney, E. D. (2024). The Longwave Cloud-Radiative Feedback in Tropical Waves Derived by Different Precipitation Data Sets. *Geophysical Research Letters*, *51*(11), e2024GL109143.

Hsiao, W.-T., Maloney, E. D., & Barnes, E. A. (2020). Investigating Recent Changes in MJO Precipitation and Circulation in Multiple Reanalyses. *Geophysical Research Letters*, *47*(22), e2020GL090139.

Hsiao, W.-T., Barnes, E. A., Maloney, E. D., Tulich, S. N., Dias, J., & Kiladis, G. N. (2022). Role of the tropics in state-dependent improvements of US west coast NOAA unified forecast system precipitation forecasts. *Geophysical Research Letters*, *49*(5). https://doi.org/10.1029/2021gl096447

Hsiao, W.-T., Hwang, Y.-T., Chen, Y.-J., & Kang, S. M. (2022). The role of clouds in shaping tropical pacific response pattern to extratropical thermal forcing. *Geophysical Research Letters*, *49*(11). https://doi.org/10.1029/2022gl098023

Hsiao, W.-T., Maloney, E. D., Leitmann-Niimi, N. M., & Kummerow, C. D. (2024). Observed Relationships between Sea Surface Temperature, Vertical Wind Shear, Tropical Organized Deep Convection, and Radiative Effects. *Journal of Climate*, *37*(4), 1277–1293.

Hu, Q., & Randall, D. A. (1994). Low-Frequency Oscillations in Radiative-Convective Systems. *Journal of the Atmospheric Sciences*, *51*(8), 1089–1099.

Hudson, J., & Maloney, E. (2022). The Role of Surface Fluxes in MJO Propagation Through the Maritime Continent. *Journal of Climate*, *1*(aop), 1–41.

Huffman, G. J., Adler, R. F., Morrissey, M. M., Bolvin, D. T., Curtis, S., Joyce, R., et al. (2001). Global Precipitation at One-Degree Daily Resolution from Multisatellite Observations. *Journal of Hydrometeorology*, *2*(1), 36–50.

Huffman, G. J., Adler, R. F., Behrangi, A., Bolvin, D. T., Nelkin, E. J., & Ehsani, M. R. (2023). *Algorithm Theoretical Basis Document (ATBD) for global precipitation climatology project version 3.2 precipitation data*. MEaSUREs project, Greenbelt, MD. Retrieved from https://docserver.gesdisc.eosdis.nasa.gov/public/project/MEaSUREs/GPCP/GPCP_ATBD_V3.2_Daily.pdf

Igel, M. R., Drager, A. J., & van den Heever, S. C. (2014). A CloudSat cloud object partitioning technique and assessment and integration of deep convective anvil sensitivities to sea surface temperature. *Journal of Geophysical Research*, *119*(17), 10515–10535.

Inoue, K., & Back, L. (2015). Column-Integrated Moist Static Energy Budget Analysis on Various Time Scales during TOGA COARE. *Journal of the Atmospheric Sciences*, *72*(5), 1856–1871.

Inoue, K., Adames, Á. F., & Yasunaga, K. (2020). Vertical Velocity Profiles in Convectively Coupled Equatorial Waves and MJO: New Diagnoses of Vertical Velocity Profiles in the Wavenumber–Frequency Domain. *Journal of the Atmospheric Sciences*, *77*(6), 2139–2162.

Jakob, C., Singh, M. S., & Jungandreas, L. (2019). Radiative convective equilibrium and organized convection: An observational perspective. *Journal of Geophysical Research*, *124*(10), 5418–5430.

Janiga, M. A., & Zhang, C. (2016). MJO Moisture Budget during DYNAMO in a Cloud-Resolving Model. *Journal of the Atmospheric Sciences*, *73*(6), 2257–2278.

Jiang, X., Adames, Á. F., Kim, D., Maloney, E. D., Lin, H., Kim, H., et al. (2020). Fifty years of research on the madden-Julian oscillation: Recent progress, challenges, and perspectives. *Journal of Geophysical Research*, *125*(17), e2019JD030911.

Johnson, N. C., & Xie, S.-P. (2010). Changes in the sea surface temperature threshold for tropical convection. *Nature Geoscience*, *3*(12), 842–845.

Johnson, R. H., & Ciesielski, P. E. (2000). Rainfall and Radiative Heating Rates from TOGA COARE Atmospheric Budgets. *Journal of the Atmospheric Sciences*, *57*(10), 1497–1514.

Johnson, R. H., Rickenbach, T. M., Rutledge, S. A., Ciesielski, P. E., & Schubert, W. H. (1999). Trimodal Characteristics of Tropical Convection. *Journal of Climate*, *12*(8), 2397–2418.

Johnson, R. H., Ciesielski, P. E., Ruppert, J. H., & Katsumata, M. (2015). Sounding-Based Thermodynamic Budgets for DYNAMO. *Journal of the Atmospheric Sciences*, *72*(2), 598–622.

Keeler, R. J., Lutz, J., & Vivekanandan, J. (2000). S-Pol: NCAR's polarimetric Doppler research radar. In *IGARSS 2000. IEEE 2000 International Geoscience and Remote Sensing Symposium. Taking the Pulse of the Planet: The Role of Remote Sensing in Managing the Environment. Proceedings (Cat. No.00CH37120)* (Vol. 4, pp. 1570–1573 vol.4). IEEE.

Keenan, T. D., & Carbone, R. E. (1992). A preliminary morphology of precipitation systems in tropical northern Australia. *Quarterly Journal of the Royal Meteorological Society. Royal Meteorological Society (Great Britain)*, *118*(504), 283–326.

Kiladis, G. N., Wheeler, M. C., Haertel, P. T., Straub, K. H., & Roundy, P. E. (2009). Convectively coupled equatorial waves. *Reviews of Geophysics* , *47*(2). https://doi.org/10.1029/2008rg000266

Kiladis, G. N., Dias, J., Straub, K. H., Wheeler, M. C., Tulich, S. N., Kikuchi, K., et al. (2014). A Comparison of OLR and Circulation-Based Indices for Tracking the MJO. *Monthly Weather Review*, *142*(5), 1697–1715.

Kim, D., Ahn, M.-S., Kang, I.-S., & Del Genio, A. D. (2015). Role of Longwave Cloud–Radiation Feedback in the Simulation of the Madden–Julian Oscillation. *Journal of Climate*, *28*(17), 6979–6994.

Kim, D., Kim, H., & Lee, M.-I. (2017). Why does the MJO detour the Maritime Continent during austral summer? *Geophysical Research Letters*, *44*(5), 2579–2587.

Knutson, T. R., & Manabe, S. (1995). Time-Mean Response over the Tropical Pacific to Increased C02 in a Coupled Ocean-Atmosphere Model. *Journal of Climate*, *8*(9), 2181–2199.

Kummerow, C., Barnes, W., Kozu, T., Shiue, J., & Simpson, J. (1998). The Tropical Rainfall Measuring Mission (TRMM) Sensor Package. *Journal of Atmospheric and Oceanic Technology*, *15*(3), 809–817.

Laing, A. G., & Fritsch, J. M. (2000). The Large-Scale Environments of the Global Populations of Mesoscale Convective Complexes. *Monthly Weather Review*, *128*(8), 2756–2776.

Landu, K., & Maloney, E. D. (2011). Effect of SST Distribution and Radiative Feedbacks on the Simulation of Intraseasonal Variability in an Aquaplanet GCM. *Journal of the Meteorological Society of Japan. Ser. II*, *89*(3), 195–210.

Lau, K.-M., Wu, H.-T., & Bony, S. (1997). The Role of Large-Scale Atmospheric Circulation in the Relationship between Tropical Convection and Sea Surface Temperature. *Journal of Climate*, *10*(3), 381–392.

Lee, H.-T., Gruber, A., Ellingson, R. G., & Laszlo, I. (2007). Development of the HIRS Outgoing Longwave Radiation Climate Dataset. *Journal of Atmospheric and Oceanic Technology*, *24*(12), 2029–2047.

Lee, M.-I., Kang, I.-S., Kim, J.-K., & Mapes, B. E. (2001). Influence of cloud-radiation interaction on simulating tropical intraseasonal oscillation with an atmospheric general circulation model. *Journal of Geophysical Research*, *106*(D13), 14219–14233.

Lee, S., L'Heureux, M., Wittenberg, A. T., Seager, R., O'Gorman, P. A., & Johnson, N. C. (2022). On the future zonal contrasts of equatorial Pacific climate: Perspectives from Observations, Simulations, and Theories. *Npj Climate and Atmospheric Science*, *5*(1). https://doi.org/10.1038/s41612-022-00301-2

Li, R. L., Studholme, J. H. P., Fedorov, A. V., & Storelvmo, T. (2022). Precipitation efficiency constraint on climate change. *Nature Climate Change*, *12*(7), 642–648.

Li, T., Wang, L., Peng, M., Wang, B., Zhang, C., Lau, W., & Kuo, H.-C. (2018). A Paper on the Tropical Intraseasonal Oscillation Published in 1963 in a Chinese Journal. *Bulletin of the American Meteorological Society*, *99*(9), 1765–1779.

Li, Z., Thompson, E. J., Behrangi, A., Chen, H., & Yang, J. (2023). Performance of GPCP Daily Products Over Oceans: Evaluation Using Passive Aquatic Listeners. *Geophysical Research Letters*, *50*(11), e2023GL104310.

Liebmann, B., & Smith, C. A. (1996). Description of a Complete (Interpolated) Outgoing Longwave Radiation Dataset. *Bulletin of the American Meteorological Society*, *77*(6), 1275–1277.

Lin, J.-L., & Mapes, B. (2004a). Wind shear effects on cloud-radiation feedback in the western Pacific warm pool. *Geophysical Research Letters*, *31*(16). https://doi.org/10.1029/2004GL020199

Lin, J.-L., & Mapes, B. E. (2004b). Radiation Budget of the Tropical Intraseasonal Oscillation. *Journal of the Atmospheric Sciences*, *61*(16), 2050–2062.

Lin, X., & Johnson, R. H. (1996). Kinematic and thermodynamic characteristics of the flow over the western pacific warm pool during TOGA COARE. *Journal of the Atmospheric Sciences*, *53*(5), 695–715.

Lindzen, R. S., & Nigam, S. (1987). On the Role of Sea Surface Temperature Gradients in Forcing Low-Level Winds and Convergence in the Tropics. *Journal of the Atmospheric Sciences*, *44*(17), 2418–2436.

Ling, J., Zhang, C., Joyce, R., Xie, P., & Chen, G. (2019). Possible Role of the Diurnal Cycle in Land Convection in the Barrier Effect on the MJO by the Maritime Continent. *Geophysical Research Letters*, *46*(5), 3001–3011.

Loeb, N. G., Doelling, D. R., Wang, H., Su, W., Nguyen, C., Corbett, J. G., et al. (2018). Clouds and the Earth's Radiant Energy System (CERES) Energy Balanced and Filled (EBAF) top-of-atmosphere (TOA) Edition-4.0 data product. *Journal of Climate*, *31*(2), 895–918.

Ma, D., & Kuang, Z. (2011). Modulation of radiative heating by the Madden-Julian Oscillation and convectively coupled Kelvin waves as observed by CloudSat. *Geophysical Research Letters*, *38*(21). https://doi.org/10.1029/2011gl049734

Madden, R. A., & Julian, P. R. (1971). Detection of a 40–50 Day Oscillation in the Zonal Wind in the Tropical Pacific. *Journal of the Atmospheric Sciences*, *28*(5), 702–708.

Madden, R. A., & Julian, P. R. (1972). Description of global-scale circulation cells in the tropics with a 40--50 day period. *Journal of the Atmospheric Sciences*, *29*(6), 1109–1123.

Maloney, E. D. (2009). The Moist Static Energy Budget of a Composite Tropical Intraseasonal Oscillation in a Climate Model. *Journal of Climate*, *22*(3), 711–729.

Maloney, E. D., & Hartmann, D. L. (1998). Frictional Moisture Convergence in a Composite Life Cycle of the Madden–Julian Oscillation. *Journal of Climate*, *11*(9), 2387–2403.

Maloney, E. D., & Hartmann, D. L. (2000). Modulation of Eastern North Pacific Hurricanes by the Madden–Julian Oscillation. *Journal of Climate*, *13*(9), 1451–1460.

Maloney, E. D., & Sobel, A. H. (2004). Surface Fluxes and Ocean Coupling in the Tropical Intraseasonal Oscillation. *Journal of Climate*, *17*(22), 4368–4386.

Mapes, B., & Houze, R. A., Jr. (1992). An integrated view of the 1987 Australian monsoon and its mesoscale convective systems. I: Horizontal structure. *Quarterly Journal of the Royal Meteorological Society. Royal Meteorological Society (Great Britain)*, *118*(507), 927–963.

Mapes, B., Tulich, S., Lin, J., & Zuidema, P. (2006). The mesoscale convection life cycle: Building block or prototype for large-scale tropical waves? *Dynamics of Atmospheres and Oceans*, *42*(1), 3–29.

Matthews, A. J. (2008). Primary and successive events in the Madden–Julian Oscillation. *Quarterly Journal of the Royal Meteorological Society. Royal Meteorological Society (Great Britain)*, *134*(631), 439–453.

Mauritsen, T., & Stevens, B. (2015). Missing iris effect as a possible cause of muted hydrological change and high climate sensitivity in models. *Nature Geoscience*, *8*(5), 346–351.

Mayta, V. C., & Adames Corraliza, Á. F. (2023). Is the Madden-Julian Oscillation a moisture mode? *Geophysical Research Letters*, *50*(15). https://doi.org/10.1029/2023gl103002

Medeiros, B., Clement, A. C., Benedict, J. J., & Zhang, B. (2021). Investigating the impact of cloud-radiative feedbacks on tropical precipitation extremes. *Npj Climate and Atmospheric Science*, *4*(1), 1–10.

Muller, C., & Bony, S. (2015). What favors convective aggregation and why? *Geophysical Research Letters*, *42*(13), 5626–5634.

Najarian, H., & Sakaeda, N. (2023). The influence of cloud types on cloud-radiative forcing during DYNAMO/AMIE. *Journal of Geophysical Research*, *128*(8). https://doi.org/10.1029/2022jd038006

Peters, M. E., & Bretherton, C. S. (2005). A Simplified Model of the Walker Circulation with an Interactive Ocean Mixed Layer and Cloud-Radiative Feedbacks. *Journal of Climate*, *18*(20), 4216–4234.

Peters, M. E., Kuang, Z., & Walker, C. C. (2008). Analysis of atmospheric energy transport in ERA-40 and implications for simple models of the mean tropical circulation. *Journal of Climate*, *21*(20), 5229–5241.

Pope, M., Jakob, C., & Reeder, M. J. (2009). Regimes of the north Australian wet season. *Journal of Climate*, *22*(24), 6699–6715.

Prakash, S., & Gairola, R. M. (2014). Validation of TRMM-3B42 precipitation product over the tropical Indian Ocean using rain gauge data from the RAMA buoy array. *Theoretical and Applied Climatology*, *115*(3), 451–460.

Prakash, S., Mahesh, C., & Gairola, R. M. (2013). Comparison of TRMM Multi-satellite Precipitation Analysis (TMPA)-3B43 version 6 and 7 products with rain gauge data from ocean buoys. *Remote Sensing Letters* , *4*(7), 677–685.

Prigent, C. (2010). Precipitation retrieval from space: An overview. *Comptes Rendus: Geoscience*, *342*(4), 380–389.

Rädel, G., Mauritsen, T., Stevens, B., & Dommenget, D. (2016). Amplification of El Nino by cloud longwave coupling to atmospheric circulation. *Nature*. Retrieved from https://www.nature.com/articles/ngeo2630

Raymond, D. J. (2001). A New Model of the Madden–Julian Oscillation. *Journal of the Atmospheric Sciences*, *58*(18), 2807–2819.

Raymond, D. J., & Fuchs, Ž. (2007). Convectively coupled gravity and moisture modes in a simple atmospheric model. *Tellus A Dynamic Meteorology and Oceanography*, *59*(5), 627.

Raymond, D. J., & Fuchs, Ž. (2009). Moisture Modes and the Madden–Julian Oscillation. *Journal of Climate*, *22*(11), 3031–3046.

Raymond, D. J., Sessions, S. L., Sobel, A. H., & Fuchs, Ž. (2009). The mechanics of gross moist stability. *Journal of Advances in Modeling Earth Systems*, *1*(3). https://doi.org/10.3894/james.2009.1.9

Reynolds, R. W., Rayner, N. A., Smith, T. M., Stokes, D. C., & Wang, W. (2002). An Improved In Situ and Satellite SST Analysis for Climate. *Journal of Climate*, *15*(13), 1609–1625.

Robe, F. R., & Emanuel, K. A. (2001). The Effect of Vertical Wind Shear on Radiative–Convective Equilibrium States. *Journal of the Atmospheric Sciences*, *58*(11), 1427–1445.

Roca, R., & Fiolleau, T. (2020). Extreme precipitation in the tropics is closely associated with long-lived convective systems. *Communications Earth & Environment*, *1*(1), 1–6.

Rossow, W. B., Mekonnen, A., Pearl, C., & Goncalves, W. (2013). Tropical Precipitation Extremes. *Journal of Climate*, *26*(4), 1457–1466.

Rotunno, R., Klemp, J. B., & Weisman, M. L. (1988). A Theory for Strong, Long-Lived Squall Lines. *Journal of the Atmospheric Sciences*, *45*(3), 463–485.

Ruppert, J. H., & Hohenegger, C. (2018). Diurnal Circulation Adjustment and Organized Deep Convection. *Journal of Climate*, *31*(12), 4899–4916.

Ruppert, J. H., Wing, A. A., Tang, X., & Duran, E. L. (2020). The critical role of cloud–infrared radiation feedback in tropical cyclone development. *Proceedings of the National Academy of Sciences*, *117*(45), 27884–27892.

Ruppert, J. H., Jr, & Klocke, D. (2019). The two diurnal modes of tropical upward motion. *Geophysical Research Letters*, *46*(5), 2911–2921.

Rutledge, S., Hein, P., Dolan, B., Powell, S., & Brodzik, S. (2018). *NCAR S-polka radar data: DYNAMO legacy data products*. UCAR Earth Observing Laboratory. Retrieved from https://orca.atmos.washington.edu/dynamo_legacy/resources/documents/readme/radar/radar_spolka_readme.pdf

Saxen, T. R., & Rutledge, S. A. (2000). Surface Rainfall–Cold Cloud Fractional Coverage Relationship in TOGA COARE: A Function of Vertical Wind Shear. *Monthly Weather Review*, *128*(2), 407–415.

Schumacher, C., & Houze, R. A. (2000). Comparison of Radar Data from the TRMM Satellite and Kwajalein Oceanic Validation Site. *Journal of Applied Meteorology and Climatology*, *39*(12), 2151–2164.

Schumacher, C., Houze, R. A., & Kraucunas, I. (2004). The Tropical Dynamical Response to Latent Heating Estimates Derived from the TRMM Precipitation Radar. *Journal of the Atmospheric Sciences*, *61*(12), 1341–1358.

Semie, A. G., & Bony, S. (2020). Relationship Between Precipitation Extremes and Convective Organization Inferred From Satellite Observations. *Geophysical Research Letters*, *47*(9), e2019GL086927.

Shell, K. M., de Szoeke, S. P., Makiyama, M., & Feng, Z. (2020). Vertical Structure of Radiative Heating Rates of the MJO during DYNAMO. *Journal of Climate*, *33*(12), 5317–5335.

Sobel, A., & Maloney, E. (2012). An Idealized Semi-Empirical Framework for Modeling the Madden–Julian Oscillation. *Journal of the Atmospheric Sciences*, *69*(5), 1691–1705.

Sobel, A., & Maloney, E. (2013). Moisture Modes and the Eastward Propagation of the MJO. *Journal of the Atmospheric Sciences*, *70*(1), 187–192.

Sobel, A., Wang, S., & Kim, D. (2014). Moist Static Energy Budget of the MJO during DYNAMO. *Journal of the Atmospheric Sciences*, *71*(11), 4276–4291.

Sobel, A. H., Held, I. M., & Bretherton, C. S. (2002). The ENSO Signal in Tropical Tropospheric Temperature. *Journal of Climate*, *15*(18), 2702–2706.

Sobel, A. H., Maloney, E. D., Bellon, G., & Frierson, D. M. (2008). The role of surface heat fluxes in tropical intraseasonal oscillations. *Nature Geoscience*, *1*(10), 653–657.

Sobel, A. H., Maloney, E. D., Bellon, G., & Frierson, D. M. (2010). Surface Fluxes and Tropical Intraseasonal Variability: a Reassessment. *Journal of Advances in Modeling Earth Systems*, *2*(1). https://doi.org/10.3894/JAMES.2010.2.2

Stein, T. H. M., Holloway, C. E., Tobin, I., & Bony, S. (2017). Observed Relationships between Cloud Vertical Structure and Convective Aggregation over Tropical Ocean. *Journal of Climate*, *30*(6), 2187–2207.

Stevens, B., Satoh, M., Auger, L., Biercamp, J., Bretherton, C. S., Chen, X., et al. (2019). DYAMOND: the DYnamics of the Atmospheric general circulation Modeled On Non-hydrostatic Domains. *Progress in Earth and Planetary Science*, *6*(1), 1–17.

Su, H., & David Neelin, J. (2002). Teleconnection Mechanisms for Tropical Pacific Descent Anomalies during El Niño. *Journal of the Atmospheric Sciences*, *59*(18), 2694–2712.

Sugiyama, M. (2009). The Moisture Mode in the Quasi-Equilibrium Tropical Circulation Model. Part I: Analysis Based on the Weak Temperature Gradient Approximation. *Journal of the Atmospheric Sciences*, *66*(6), 1507–1523.

Sulak, A. M., Calabrase, W. J., Ryan, S. D., & Heus, T. (2020). The contributions of shear and turbulence to cloud overlap for cumulus clouds. *Journal of Geophysical Research*, *125*(10). https://doi.org/10.1029/2019jd032017

de Szoeke, S. P., & Maloney, E. D. (2020). Atmospheric Mixed Layer Convergence from Observed MJO Sea Surface Temperature Anomalies. *Journal of Climate*, *33*(2), 547–558.

Takayabu, Y. N. (1994). Large-Scale Cloud Disturbances Associated with Equatorial Waves. *Journal of the Meteorological Society of Japan. Ser. II*, *72*(3), 433–449.

Tan, J., Jakob, C., Rossow, W. B., & Tselioudis, G. (2015). Increases in tropical rainfall driven by changes in frequency of organized deep convection. *Nature*, *519*(7544), 451–454.

Tobin, I., Bony, S., & Roca, R. (2012). Observational Evidence for Relationships between the Degree of Aggregation of Deep Convection, Water Vapor, Surface Fluxes, and Radiation. *Journal of Climate*, *25*(20), 6885–6904.

Tsai, W.-M., & Wu, C.-M. (2017). The environment of aggregated deep convection. *Journal of Advances in Modeling Earth Systems*, *9*(5), 2061–2078.

Tseng, Kai-Chih, Maloney, E., & Barnes, E. (2019). The Consistency of MJO Teleconnection Patterns: An Explanation Using Linear Rossby Wave Theory. *Journal of Climate*, *32*(2), 531–548.

Tseng, K-C, Barnes, E. A., & Maloney, E. D. (2018). Prediction of the Midlatitude Response to Strong Madden-Julian Oscillation Events on S2S Time Scales. *Geophysical Research Letters*, *45*(1), 463–470.

Vecchi, G. A., & Soden, B. J. (2007). Effect of remote sea surface temperature change on tropical cyclone potential intensity. *Nature*, *450*(7172), 1066–1070.

Waliser, D. E., & Graham, N. E. (1993). Convective cloud systems and warm-pool sea surface temperatures: Coupled interactions and self-regulation. *Journal of Geophysical Research*, *98*(D7), 12881.

Wang, T., & Li, T. (2022). Diversity of MJO Initiation Regions and Processes. *Journal of Climate*, *35*(20), 6721–6740.

Watanabe, M., & Kimoto, M. (2000). Atmosphere-ocean thermal coupling in the North Atlantic: A positive feedback. *Quarterly Journal of the Royal Meteorological Society*, *126*(570), 3343–3369.

Webster, P. J., & Stephens, G. L. (1980). Tropical upper-tropospheric extended clouds: Inferences from winter MONEX. *Journal of the Atmospheric Sciences*, *37*(7), 1521–1541.

Wheeler, M., & Kiladis, G. N. (1999). Convectively Coupled Equatorial Waves: Analysis of Clouds and Temperature in the Wavenumber–Frequency Domain. *Journal of the Atmospheric Sciences*, *56*(3), 374–399.

Wheeler, M., Kiladis, G. N., & Webster, P. J. (2000). Large-Scale Dynamical Fields Associated with Convectively Coupled Equatorial Waves. *Journal of the Atmospheric Sciences*, *57*(5), 613–640.

Wheeler, M. C., & Hendon, H. H. (2004). An All-Season Real-Time Multivariate MJO Index: Development of an Index for Monitoring and Prediction. *Monthly Weather Review*, *132*(8), 1917–1932.

Wing, A. A. (2019). Self-Aggregation of Deep Convection and its Implications for Climate. *Current Climate Change Reports*, *5*(1), 1–11.

Wing, A. A., Emanuel, K., Holloway, C. E., & Muller, C. (2017). Convective Self-Aggregation in Numerical Simulations: A Review. *Surveys in Geophysics*, *38*(6), 1173–1197.

Wing, A. A., Stauffer, C. L., Becker, T., Reed, K. A., Ahn, M.-S., Arnold, N. P., et al. (2020). Clouds and Convective Self-Aggregation in a Multimodel Ensemble of Radiative-Convective Equilibrium Simulations. *Journal of Advances in Modeling Earth Systems*, *12*(9), e2020MS002138.

Wolding, B., Dias, J., Kiladis, G., Ahmed, F., Powell, S. W., Maloney, E., & Branson, M. (2020). Interactions between moisture and tropical convection. Part I: The coevolution of moisture and convection. *Journal of the Atmospheric Sciences*, *77*(5), 1783–1799.

Wolding, B., Rydbeck, A., Dias, J., Ahmed, F., Gehne, M., Kiladis, G., et al. (2023). Atmosphere–Ocean Coupled Energy Budgets of Tropical Convective Discharge–Recharge Cycles. *Journal of the Atmospheric Sciences*, *81*(1), 3–29.

Wolding, B. O., & Maloney, E. D. (2015). Objective Diagnostics and the Madden–Julian Oscillation. Part II: Application to Moist Static Energy and Moisture Budgets. *Journal of Climate*, *28*(19), 7786–7808.

Wolding, B. O., Maloney, E. D., & Branson, M. (2016). Vertically resolved weak temperature gradient analysis of the Madden- Julian Oscillation in SP-CESM. *Journal of Advances in Modeling Earth Systems*, *8*(4), 1586–1619.

Xie, P., & Arkin, P. A. (1997). Global Precipitation: A 17-Year Monthly Analysis Based on Gauge Observations, Satellite Estimates, and Numerical Model Outputs. *Bulletin of the American Meteorological Society*, *78*(11), 2539–2558.

Yanai, M., Esbensen, S., & Chu, J.-H. (1973). Determination of Bulk Properties of Tropical Cloud Clusters from Large-Scale Heat and Moisture Budgets. *Journal of the Atmospheric Sciences*, *30*(4), 611–627.

Yasunaga, K., & Mapes, B. (2012). Differences between More Divergent and More Rotational Types of Convectively Coupled Equatorial Waves. Part I: Space–Time Spectral Analyses. *Journal of the Atmospheric Sciences*, *69*(1), 3–16.

Yasunaga, K., Yokoi, S., Inoue, K., & Mapes, B. E. (2019). Space–Time Spectral Analysis of the Moist Static Energy Budget Equation. *Journal of Climate*, *32*(2), 501–529.

Yu, J.-Y., & David Neelin, J. (1997). Analytic Approximations for Moist Convectively Adjusted Regions. *Journal of the Atmospheric Sciences*, *54*(8), 1054–1063.

Yu, L., & Weller, R. A. (2007). Objectively Analyzed Air–sea heat fluxes for the global ice-free oceans (1981–2005). *Bulletin of the American Meteorological Society*, *88*(4), 527–540.

Zhang, C., Gottschalck, J., & Maloney, E. D. (2013). Cracking the MJO nut. *Geophysical*. Retrieved from https://agupubs.onlinelibrary.wiley.com/doi/abs/10.1002/grl.50244@10.1002/(ISSN)1944-8007.ATMOS_VARIABILITY

Zhang, C., Adames, Á. F., Khouider, B., Wang, B., & Yang, D. (2020). Four Theories of the Madden-Julian Oscillation. *Reviews of Geophysics* , *58*(3), e2019RG000685.

Zhang, Chidong. (1993). Large-Scale Variability of Atmospheric Deep Convection in Relation to Sea Surface Temperature in the Tropics. *Journal of Climate*, *6*(10), 1898–1913.

Zhang, Chidong, & Ling, J. (2012). Potential Vorticity of the Madden–Julian Oscillation. *Journal of the Atmospheric Sciences*, *69*(1), 65–78.

Zhang, T., Hoell, A., Perlwitz, J., Eischeid, J., Murray, D., Hoerling, M., & Hamill, T. M. (2019). Towards probabilistic multivariate ENSO monitoring. *Geophysical Research Letters*, *46*(17–18), 10532–10540.

Zipser, E. J., Cecil, D. J., Liu, C., Nesbitt, S. W., & Yorty, D. P. (2006). WHERE ARE THE MOST INTENSE THUNDERSTORMS ON EARTH? *Bulletin of the American Meteorological Society*, *87*(8), 1057–1072.

Zurovac-Jevtić, D., Bony, S., & Emanuel, K. (2006). On the Role of Clouds and Moisture in Tropical Waves: A Two-Dimensional Model Study. *Journal of the Atmospheric Sciences*, *63*(8), 2140–2155.

APPENDIX A

Supplementary Figures

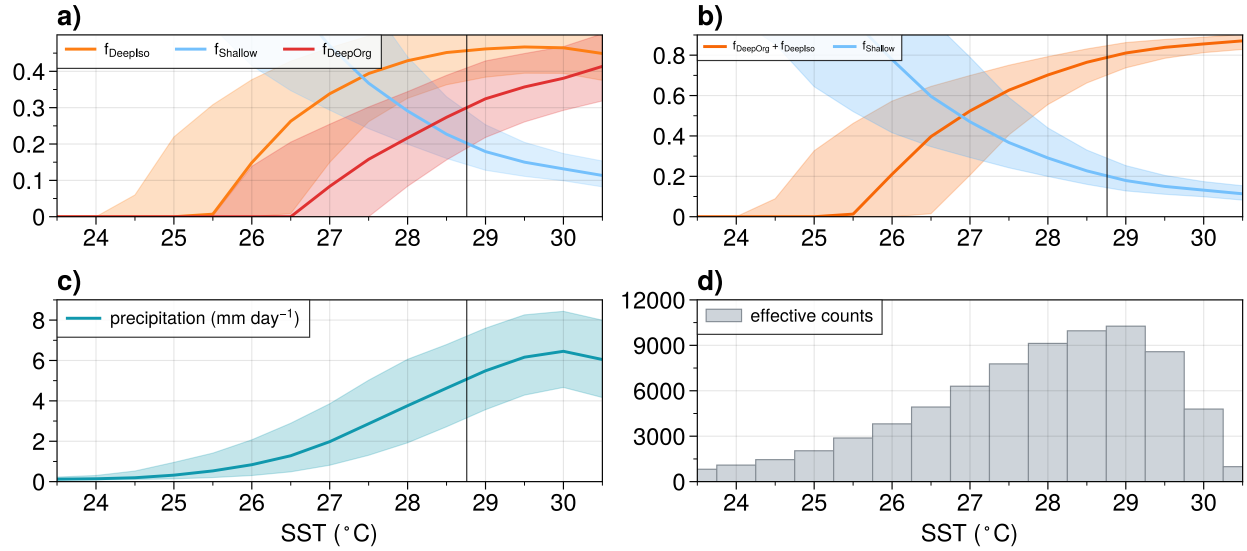

Figure A2.1. As in **Figure 2.2**, but with CRS rain contributions and other averaged quantities obtained by 10° × 10° domains.

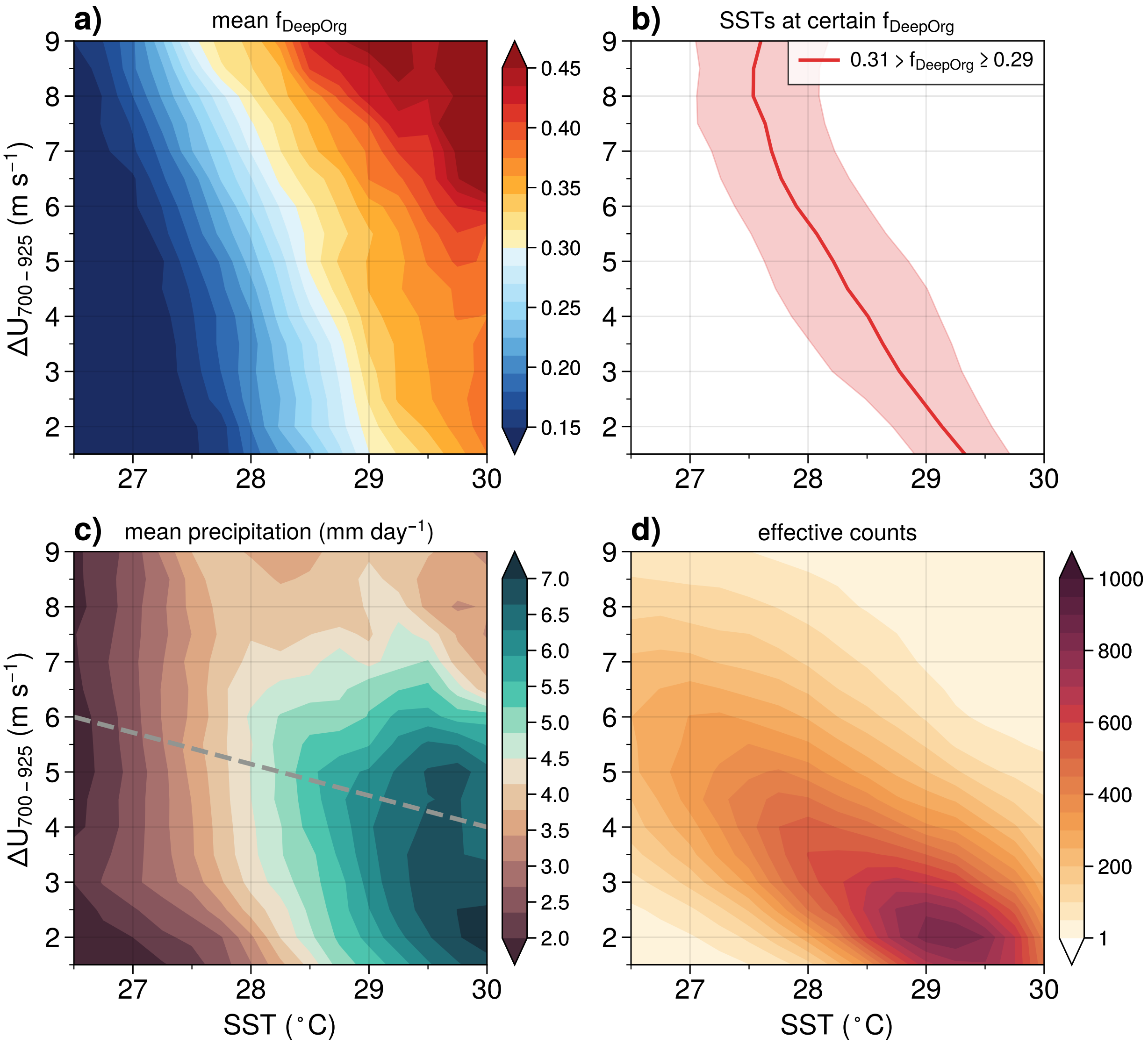

Figure A2.2. As in **Figure 2.7**, but with CRS rain contributions and other averaged quantities obtained by 10° × 10° domains.

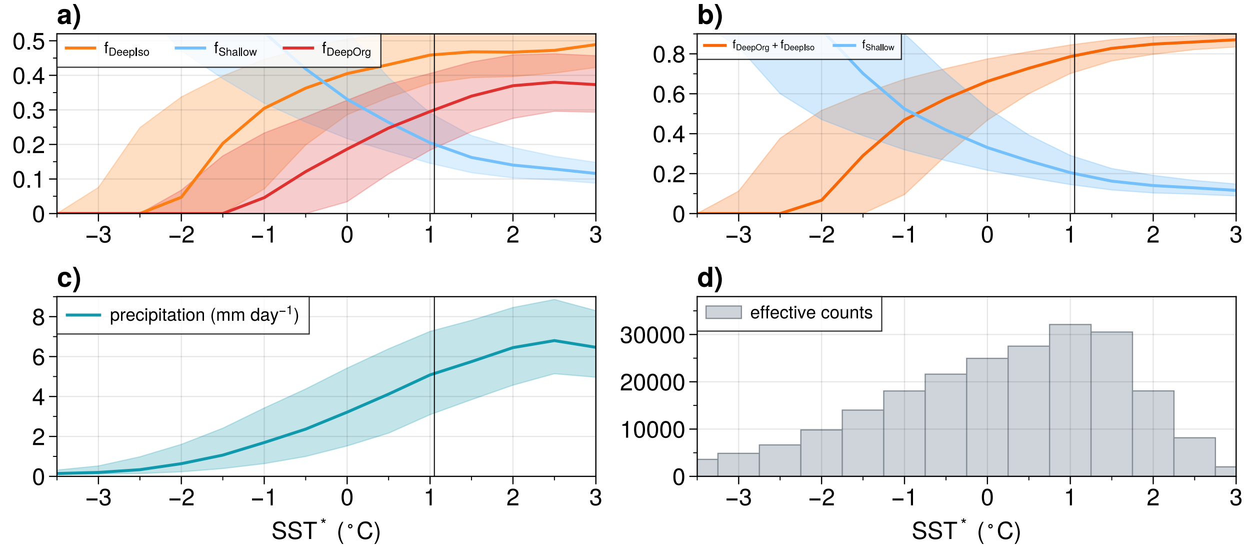

Figure A2.3. As in **Figure 2.4**, but with CRS rain contributions and other averaged quantities obtained by 10° × 10° domains.

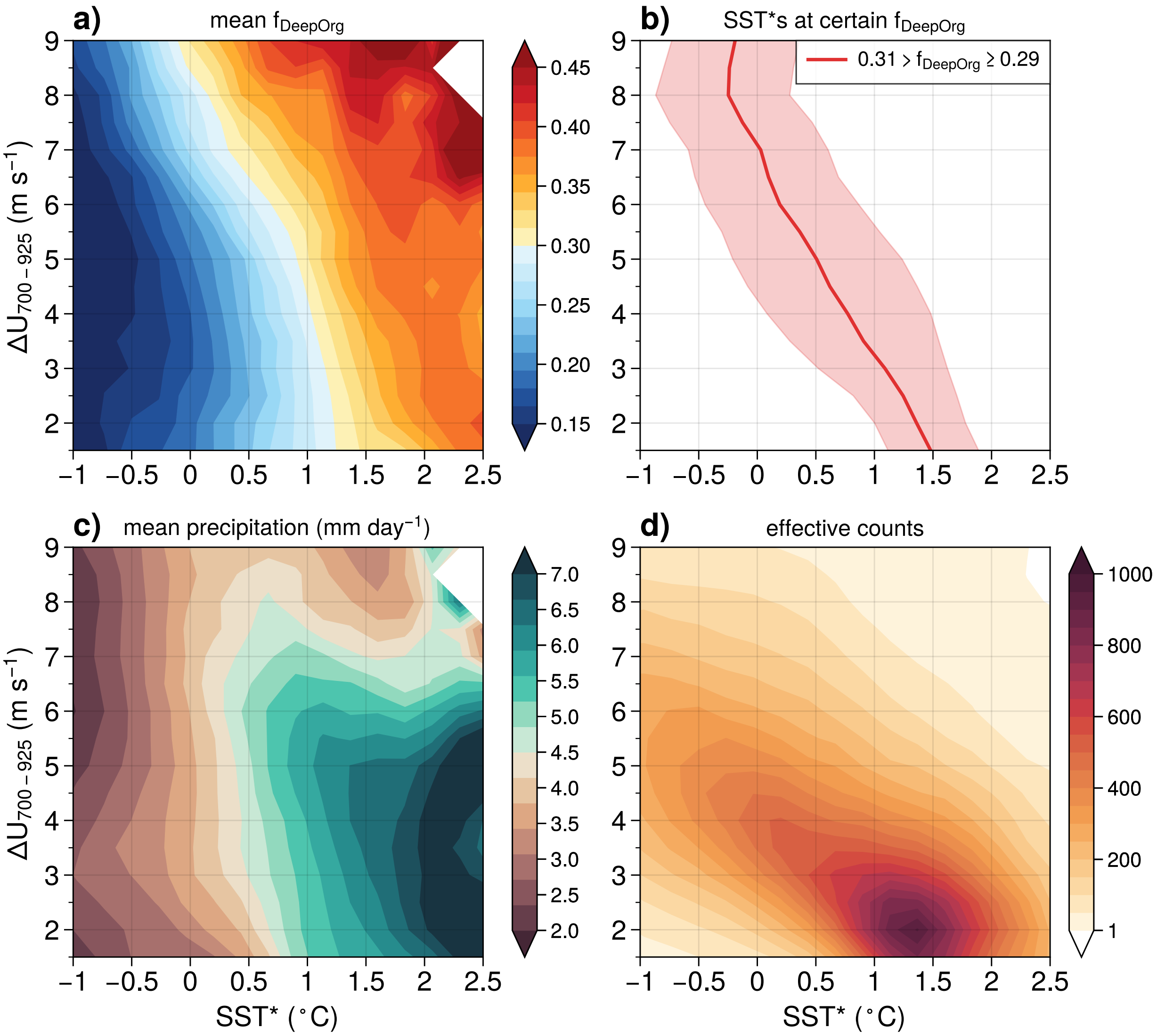

Figure A2.4. As in **Figure 2.7**, but with binning by SST* instead of SST, and showing CRS rain contributions and other averaged quantities obtained by 10° × 10° domains.

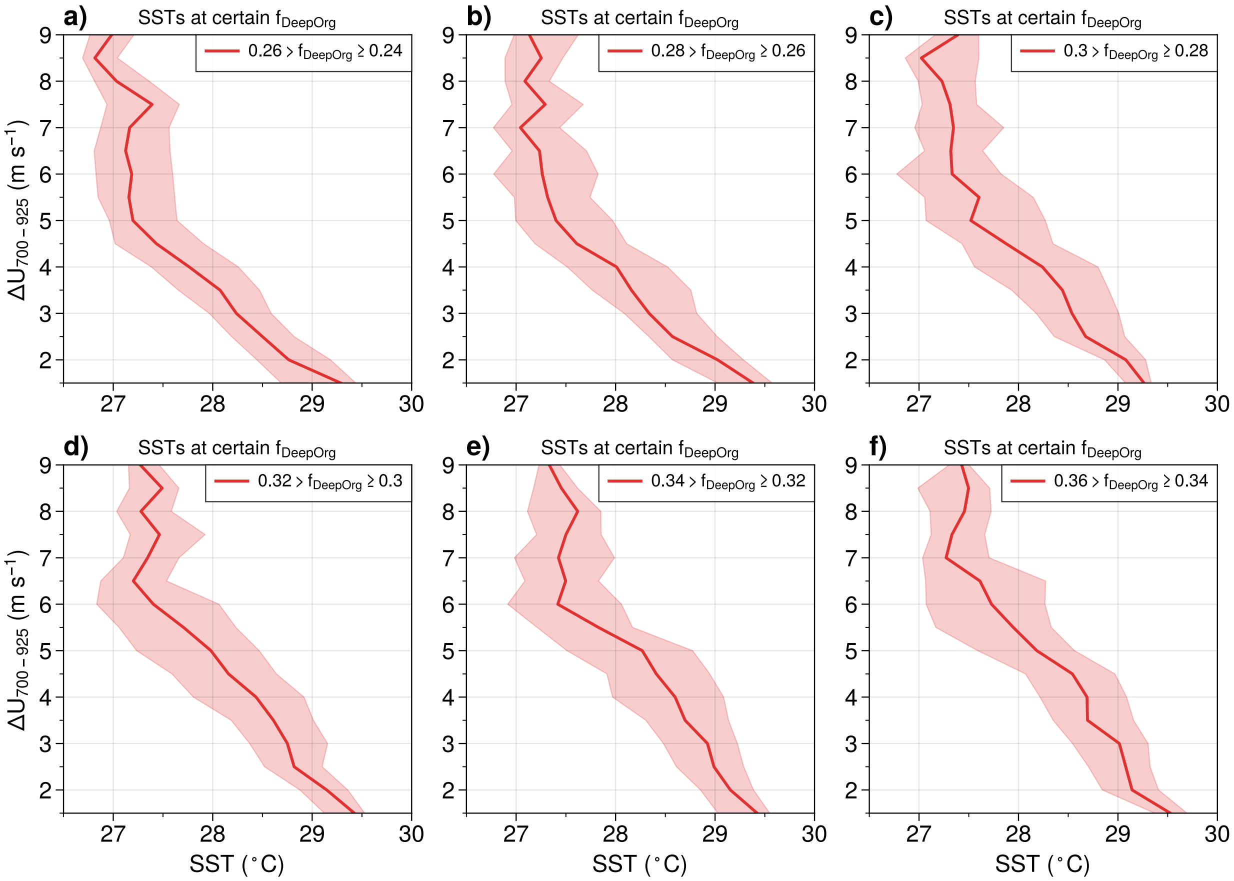

Figure A2.5. As in **Figure 2.7b**, but with different criteria ranges of $f_{DeepOrg}$ as annotated at the upper right corner of each panel.

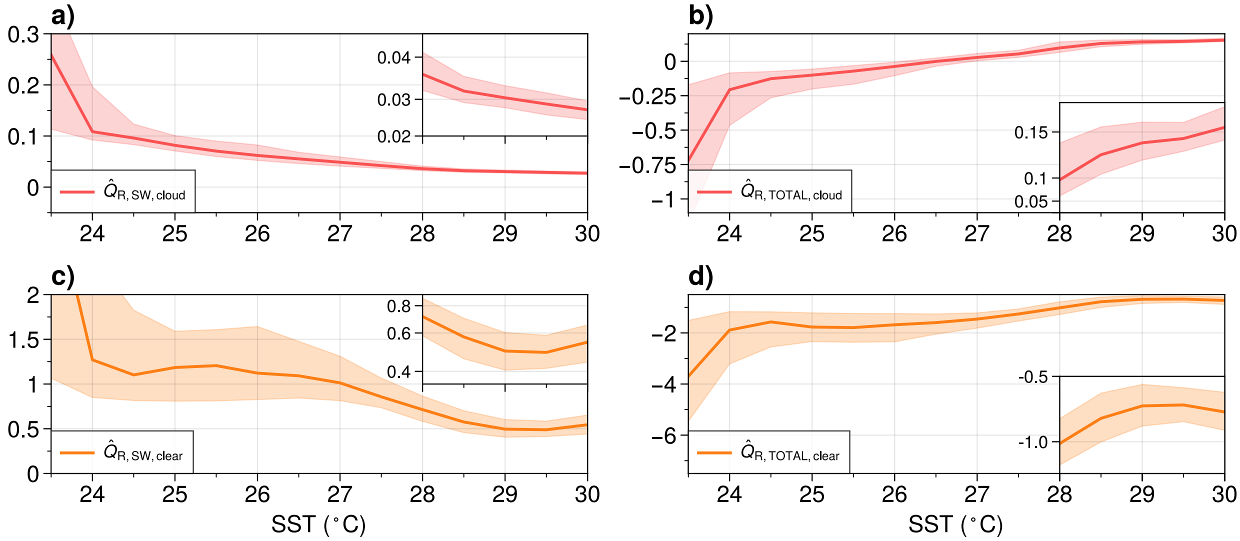

Figure A2.6. As in **Figures 2.3a, c**, but showing (a)(c) the shortwave radiative heating component and (b)(d) the total (shortwave plus longwave) radiative heating component.

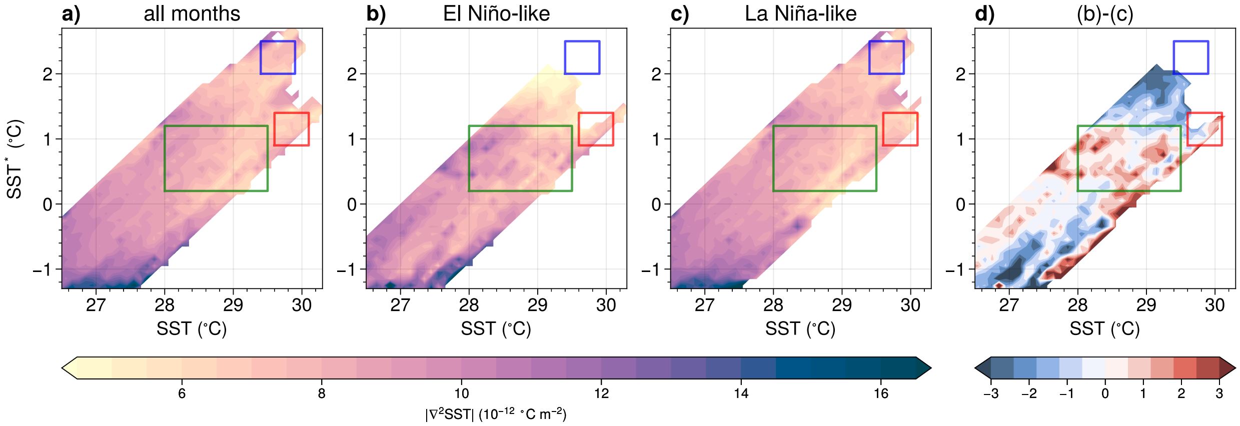

Figure A2.7. As **Figure 2.6**, but showing mean $|\nabla^2\mathrm{SST}|$ instead of effective counts.

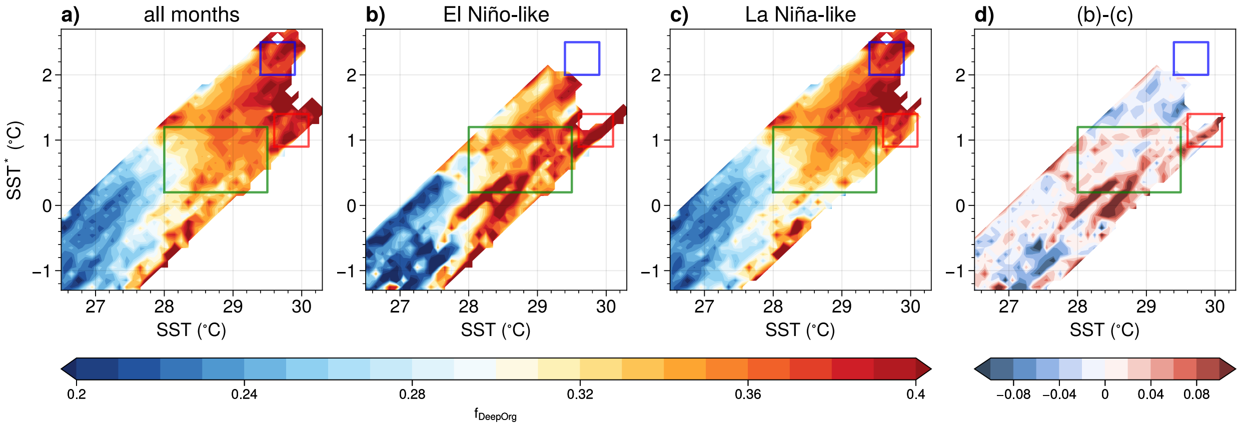

Figure A2.8. As **Figure 2.6**, but showing mean f_{DeepOrg} instead of effective counts.

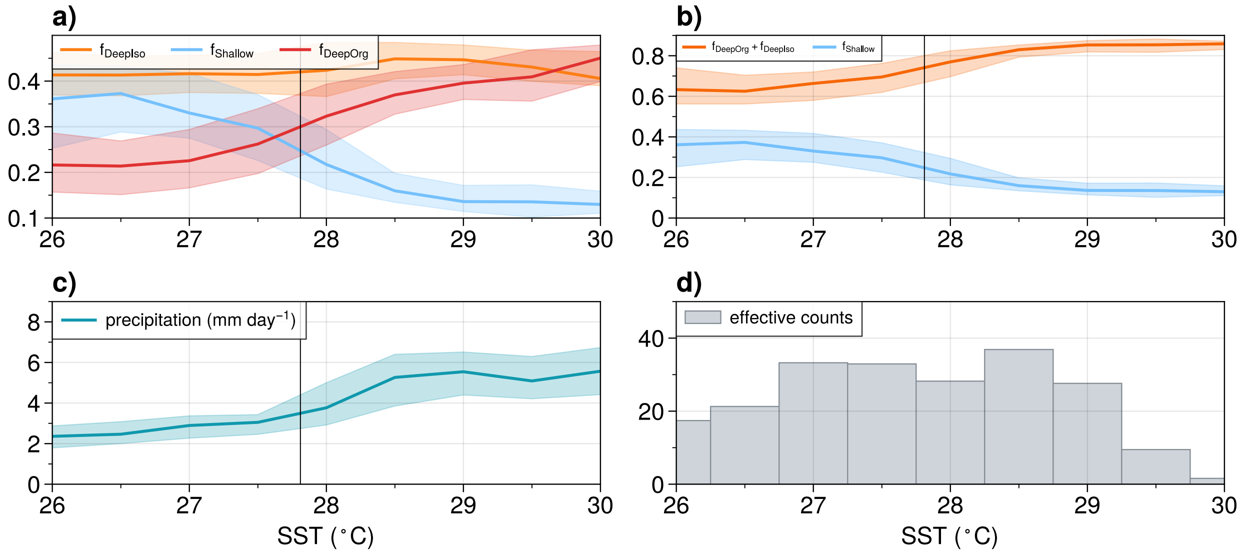

Figure A2.9. As **Figure 2.2** (binned by SST), but selecting samples only with $|\nabla^2\mathrm{SST}|$ in 10 to 11 $\times 10^{-12}$ °C m^{-2}. The range is chosen to avoid the intensely low $|\nabla^2\mathrm{SST}|$ of $< 7 \times 10^{-12}$ °C m^{-2} at high SST*s associated with El Niño shown in **Figure A2.7**.

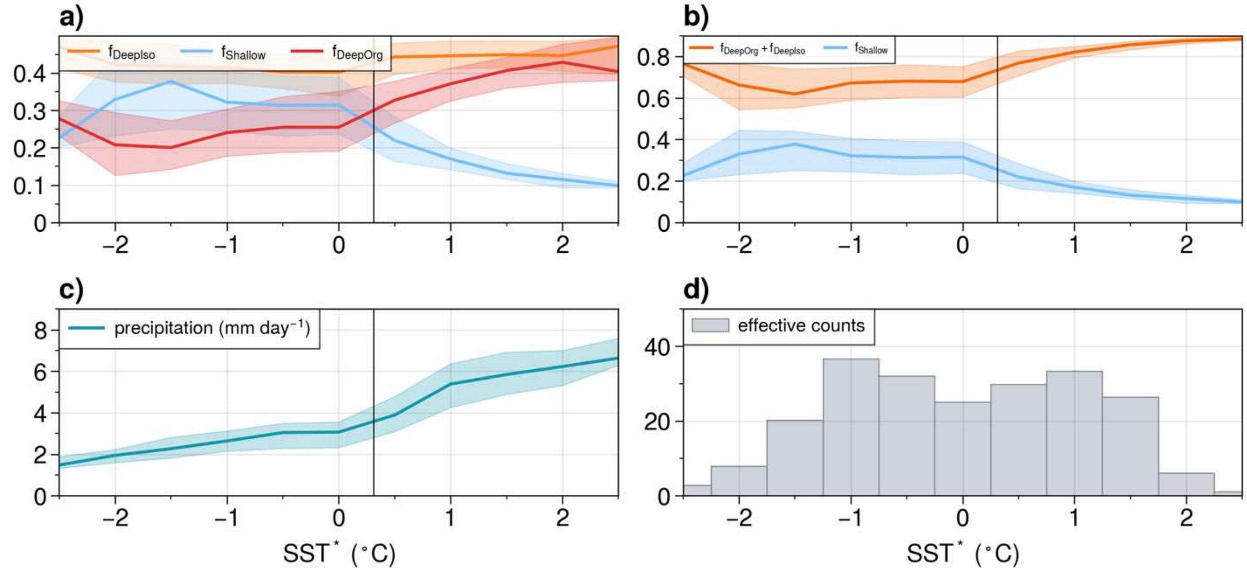

Figure A2.10. As **Figure 2.4** (binned by SST*), but selecting samples only with $|\nabla^2\mathrm{SST}|$ in 10 to 11 × 10^{-12} °C m^{-2}. The range is chosen to avoid the intensely low $|\nabla^2\mathrm{SST}|$ of $< 7 \times 10^{-12}$ °C m^{-2} at high SST*s associated with El Niño shown in **Figure A2.7**.

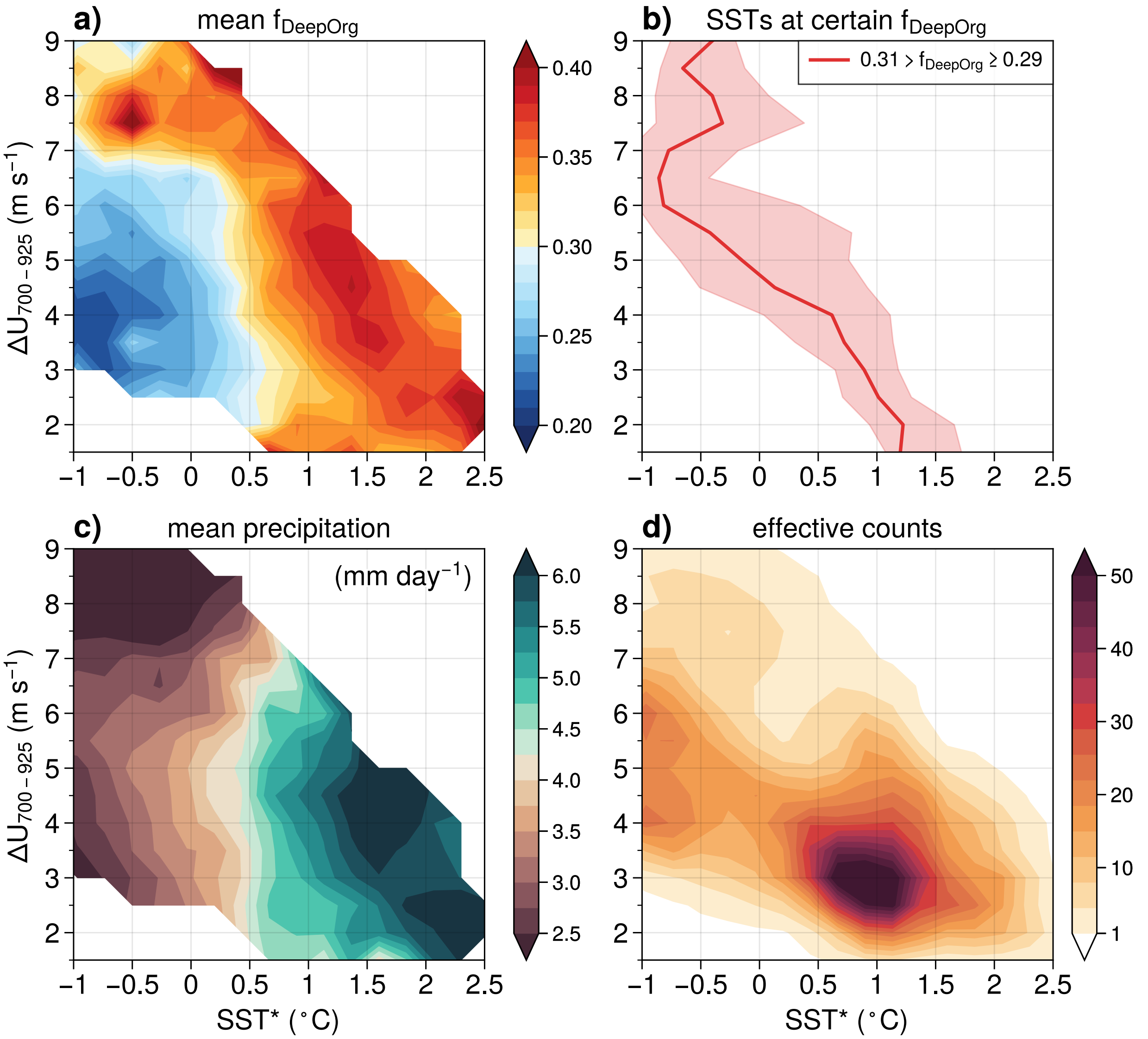

Figure A2.11. As in **Figure 2.7**, but binned by the deviation of SST from its tropical mean (SST*) every 0.25°C instead of SST on the x-axis.

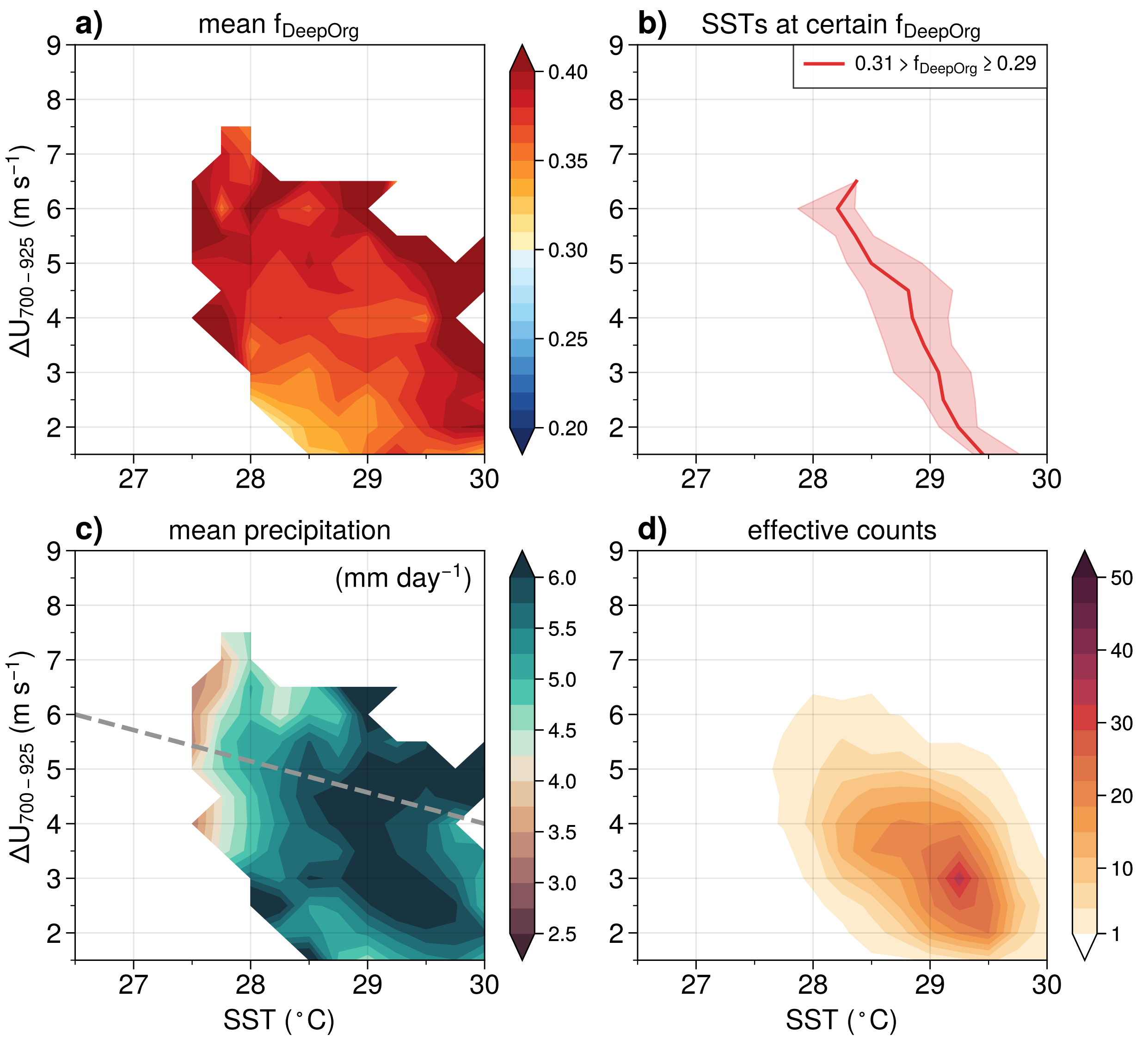

Figure A2.12. As in **Figure 2.7**, but obtained only with the domains including the Maritime Continent, namely the domains with their center longitudes over 90°E-170°E.

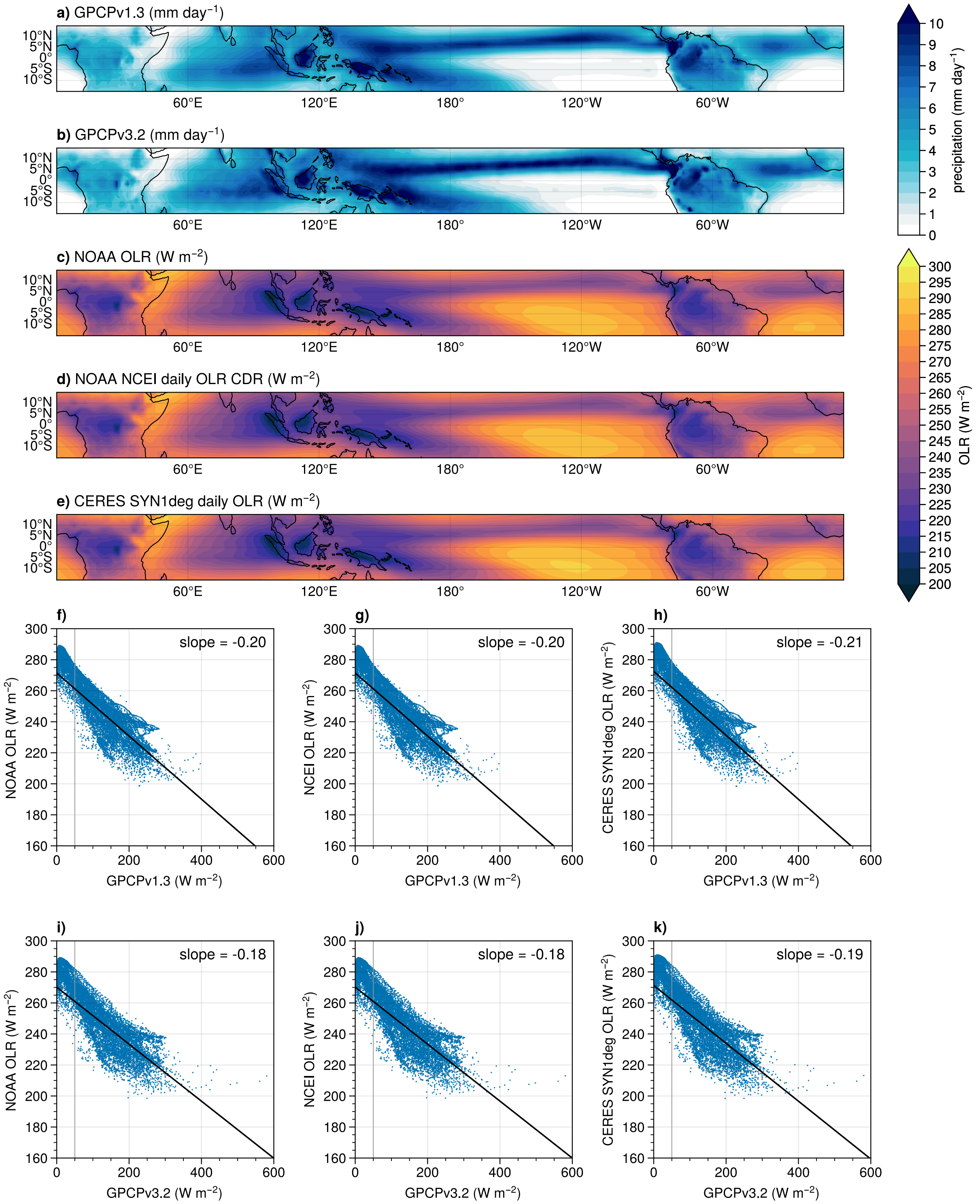

Figure A3.1. As in **Figures 3.1d**, showing the annual-mean climatological precipitation from (a) GPCPv1.3, (b) GPCPv3.2, and OLR from (c) NOAA OLR, (d) NOAA NCEI CDR daily OLR, and (e) CERES daily OLR. Also as in **Figure 3.1e-f**, (f-k) show the scatter plots and climatological feedback between two versions of GPCP and three OLR products as labeled on the axes.

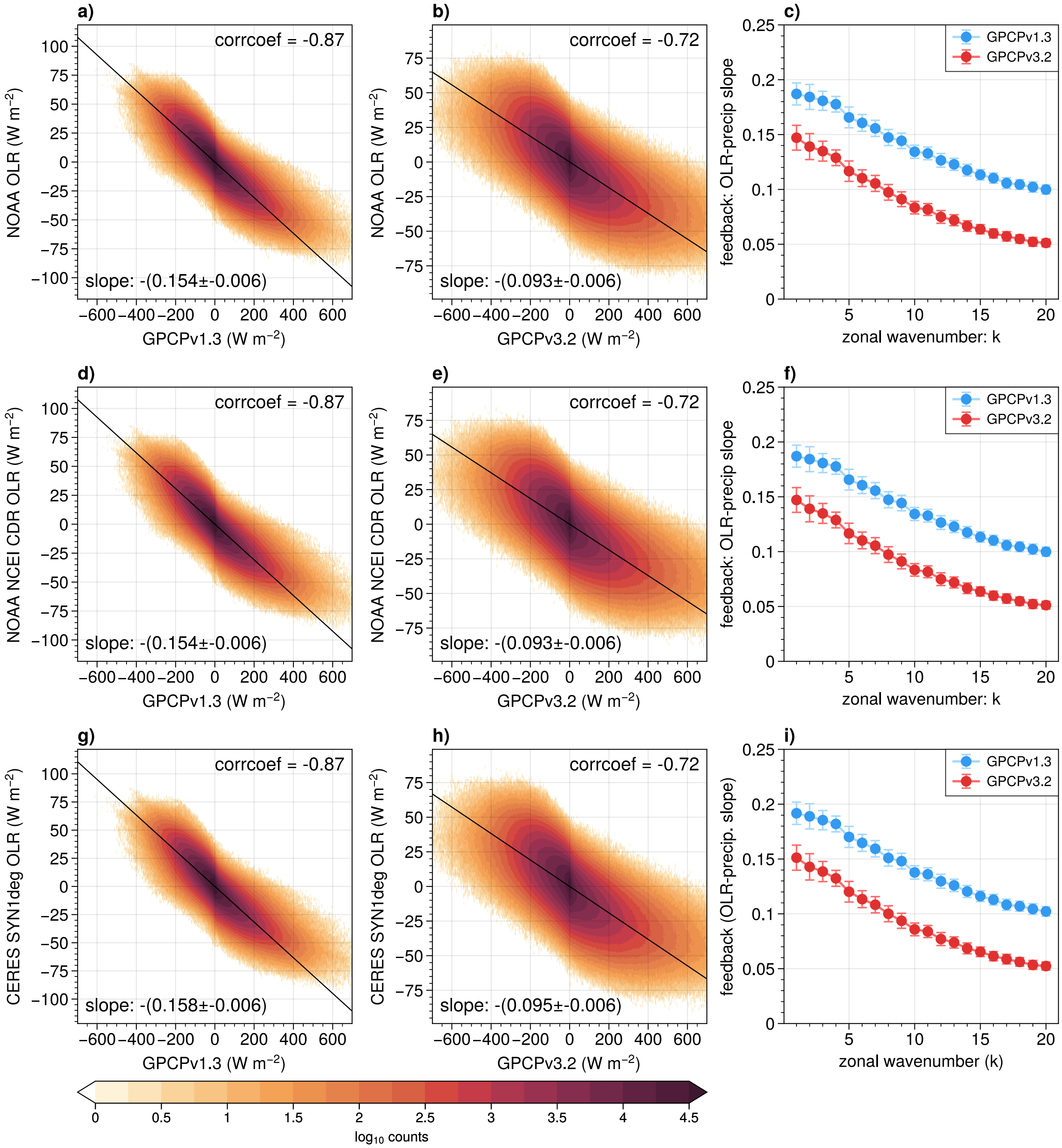

Figure A3.2. As in **Figures 3.2a-b** and **3.2d**, showing the histograms and radiative feedback of 20-100 day-filtered OLR and precipitation over the Indo-Pacific warm pool (60°E-180°, 15°S-15°N), but using the OLR product of (a-c) NOAA OLR, (d-f) NOAA NCEI CDR daily OLR, and (g-i) CERES OLR.

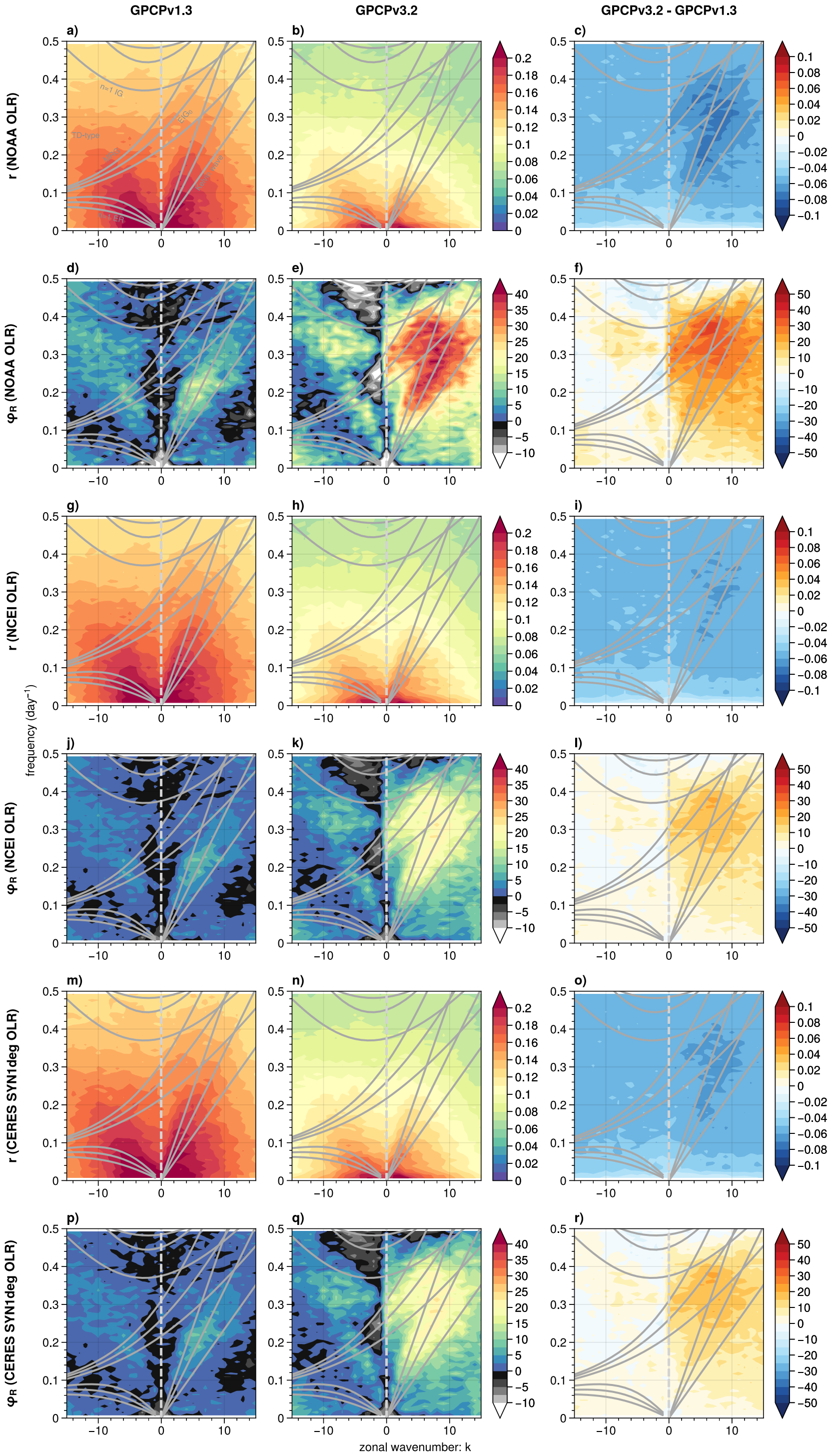

Figure A3.3. (a-f) as in **Figures 3.4d-i**, while (g-l) uses NOAA NCEI CDR daily OLR, and (m-r) uses CERES SYN1deg OLR.

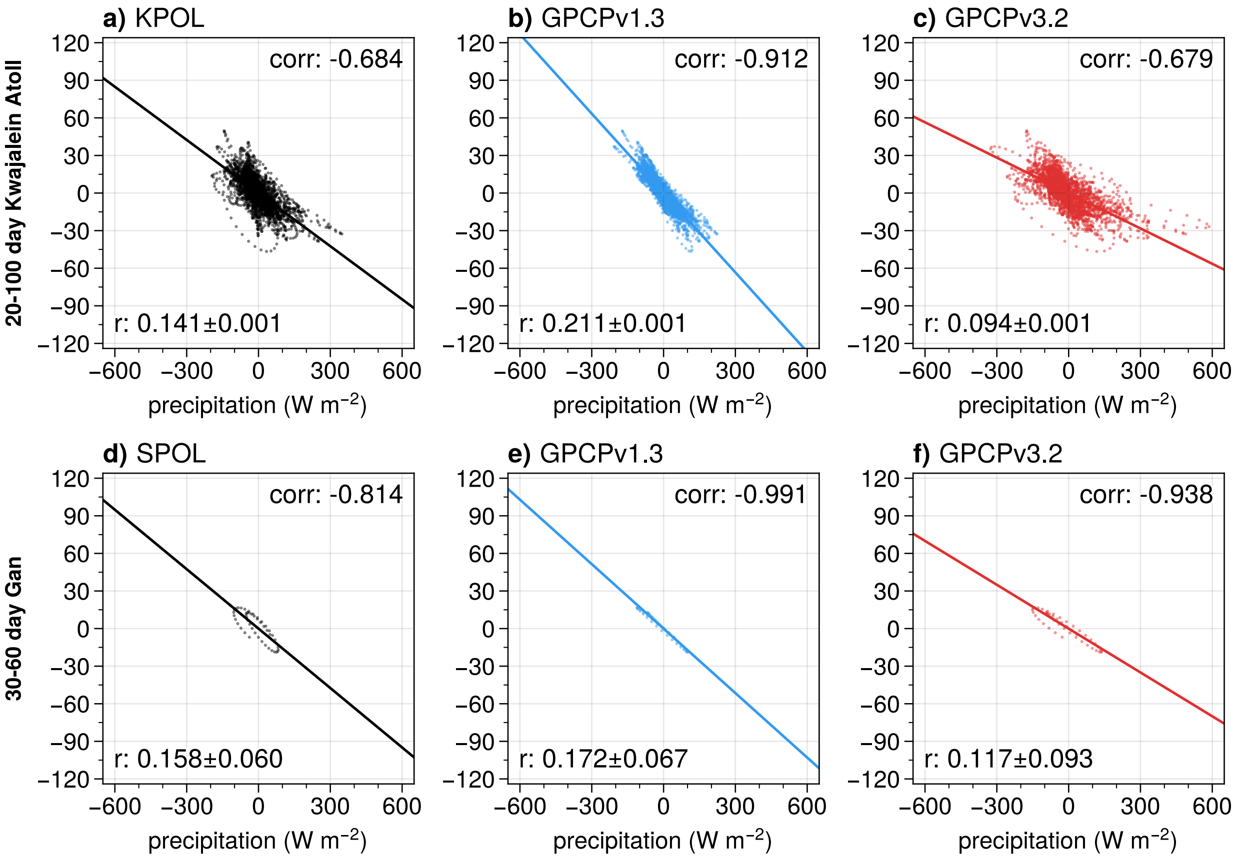

Figure A3.4. As in **Figure 3.2c**, showing the scatter plots of NOAA OLR against precipitation observations on (a-c) Kwajalein Atoll during 1 Apr 2014 – 31 Dec 2021 filtered for variability of 20-100 days, but plotted separately for different precipitation observations as labeled for clarity. (d-f) as (a-c), but showing observations on Gan Island during the DYNAMO field campaign period (1 Oct 2011 – 15 Jan 2012) filtered for variability of 30-60 days.

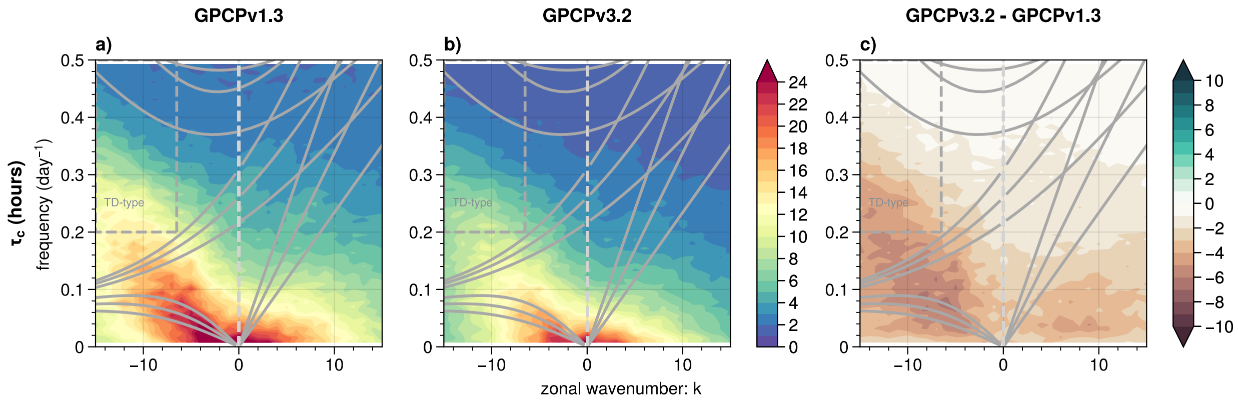

Figure A3.5. As in **Figures 3.3a-c**, but showing convective adjustment time (denoted as τ_c in many previous studies). τ_c is calculated as the ratio of the co-spectrum $[K(\cdot,\cdot)]$ of ERA5 column-integrated specific humidity anomaly $<q'>$ and GPCP precipitation anomaly P' to the power spectrum of precipitation anomaly ($4P^2$), or $\tau_c = K[<q'>,P']/4P^2$. Note that a domain of TD-type wave is outlined with gray dashed lines near the top left of the panels.

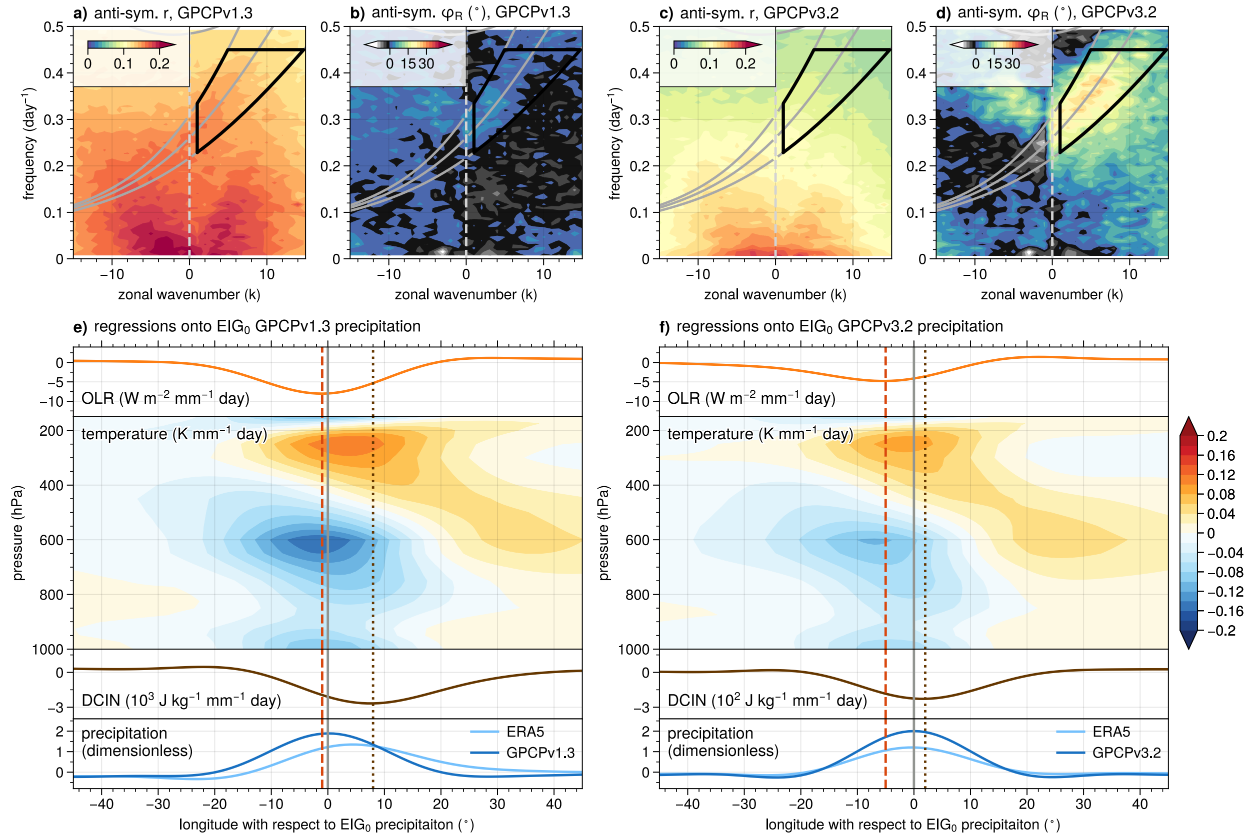

Figure A3.6. As **Figure 3.4**, but for n = 0 eastward inertia-gravity waves (EIG_0).

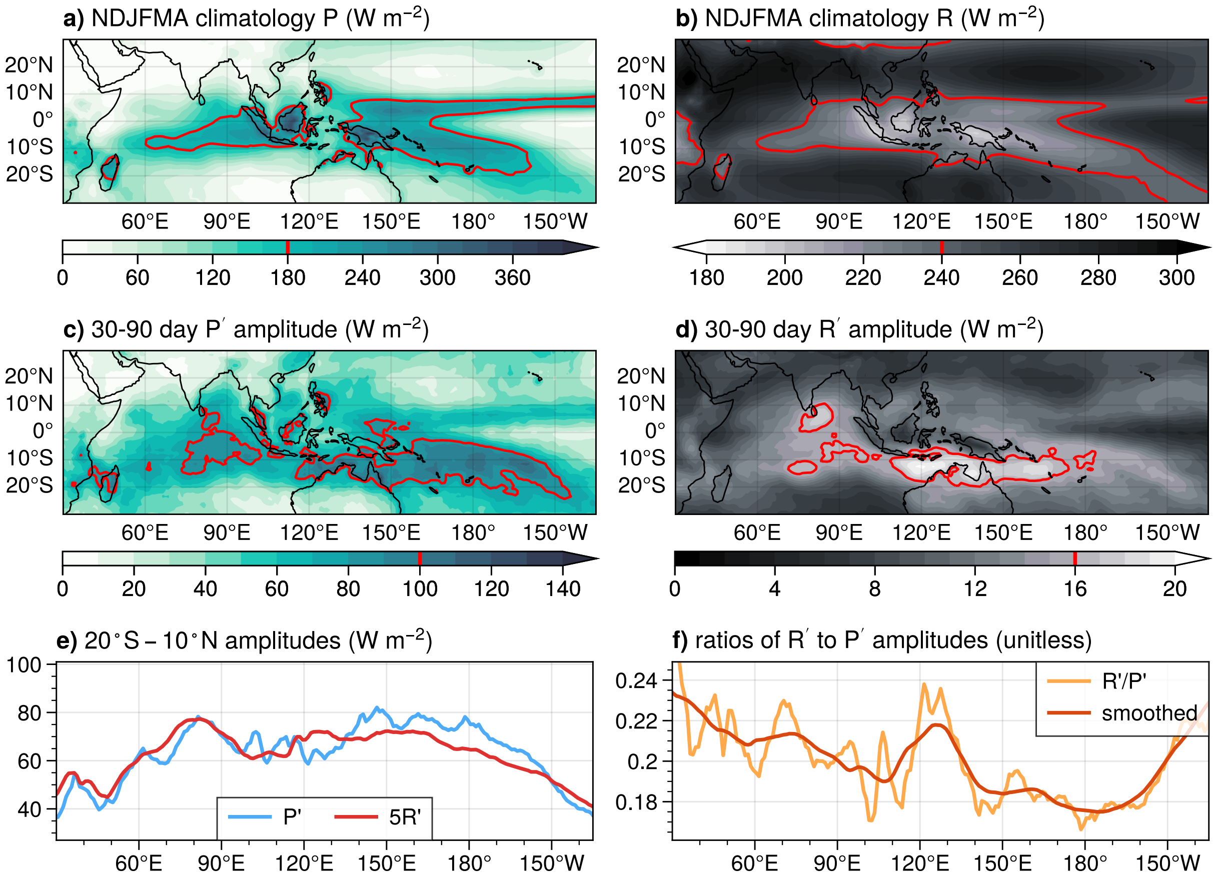

Figure A5.1. As **Figure 5.1** but using GPCPv1.3 in the precipitation field.

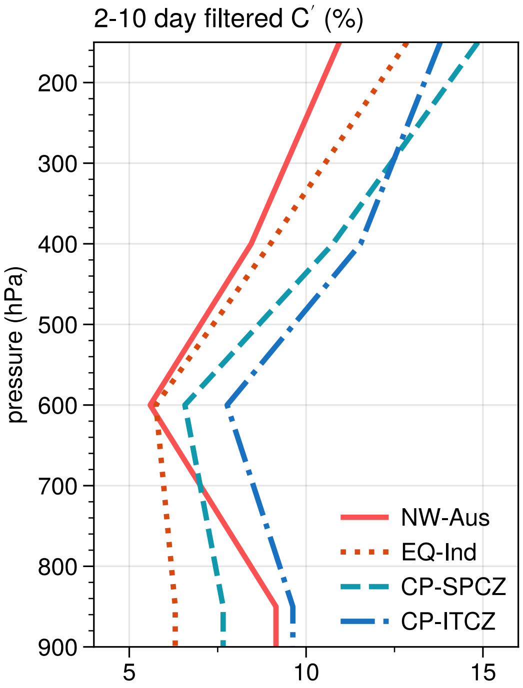

Figure A5.2. As **Figure 5.3b**, but for *C*’ calculated using 2-10-day filtered cloud covers.

APPENDIX B

Supplementary Text for Chapter 3

B1. Details of the spectral analyses

To obtain the spectral quantities related to the radiative feedback, OLR, precipitation, and column-integrated specific humidity (<q>), they are detrended over the entire time span and the first three harmonics of the annual cycle are removed to obtain anomalies. Spatiotemporal Fourier decomposition is applied to the anomalies following Hayashi (1971) to obtain the power spectra, co-spectra, and quadrature spectra at each latitude and 128-day window shifted consecutively by a day and 10-day Hanning tapering at both ends. The amplitude spectra R and P are calculated as the latitudinal (15°S-15°N) and temporal average of the square roots of half of the power spectra of OLR and precipitation, respectively. The phase spectra φ_R between precipitation and OLR is calculated as in equation (4-12) in Hayashi (1971) after latitudinal and temporal averaging of their co-spectra [$K(\cdot,\cdot)$] and quadrature-spectra [$Q(\cdot,\cdot)$] as:

$$\varphi_R = tan^{-1}[Q(precipitation, OLR)/K(precipitation, OLR)]$$

The convective adjustment time τ_c in the spectral space examined in **Chapter 3.3.3** is calculated following Yasunaga et al. (2019) and Adames et al. (2019) as:

$$\tau_c = K(precipitation, < q >)/(4P^2)$$

The regression method to produce **Figures 3.4** and **A3.6** is as follows. Precipitation spectra in the spectral range associated with select waves (Kelvin wave as indicated in **Figures 3.4a-d** and EIG$_0$ as indicated in **Figures A3.6a-d**) in k-ω space are determined by assigning zero values outside of the area, and an inverse Fourier decomposition is applied to obtain the variability of precipitation associated with the wave of interest. A meridional mean over the tropics (15°S-15°N) is then applied onto this 2-D wave-associated precipitation, and the resultant meridional-mean wave-associated precipitation is used as the predictor in the regression. Anomalous precipitation, OLR, air temperature, and DCIN are linearly regressed onto the wave-associated meridional-mean precipitation at each latitude at lag-0 time and all possible lead-lag longitudes. A meridional mean over the tropics (15°S-15°N) is then applied on all the output variables of the regression for showing regression slopes and correlation coefficients, and conducting statistical tests. **Figure A3.6** follows a similar procedure but with filtering using the EIG_0 spectral range.

B2. Details of the statistical methods

To obtain the 95% confidence interval (CI) of the MJO radiative feedback in **Figure 3.2** and regressions in **Figures 3.4** and **A3.6**, we calculate the expected value [$E(\cdot)$] of the regression slope (*S*) by linearly regressing some variable *Y* onto *X*. The statistical significance interval of *S* based on a Student-t test can be written as:

$$E(S) \pm t(0.025, n-2) \cdot s_S$$

where s_S is the estimated standard error of *S*, and the term t denotes the value where the cumulative probability density is at 0.025 in a Student-t distribution with *n* - 2 degrees of freedom. Here, *n* can be estimated as the number of individual samples, which will be discussed later. s_S can be obtained as:

$$s_S = \sqrt{\frac{\Sigma_i (Y_i - \widehat{Y}_i)^2}{\Sigma_i (X_i - \bar{X})^2} \cdot \frac{1}{n-2}}$$

where subscript i denotes sample counts, $\widehat{X}_i$ denotes the predicted value of *X* by *Y* based on the linear fit, $\bar{Y}$ is the mean of *Y*, and *n* denotes the number of individual samples.

When estimating n using OLR in **Figure 3.2**, the spatial degree of freedoms is estimated following the "moment-matching" method in Bretherton et al. (1999), which provides a more conservative degree of freedom than other methods utilizing empirical orthogonal functions. When estimating n using the meridional-mean wave-associated precipitation in **Figures 3.4** and **A3.6**, the spatial degree of freedom is calculated as the total spatial length divided by the decorrelation length defined by counting points when its lead-lag autocorrelation is larger than e^{-1}. The temporal degree of freedoms for both **Figures 3.2**, **3.4**, and **A3.6** are estimated by dividing the total length of the timeseries by the decorrelation time scale of the given Y data. In particular, the decorrelation time scale is estimated with the following procedure considering that the correlation coefficients ($\hat{r}$) exhibit wave-like behavior along the lead-lag time axis using temporally filtered data. First, the first peaks where $\hat{r}$ is smaller than e^{-1} on both leading or lagging sides, say, which have $\hat{r}(t_{-1})$ on the lag side and $\hat{r}(t_1)$ on the lead side given $t_1 = -t_{-1}$, are located. The width where $\hat{r}$ first touches zero is defined as the decorrelation time scale, which is estimated by linearly extrapolating the decay of $\hat{r}$ at t_{-1} and t_1 away from t = 0. The decorrelation time scale (t_d) is calculated with the following equation using only data over 1 September 2000 to 31 August 2003 in **Figure 3.2** and 2 September 2000 to 1 September 2002 in **Figures 3.4** and **A3.6** for computational resource considerations:

$$t_d = \frac{t_{-1}}{1 - r(t_{-1})} + \frac{t_1}{1 - r(t_1)}$$

Finally, multiplying the spatial degree of freedom by the temporal degree of freedom yields n. Inserting the value of n into the previous equations yields the significance interval of S. Note that in **Figures 3.4** and **A3.6**, all data points of regression slopes shown pass the statistical significance test that none of the 95% CI of the slopes include zero.